

**BREAKING SYMMETRY IN LIQUID BRIDGES: THE EFFECT OF
PINNING AND ASPECT RATIO ON CAPILLARY FORCES**

by
David Broesch

A dissertation submitted to The Johns Hopkins University in conformity with the
requirements for the degree of Doctor of Philosophy

Baltimore Maryland
February 2014

© 2014 David Broesch
All rights reserved

Capillary bridges between solid substrates are critical to a myriad of natural and industrial processes, such as oil recovery from porous rocks, or the packaging of micro-circuitry components. Generally, the surfaces of these solids are not uniform, and contain physical or chemical heterogeneities that result in asymmetric bridge morphologies (due to the partial pinning of the solid-liquid-vapor interface). While such pinning can greatly affect the forces and morphologies of the liquid, many studies that investigate capillary bridges assume the solid surfaces to be ideal, and the subsequent bridge profiles to be highly symmetric. This thesis details our investigations of how breaking symmetry (through changing of the pinning condition or the shape of the substrates) results in quantitative changes to the properties of the capillary bridges such as the morphology, forces and torques.

First, we explored the importance of the pinning condition by studying capillary bridges in a narrow rectangular slit pore, which is one of the simplest ways to break symmetry. We employed experiments, numerical simulations, and theory to highlight the importance of pinning on the bridge morphology and associated capillary forces. Experiments showed that as the height of the slit pore is increased past the width of the strip the mean curvature of the capillary bridge changes sign from negative to positive (concave to convex). This counterintuitive observation was confirmed by using Surface Evolver simulations. Interestingly, the force the capillary bridge exerts on the pore itself always remains attractive due to the dominance of the vertical projection of the surface tension force at the pinning boundary. It was also found that the mean curvature was

independent of the liquid volume in the pore, as long as the bridge did not extend to the end of the strip. We developed a simple theory to show that the change in mean curvature can be described as a competition between the confinement of the liquid bridge and the wetting of the strip.

Next, we studied the role of substrate shape on the restoring forces and torques of capillary based self-alignment systems, such as “flip-chip” micro-circuit packaging. To do this we varied systematically the aspect ratio of rectangular substrates under conditions where the fluid was pinned on all sides. We found that increasing the aspect ratio of the substrates (even when holding the substrate area, and liquid volume constant) resulted in higher total restoring forces and torques under both lateral and rotational perturbations. It is also shown that the rotational restoring force is of order the shift restoring force, and should generally be considered in alignment analysis. Finally, parameters from experimental flip-chip devices were used in our simulations to show how current capillary self-alignment schemes can benefit from using rectangular substrate shapes with aspect ratio greater than one.

Acknowledgements

This thesis is dedicated to the friends and family that made its completion possible. Without your support I would not have had the strength to complete my PhD.

To my parents: I have never forgotten the unwavering support you have given me. My goal has always been to make you proud, I hope this is a small step in that direction.

To Kim: This thesis is as much yours as mine. While I would have gladly dropped it all to follow you around the world, you stayed here and sacrificed tremendously to support me. Je t'aime de tout mon coeur.

To John, Claire, and Bastien: The three of you were a buoy in the sea of chaos that was my PhD. The dinners, climbing trips, and all the support you gave to Kim when I couldn't be around meant the world to me.

To Mike, Rose, Kathy, and William: The four of you have been a second family to me for nearly as long as I can remember. I have always felt blessed to have you in my life.

To my colleagues: There is a bond between PhD students that is hard to describe if you haven't experienced it. Chris, Ming, Clay, Elad, Charles, Angela, Rohini, Allison, Brian, Matt, among others, you will always have a special place in my heart.

Table of Contents

Abstract	ii
Acknowledgements	iv
Table of Contents	v
List of Tables	viii
List of Figures	ix
Chapter 1 Introduction.....	1
1.1. Motivation.....	1
1.2. Thesis overview	2
Chapter 2 Key concepts.....	6
2.1. Wetting and capillarity.....	6
2.1.1. Energy and contact angles (Young’s relation).....	7
2.1.2. Pinned contact lines: The canthotaxis limit.....	8
2.1.2.1. Chemical heterogeneity.....	9
2.1.2.2. Physical heterogeneity	9
2.1.3. Relationship between curvature and pressure (Young-Laplace equation)	10
2.2. Experimental Techniques.....	12
2.2.1. Photolithography.....	12
2.2.2. Surface energy modification through self assembled monolayers.....	14
2.3. The Surface Evolver finite element package	16
2.3.1. Introduction	16
2.3.2. Overview	17
2.3.3. User generated file syntax	19
2.3.4. Dimensional analysis.....	20
2.3.5. Example 1: 2D wire frame	22

	2.3.6. Example 2: cube in free space.....	25
	2.3.7. Example 3: droplet on homogenous substrate	27
Chapter 3	From concave to convex: capillary bridges in slit pore geometry.....	34
	3.1. Introduction.....	34
	3.2. Materials and Methods.....	38
	3.2.1. Fabrication of the substrates.....	38
	3.2.2. Experimental device.....	39
	3.2.3. Formation and characterization of the capillary bridges	41
	3.2.4. Surface Evolver simulations.....	43
	3.3. Results and Discussion	43
	3.3.1. Bridge morphology and scaling	43
	3.3.2. Curvature and capillary force.....	56
	3.4. Conclusion	59
Chapter 4	Curvature of capillary bridges as a competition between wetting and confinement.....	61
	4.1. Introduction.....	61
	4.2. Materials and Methods.....	64
	4.2.1. Simulations.....	64
	4.2.2. Experiments.....	65
	4.3. Results and Discussion	66
	4.3.1. Theory	66
	4.3.2. Overall comparison with experimental data.....	79
	4.4. Conclusions.....	82
Chapter 5	Role of substrate aspect ratio on the robustness of capillary alignment... 	83
Chapter 6	Conclusions.....	104
	6.1. Concluding remarks	104
	6.2. Impact and contributions.....	104
	6.3. Future direction.....	106
References		108
Appendix A	Fabrication and visualization of capillary bridges in slit pore geometry	118

A.1	Introduction.....	118
A.2	Protocol.....	119
A.3	Representative Results:.....	127
A.4	Figures and Tables	130
A.5	Discussion:.....	134
A.6	Table of specific reagents and equipment:.....	137
	Curriculum Vitae	139

List of Tables

Table A1: Specific chemicals and reagents used for the fabrication of MHA functionalized raised PDMS pillars.	137
Table A2: Specific parts used to create experimental 4-axis micro stage and imaging device.	138

List of Figures

Figure 2.1: In the absence of body forces, Young’s relation can be obtained by projecting the liquid vapor surface tension into the x direction and performing a force balance..... 7

Figure 2.2: a) A liquid drop pinned on the interface between substrates with Young’s angle θ_1 and θ_2 . The canthotaxis limit states that the liquid drop will remain pinned so long as $\theta_1 < \theta < \theta_2$. b) A liquid drop pinned on a surface with a chemical and physical heterogeneity with angle β . The canthotaxis limit states that the drop will remain pinned so long as $\theta_1 < \theta + \beta < \theta_2$ 10

Figure 2.3: A capillary bridge between two homogenous plates, with principle radii of curvature R_1 and R_2 . a) front view b) top down view..... 12

Figure 2.4: a) A photolithographic mold is made by spin coating SU-8 polymer onto a silicon wafer, and then shining UV light through a predesigned transparency mask. Liquid PDMS is then poured into the mold and heated until it becomes solid. The PDMS is then removed from the SU-8 mold. b) The resulting 3D PDMS device fabricated in a). The width (W) of the strip were between 250-500 μm , while the length (L) was as long as 70 mm. 14

Figure 2.5: Illustration of forming a MHA SAM on a raised PDMS pillar. a), b) A layer of gold is transferred to PDMS to allow for the binding of the sulfur terminated molecules. c) The substrate is placed in a solution of 1 mM MHA in DMSO, where over the course of 24 hours a self assembled monolayer forms. d) The SAM changes the water contact angle of the gold coated PDMS, making it far more hydrophilic. See appendix A for a detailed experimental protocol. Note the size of the MHA molecules are dramatically increased for visualization and are not to scale. 15

Figure 2.6: a) Starting geometry of wire frame. b) Final shape after frame convergences to its energy minimum. 22

Figure 2.7: A graph of the energy/perimeter vs. surface tension (T) of the 2D wire frame. As predicted by theory, the SE points form a straight line. Error < 0.0016% 24

Figure 2.8: a) Starting geometry of cube in free space. b) Final shape after cube convergences to its energy minimum. As predicted, it is a perfect sphere. 25

Figure 2.9: Energy vs. Volume graph of a cube in free space with surface tension term T set to one. Error < 0.001%..... 26

Figure 2.10: a) Starting geometry of a liquid cube on a homogeneous substrate. b) Final shape after evolution.	27
Figure 2.11: Energy vs. Volume of a liquid drop on a homogeneous substrate. Error < 0.0026%.	32
Figure 2.12: Area vs. Volume for a liquid drop on a homogeneous substrate. Since SE includes the area of all facets in its calculation, we must subtract out the area of the substrate. Note that since $T_L = 0$ the substrate does not contribute to the total energy of the system and Figure 2.11 remains correct. Had a different contact angle been chosen, this would not have been true.	33
Figure 3.1: Experimental parameters for the characterization of capillary bridges in slit pore geometry. (a) Three quarters view, (b) Side view and (c) Front view. Images were rendered in Cinema 4D using data from Surface Evolver simulations.....	37
Figure 3.2: Schematic of experimental device. x, y, z, and ϕ stages allow for four special degrees of freedom.....	40
Figure 3.3: Picture of complete experimental set up. The PDMS substrates are held at a variable distance apart through a combination of x,y,z and rotation stages. A separate set of microstages (far right) holds the syringe to introduce the liquid into a narrow gap to create the capillary bridge in a slit-pore geometry. A CCD camera (pictured left) is used to image the resulting capillary bridges as the pore separation is changed. The resulting images can then be analyzed in the open source image analysis software ImageJ.....	41
Figure 3.4: (a) Aspect ratio (L/W), and (b) pinning angle (α) as a function of the bridge height (H) taken for different volumes and strip widths. The data points are from experimental measurements and the solid lines are the results of the Surface Evolver simulations. The dashed line in the inset corresponds to the aspect ratio of a rectangular box (i.e. $\alpha = 90^\circ$), when the experimental data is above the dashed line the pinning angle must be less than 90° and when it is below the dashed line the pinning angle must be greater than 90° , as illustrated by the schematic.	45
Figure 3.5: Hysteresis in the measurement of the length for a capillary bridge with width = 0.35 mm and volume = $1\mu\text{L}$. The liquid was induced between the substrates at 0.2 mm, then the separation was increased to 1.1 mm, and decreased back down to 0.2 mm.	46
Figure 3.6: Experimental (a, b) and simulated (c, d) images of liquid bridges with volume = $2.5\mu\text{L}$, strip width = 0.5 mm and height i) 0.3, ii) 0.5, iii) 0.7, iv) 0.9 and v) 1.1	

mm. The side view showing the bridge length is shown in (a) and (c) and the front view showing the pinning angle is shown in (b) and (d)..... 48

Figure 3.7: Scaling of the length (a) and of the pinning angle (b) as the height of the capillary bridge is increased. The data points correspond to experimental results and the solid lines correspond to the Surface Evolver simulations. 50

Figure 3.8: Volume of liquid bridges normalized by the “box” ($\alpha = 90^\circ$) volume vs. H/W . The data collapses when the pinning angle is near 90° , and deviates as α increases or decreases from this value..... 51

Figure 3.9: Simulated data for pinning angle (α) at various positions (X) along the length of liquid bridge (width = 0.35 mm, volume = $1\mu\text{L}$)...... 52

Figure 3.10: (a) Mean curvature normalized by width and (b) pinning angle vs. H/W for a large range of V/W^3 . Bridges with lower reduced volumes deviate from universal behavior at lower H/W 54

Figure 3.11: (a) Change in mean curvature (scaled by the width) as the bridge height is increased. A sign change from negative to positive occurs at around $H/W = 1.0$. (b) Normalized total force and normalized Laplace and surface tension components of the capillary force between the substrates. The curves are obtained from Surface Evolver simulations. The inset shows the projections of the surface tension (F_{ST}) and Laplace (F_{Laplace}) force components..... 55

Figure 3.12: Simulated data for Volume = $2.5\mu\text{L}$, width = 0.5 mm. The normalized height at which the sign change in curvature occurs decreases as the wetting angle increases..... 59

Figure 4.1: Capillary bridge in slit pore geometry. (a) Three quarters view, (b) Side view and (c) Front view. Images were rendered in Cinema 4D using data from Surface Evolver simulations. Representative experimental results for the length (d) and the pinning angle (e) are also shown. 64

Figure 4.2: Schematic of the capillary bridge. The theory estimates the curvature at points M and N on the bridge. 68

Figure 4.3: Section of the capillary bridge in the C_1C_2 -plane (see Figure 4.2d for the definition of the plane and coordinate system) extracted from the minimal energy shape obtained from Surface Evolver simulations at different heights and for a wetting angle of a) 15° , and b) 60° . Also shown is the transition from a bridge with negative mean curvature to a bridge with positive mean curvature: the width of the bridge is less than the

width of the strip at low H/W and increases to become larger than the width as H/W increases..... 72

Figure 4.4: Comparison between theory and simulations to test the translational invariance assumption for capillary bridges formed on strips with three different wetting angles. The mean curvature normalized by the width of the strip, κW , has been obtained in two separate ways. The lines correspond to the mean curvature obtained from the Laplace pressure of the capillary bridge based on Surface Evolver simulations while the data points represent the predictions based on extracting r at point M from Surface Evolver simulations and using Equation 4.1..... 73

Figure 4.5: Individual radii of curvature (in mm-1) calculated at a,c) point N, and b) point M. The data points correspond to curvatures calculated based on the Surface Evolver simulations for a width of 0.5 mm and a volume $(V/W^3)=20$. The radii of curvature were obtained for three different contact angles for the solid strip supporting the bridge (with \bullet for $\theta = 15^\circ$, \blacksquare for $\theta = 30^\circ$, and \blacktriangle $\theta = 60^\circ$). The solid lines correspond to theoretical predictions for the three wetting angles considered here. 75

Figure 4.6: Mean curvature normalized by the width (κW) as a function of height for different wetting angles (with \bullet for $\theta = 15^\circ$, \blacksquare for $\theta = 30^\circ$, and \blacktriangle $\theta = 60^\circ$). The lines represents predictions from the theory for the mean curvature at point N ($\kappa W = 1 - \cos\theta HW$). The data points corresponds to the results of Surface Evolver simulations with volume $V/W^3 = 20$ and width $W = 0.5$ mm. 78

Figure 4.7: Mean curvature normalized by the width (κW) as a function of height for different wetting angles (with \bullet for $\theta = 15^\circ$, \blacksquare for $\theta = 30^\circ$, \blacktriangle $\theta = 60^\circ$ and \blacklozenge $\theta = 90^\circ$). The lines represents predictions from the theory for the mean curvature at point N ($\kappa W = 1 - \cos\theta HW$).The data points corresponds to the results of surface evolver simulations with volume $V/W^3 = 20$ and width $W = 0.5$ mm. 79

Figure 4.8: Comparison between experiments, SE simulations, and theory. a) experimental results along with prediction for the theory (line). The conditions for the experiments are \blacktriangle for $V=1\mu\text{L}$ and $W = 0.25$ mm, \bullet for $V = 1\mu\text{L}$ and $W = 0.35$ mm, \blacklozenge for $V = 2.5 \mu\text{L}$ and $W = 0.5$ mm, and \blacksquare for $V = 5 \mu\text{L}$ and $W = 0.5$ mm. b) Comparison between Surface Evolver simulation, theory, and experiments for $V = 2.5 \mu\text{L}$ and $W = 0.5$ mm. The solid black line corresponds to the theory, the dashed line to the simulation without tilt, and the thin red line the simulation with a 0.1 degree tilt. 81

Figure 5.1: (a) Top down view of substrates under a rotational perturbation (ϕ) and (b) frontal view of substrates under a shift perturbation (S). F_w is the shift restoring force associated with a displacement S..... 85

Figure 5.2: Simulated restoring torque for different rotation angles obtained for capillary bridges formed between substrates of different aspect ratios. The volume of liquid is 4.9 μL and the substrate area is 25 mm^2 . The solid lines are predictions from Equation 5.1. Dashed lines represent maximum local pinning angle observed. 88

Figure 5.3: View of capillary bridge normal to the width of the top substrate when $\phi = 10^\circ$. $L/W = 4$, $V = 9.8 \mu\text{L}$ 88

Figure 5.4: Simulated equilibrium heights vs. liquid volume over substrate area for different aspect ratios, volumes, and substrate areas. The solid line represents a slope of 1. 89

Figure 5.5: Schematic illustrating the assumptions present in deriving Equation 5.1. a) Top down view of flip-chip device ($\phi = 0$). b) Front view of flip-chip device (normal to width, $\phi > 0$). This perspective shows the pinning angle of the liquid bridge when the liquid vapor interface is assumed to be flat. 91

Figure 5.6: Maximum (a) shift normal to the length, and (b) rotation angle, ϕ , for substrates of different aspect ratios. Points represent experimental data while error bars represent the standard deviation of values obtained from multiple trials over three separate sample sets for each aspect ratio. The solid lines are meant to guide the eye, while the dashed lines represent pinning angle values obtained from simulations. Volume = 39 μL and substrate area = 1 cm^2 94

Figure 5.7: Simulated restoring torques and shift restoring forces when $\alpha = 180^\circ$. (a) Torque values normalized by surface tension and substrate area. (\blacktriangle) $V = 4.9 \mu\text{L}$, $A = 25 \text{mm}^2$, $H = 196 \mu\text{m}$. (\bullet) $V = 9.8 \mu\text{L}$, $A = 25 \text{mm}^2$, $H = 392 \mu\text{m}$. (\circ) $V = 9.8 \mu\text{L}$, $A = 50 \text{mm}^2$, $H = 196 \mu\text{m}$. (\blacklozenge) $V = 4.9 \mu\text{L}$, Perimeter = 20 mm. Inset: rotation angle at $\alpha = 180^\circ$. The lines are meant to guide the eye. (b) Shift restoring forces. Data points represent Surface Evolver simulations while lines represent theoretical predictions. F_w and F_L are the restoring forces when the substrate is shifted normal to its width or length respectively. The inset shows the total translational force $F_{\text{Trans}} = F_w + F_L$ normalized by the surface tension and substrate perimeter (P). 96

Figure 5.8: (a) Simulated restoring torque for substrates with area = 1 cm^2 , volume = 39 μL , and different shapes. (b) projected area increase of substrates with area = 1 cm^2 , and different shapes vs. rotation angle. 98

Figure 5.9: Translational force (F_{trans}) over rotational force (F_{rot}) for different volumes and areas at $\alpha = 180^\circ$. Data points represent Surface Evolver simulations while lines are

meant to guide the eye. (▪) $V = 4.9 \mu\text{L}$, $A = 25 \text{ mm}^2$, $H = 196 \mu\text{m}$. (•) $V = 9.8 \mu\text{L}$, $A = 25 \text{ mm}^2$, $H = 392 \mu\text{m}$. (●) $V = 9.8 \mu\text{L}$, $A = 50 \text{ mm}^2$, $H = 196 \mu\text{m}$. Inset shows $F_{\text{trans}}/F_{\text{rot}}$ at $\alpha = 150^\circ$ 100

Figure 5.10: Experimental and simulated shift restoring forces for substrates with different aspect ratios. The data points correspond to the experimental data of Josell et. al.⁸⁶ for shift restoring force of circular pads with area = 0.32 mm^2 , liquid volume = $0.029 \mu\text{L}$, and surface tension = 0.4 N/m . Black, red, and blue lines represent simulated shift forces for rectangular substrates with aspect ratio 1, 2, and 4 respectively while keeping the same area, liquid volume, and surface tension of the experimental points. Solid lines represent shift forces normal to the substrate's length, while dashed lines represent shift forces normal to substrate's width. 102

Figure A.1: Picture of complete experimental set up. The PDMS substrates are held at a variable distance apart through a combination of x,y,z and rotation stages. A separate set of microstages (far right) holds the syringe to introduce the liquid into a narrow gap to create the capillary bridge in a slit-pore geometry. A CCD camera (pictured left) is used to image the resulting capillary bridges as the pore separation is changed. The resulting images can then be analyzed in the open source image analysis software ImageJ..... 130

Figure A.2: PDMS substrate with 20nm Au layer functionalized by a MHA self-assembled monolayer. The low water contact angle shows that the procedure was successful. The inset shows a drop on a raised functionalized PDMS/Au pillar..... 131

Figure A.3: Raised PDMS pillar after transfer of 20nm Au layer. a) Successful transfer. b) Tearing due to lateral motion of the PDMS substrate during the transfer process. c) Cracking caused by the bending of the PDMS substrate during the transfer process. ... 132

Figure A.4: Images of capillary bridges on pillars in the experimental device. a) Field of view parallel to the length of the pillar. b) Field of view perpendicular to the length of the pillar. c) Shows the filling process of the slit pore (same perspective as b). The minor graduation of the ruler in b) and c) is $500 \mu\text{m}$ 133

Introduction

1.1. Motivation

Capillary bridges are important for a myriad of natural and industrial processes. For example, the filling or draining of porous materials, such as water penetration into soil¹, or oil recovery from natural wells² is dictated by capillary forces. Additionally it is the liquid bridges between granular materials that give wet sand the structure needed to make sand castles³⁻⁶. In shorebirds, asymmetric capillary bridges in the beak are used to catch and transfer prey from the surrounding water to their throats⁷⁻⁹.

In small scale scientific applications where surface forces dominate over body forces, such as in microelectromechanical systems (MEMs) and atomic force microscopy, strong capillary forces due to condensation can cause unwanted stiction¹⁰⁻¹⁵. Conversely, improvements in microfabrication techniques allow for the creation of surfaces with physical and chemical heterogeneities that can be used to pin the liquid, and subsequently harness capillary forces in ingenious ways. For example, chemical patterning has been utilized to create “wallless” microfluidic channels¹⁶⁻¹⁸. Also, careful substrate design can yield surfaces with predetermined capillary forces or morphologies, allowing for massively parallel 2D¹⁹⁻²¹ and 3D²²⁻²⁵ self assembly of micro and nanoscale devices.

The ubiquitous nature of capillary bridges between solid substrates has motivated an impressive array of theoretical²⁶⁻²⁹, experimental³⁰⁻³⁵, and simulated³⁶⁻³⁸ investigations aimed at predicting the morphology (and subsequent forces) of axisymmetric bridges between chemically and physically homogenous plates, spheres or cylinders. A consequence of the high levels of symmetry in these systems is often elegant analytical solutions for the bridge profile and forces. As mentioned above however, many systems exploit asymmetries in liquid morphologies through pinning of the triple contact line to achieve specific bridge profiles or forces. One of the simplest model systems that breaks this symmetry is that of a capillary bridge in a slit pore geometry, where the bridge spans two long narrow rectangular strips. The slit pore is useful as a model system in fluid dispensing schemes³⁹, bio inspired adhesion³⁶, condensation and nucleation⁴⁰⁻⁴⁴ or for the passive alignment of capillary based electronic packaging^{20, 45-51} among others.

1.2. Thesis overview

This thesis summarizes experimental and simulated works aimed at exploring changes in morphology and forces of pinned or partially pinned capillary bridges between rectangular solid substrates (aspect ratio (length/width) > 1). The aspect ratio, height, surface chemistry, and alignment (lateral and rotational) are varied and the resulting liquid bridges analyzed.

Chapter 2 is meant as a brief review of topics needed to understand the core of the work in this thesis. First, an introduction to key concepts in wetting are presented, then a description of experimental techniques, followed by an introduction to the finite element

program used to model our capillary systems (Surface Evolver) is presented. Three simple examples are worked through to explain and verify how Surface Evolver calculates parameters such as energy and area.

In chapter 3 (peer reviewed publication⁵² reprinted with permission) we investigate the morphological evolution of non-axisymmetric capillary bridges in slit-pore geometry as the height of the pore and aspect ratio of the bridge is varied. The liquid bridges are formed between two hydrophobic surfaces patterned with hydrophilic strips. The aspect ratio of the capillary bridges (length/width) is varied from 2.5 to 120 by changing the separation between the surfaces, the width (W) of the strips, or the fluid volume. As the bridge height is increased, the aspect ratio decreases and we observe a large increase in the mean curvature of the bridge. More specifically, the following counterintuitive result is observed: the mean curvature of the bridges changes sign and goes from negative (concave bridge) to positive (convex bridge) when the height is increased at constant volume. These experimental observations are in quantitative agreement with Surface Evolver simulations. Scaling shows a collapse of the data indicating that this transition in the sign of the Laplace pressure is universal for capillary bridges with high aspect ratios. Finally, we show that the morphology diagrams obtained from our 3D analysis are considerably different from those expected from a 2D analysis.

In chapter 4 (peer reviewed publication⁵³ reprinted with permission) we consider the shape evolution of non-axisymmetric capillary bridges in slit pore geometry as the pore height is increased at constant volume. Experiments and finite element simulations using Surface Evolver have shown that as the height of the pore is increased the mean

curvature of the bridge, and hence Laplace pressure, changes its sign from negative to positive. Here we propose an intuitive explanation of this surprising phenomenon. We suggest that it is the balance between the confinement and the wetting properties of the supporting strips that causes the change in sign of the Laplace pressure. The theory proposed relies on three simple approximations, which are tested individually and are each in good agreement with experiments and simulations in the regime where the curvature transition from negative to positive takes place. Theoretical arguments take into account only the wetting properties and geometry of the system (the width and height of the pore). Along with the formula for the curvature, we derive also the formula for the pinning angle of the capillary bridge which is also verified experimentally.

Chapter 5 (manuscript accepted to *Applied Physics Letters*) discusses capillary forces associated with liquids bridged between solid substrates that are exploited to align and assemble micro- and nanoscale devices. The magnitude of these forces plays a critical role in minimizing substrate misalignment, and therefore should be controlled for robust and reliable fabrication process. We explore through simulation and experiment the role of the substrate aspect ratio (L/W) on capillary restoring forces and torques. Simulations show that increasing the aspect ratio of the substrates increases the capillary torques and forces when the substrates are misaligned through either lateral or rotational perturbations. The effect of substrate area, perimeter, and liquid volume are also systematically explored to show that the increase in restoring torque is caused by an increase in aspect ratio. A simple theoretical model based on the surface tension and geometric shape of the system shows excellent agreement with *Surface Evolver* simulations. Finally, parameters from experimental flip-chip devices are used in our

simulations to show how current capillary self-alignment schemes can benefit from using rectangular substrate shapes with aspect ratio greater than one.

Chapter 6 highlights my contributions in understanding the nature in which the morphology and forces of pinned and partially pinned capillary bridges change as the geometry and the orientation of the substrates are varied. Potential future directions that could extend our model to more complicated geometries are discussed.

In appendix A (peer reviewed publication⁵⁴ reprinted with permission), the details necessary to repeat the experiments presented in chapters 3 and 4 are described. The experimental protocol followed to fabricate the raised chemically heterogeneous substrates, along with a description and table of parts of the custom experimental device used to vary the height of the slit pore is presented. Representative results of the substrate fabrication process at critical steps in the protocol are presented and discussed as well.

Key concepts

2.1. Wetting and capillarity

When two materials come into contact, there is a cost in energy associated with creating their interface. When the materials themselves are deformable (soft solids, liquids, or vapors) they can adjust to change the sizes and shapes of these interfaces to minimize the total energy of the system. In the case of solid-liquid-vapor (or solid-liquid-liquid) systems, the interplay between the interfaces of the materials can be described by the wetting characteristics of the liquid on the solid. For example, when a liquid such as water is placed on a surface like gold, the amount of energy required to create the air-gold interface is larger than the amount of energy required to form the air-water interface, and the liquid spreads onto the gold. Therefore the gold surface would be considered wetting. When the reverse case is true (for a low energy material such as Teflon) the water contracts to minimize its surface contact with the air, creating a larger air-solid interface. Therefore a surface such as Teflon is considered non wetting. The purpose of this section is to give the reader a basic understanding of the key concepts of wetting that are needed to understand this thesis

2.1.1. Energy and contact angles (Young's relation)

In the absence of body forces (as in all the cases presented in this thesis) we can write a general form of the energy of a solid-liquid-vapor system in terms of surface tension and area components

$$E = \gamma_{SL}A_{SL} + \gamma_{LV}A_{LV} + \gamma_{SV}A_{SV} \quad (2.1)$$

Where γ_{SL} , γ_{LV} , γ_{SV} are the surface energies for the solid-liquid, liquid-vapor, and solid-vapor interfaces respectively, and A_{SL} , A_{LV} , A_{SV} are the areas of the corresponding interfaces. Knowing the exact values of the solid-vapor and solid-liquid surface tension components often proves difficult, so a way to redefine our energy in terms of more practical variables is needed. In general, this is done by relating the surface tension components to the contact angle (the interior angle the liquid drop makes with the solid substrate) by means of a force balance. This is known as Young's relation (Figure 2.1).

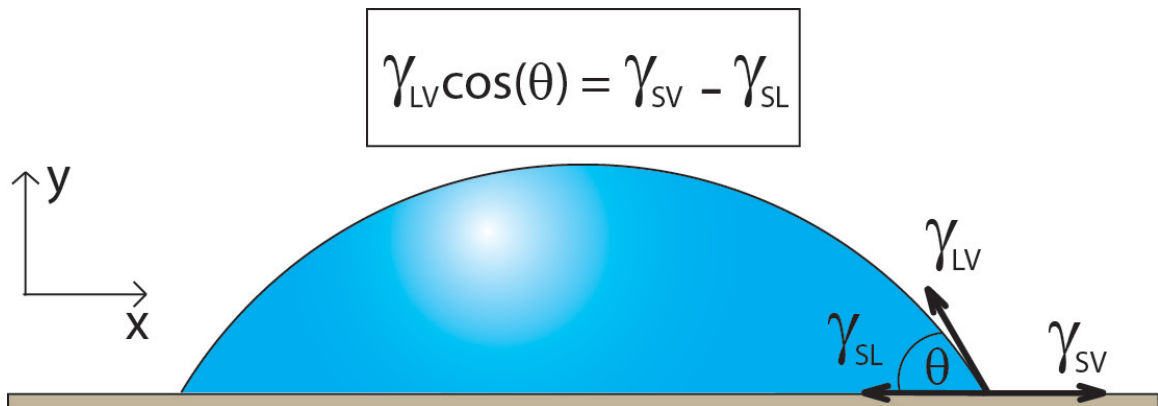


Figure 2.1: In the absence of body forces, Young's relation can be obtained by projecting the liquid vapor surface tension into the x direction and performing a force balance.

Plugging this into equation (2.1) we obtain a new relation.

$$E = \gamma_{LV} (A_{LV} - A_{LS} \cos \theta) + \gamma_{SV} (A_{LS} + A_{SV}) \quad (2.2)$$

$$\gamma_{SV} (A_{LS} + A_{SV}) = \text{constant} \quad (2.3)$$

Equation 2.3 is constant since any increase in the liquid-solid area will correspond to an equivalent decrease in the solid-vapor area and vice versa. Since this constant is of no particular importance, and properties like forces and torque depend only on changes in energy, we can rewrite our equation.

$$E = \gamma_{LV} (A_{LV} - A_{LS} \cos \theta) \quad (2.4)$$

This form of the energy is much more convenient, as it relies only on the liquid-vapor surface tension, the contact angle the liquid makes with the surface, and the area of the liquid-vapor and liquid-solid interfaces respectively.

2.1.2. Pinned contact lines: The canthotaxis limit

In the model system described in Figure 2.1, the solid substrate is assumed to be perfectly smooth and chemically homogenous. For the work described in this thesis however, it is often the case that liquid in contact with a surface is pinned due to a physical or chemical heterogeneity. It is therefore worthwhile to discuss the conditions for when a liquid will stay pinned or break free from a heterogeneity.

2.1.2.1. Chemical heterogeneity

When a liquid drop is placed on a surface with a wettability contrast (Figure 2.2a) the liquid will at first cover only the region of higher surface energy (lower Young's angles, red area in Figure 2.2). As the volume is increased however, the liquid will pin to the heterogeneity between the lower and higher surface energy surfaces. As the volume increases further, the drop will stay pinned until its contact angle exceeds that of the lower surface energy region (Figure 2.2a). This is known as the canthotaxis limit⁵⁵. Once this is passed, the liquid will continue to spread onto the lower surface energy region. Therefore the stronger the wetting contrast, the stronger the pinning boundary of the surface.

2.1.2.2. Physical heterogeneity

The canthotaxis limit is modified when a physical heterogeneity is present, such as a step (Figure 2.2b). In this case, the liquid drop will remain pinned to the higher surface energy regime until the contact angle surpasses the step angle plus the Young's angle on the side of the pillar. In short, this implies that to prevent spreading of the liquid drop to the lower surface energy regions, a strong wetting contrast and a sharp physical boundary are advantageous.

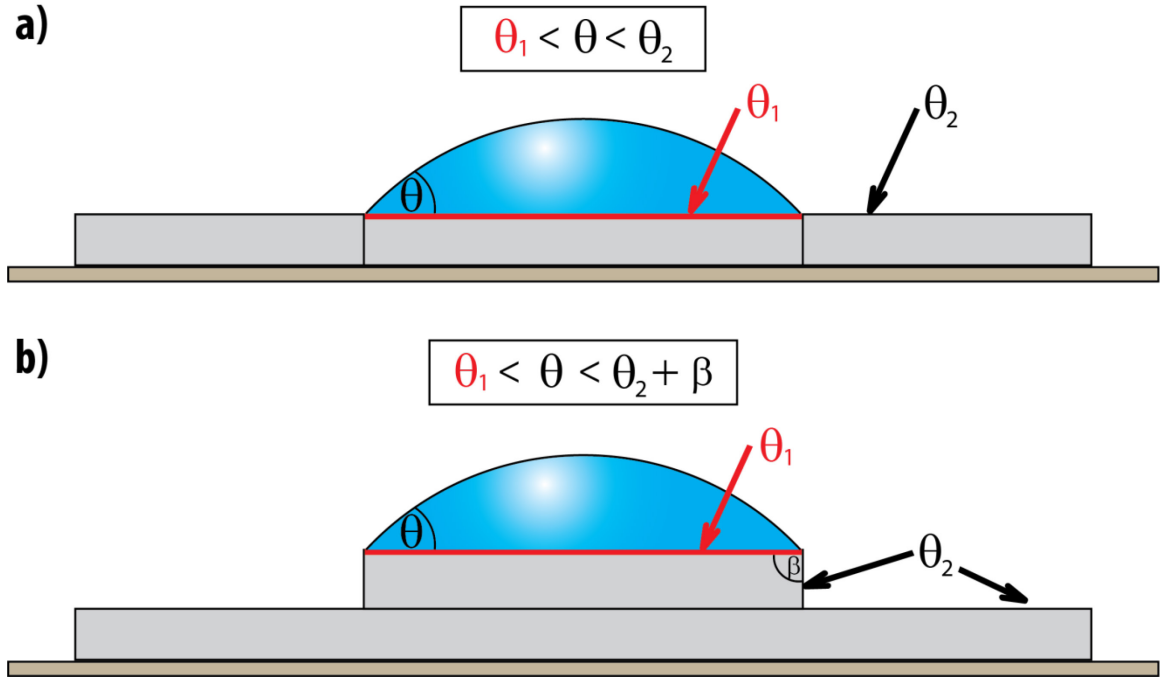


Figure 2.2: a) A liquid drop pinned on the interface between substrates with Young's angle θ_1 and θ_2 . The canthotaxis limit states that the liquid drop will remain pinned so long as $\theta_1 < \theta < \theta_2$. b) A liquid drop pinned on a surface with a chemical and physical heterogeneity with angle β . The canthotaxis limit states that the drop will remain pinned so long as $\theta_1 < \theta + \beta < \theta_2$.

2.1.3. Relationship between curvature and pressure (Young-Laplace equation)

The difference in pressure across a liquid interface can be related to the mean curvature of the interface through the Young-Laplace equation.⁵⁶

$$\Delta P = 2\kappa\gamma \quad (2.5)$$

Where κ is the mean curvature of the liquid and γ is the surface tension. The pressure drop and mean curvature are defined as (see Figure 2.3):

$$\Delta P = P_L - P_A$$

$$\kappa = \frac{1}{2} \left(\frac{1}{R_1} + \frac{1}{R_2} \right) \quad (2.6)$$

Where P_L is the pressure inside the liquid and P_A is the atmospheric pressure. For the case of a liquid drop on a homogeneous plate, the mean curvature will simply be the radius of the spherical cap made by the liquid ($R_1 = R_2$). When the liquid is bridged between two surfaces as in Figure 2.3, the radii of curvature will not be the same. The force that the liquid bridge exerts on the substrates in Figure 2.3 will be given by the pressure drop (known as the Laplace pressure) times the contact area of the liquid on the substrate.

$$F_z = \Delta P A = \pi R_1^2 \gamma \left(\frac{1}{R_1} + \frac{2 \cos(\theta)}{H} \right) \quad (2.7)$$

Often, the height of the capillary bridge will be much smaller than the radius of the drop projected onto the substrate ($H \ll R_1$). In this case, Equation 2.7 reduces to:

$$F_z = \pi R_1^2 \frac{2\gamma \cos(\theta)}{H} \quad (2.8)$$

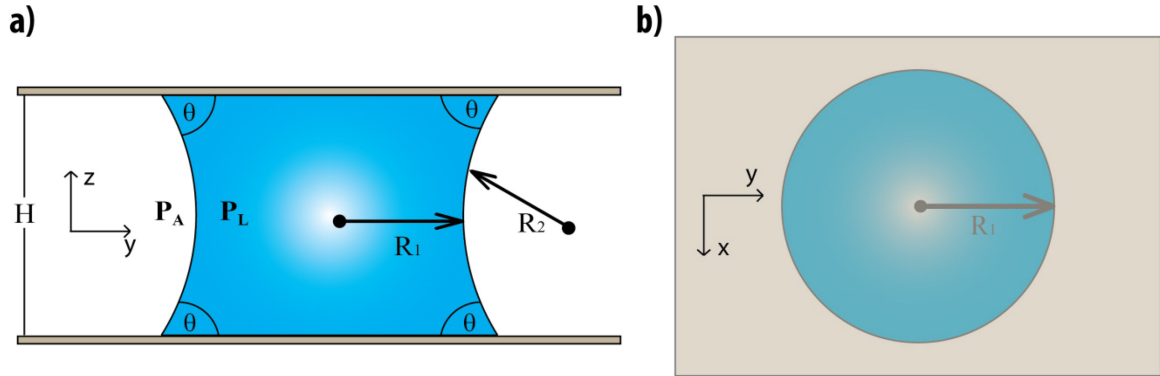


Figure 2.3: A capillary bridge between two homogenous plates, with principle radii of curvature R_1 and R_2 . a) front view b) top down view.

These forces can be deceptively high at small separations. If $H = 10 \mu\text{m}$, $R_1 = 1 \text{ cm}$ and $\theta = 0^\circ$, the resulting capillary force will be approximately 1 N. It is for this reason that unwanted capillary condensation or liquid bridging between components can ruin small scale devices.

2.2. Experimental Techniques

2.2.1. Photolithography

Photolithography is a micro fabrication technique that uses specified wave lengths of light to selectively crosslink sections of a photocurable polymer. Generally, a photoresist is spun onto a flat surface (glass or silicon wafer) and ultra violet light is shown through a transparency mask. The sections of the resist exposed to the light either become soluble in resist developer (positive photoresist) or become insoluble (negative

photoresist) depending on the specific polymer used. The soluble sections of the resist are then dissolved away and a raised image (either positive or negative) of the mask design is left on the wafer. The wafer/resist can then itself be used as a mold for a thermocurable polymer such as polydimethylsiloxane (PDMS) to create 3D structures. The feature sizes achievable by photolithography are limited by the resolution of the mask and the wavelength of the light used in the crosslinking process, making feature sizes smaller than approximately 1 μm difficult to achieve. The thickness of the photoresist layer is determined by the viscosity of the polymer and the speed at which it is spun onto the wafer. Typical resist thicknesses are in the range of 1-100 μm . Figure 2.4 depicts an SU-8/silicon wafer photolithographic device being used as a mold for creating 3D PDMS substrates with long raised channels.

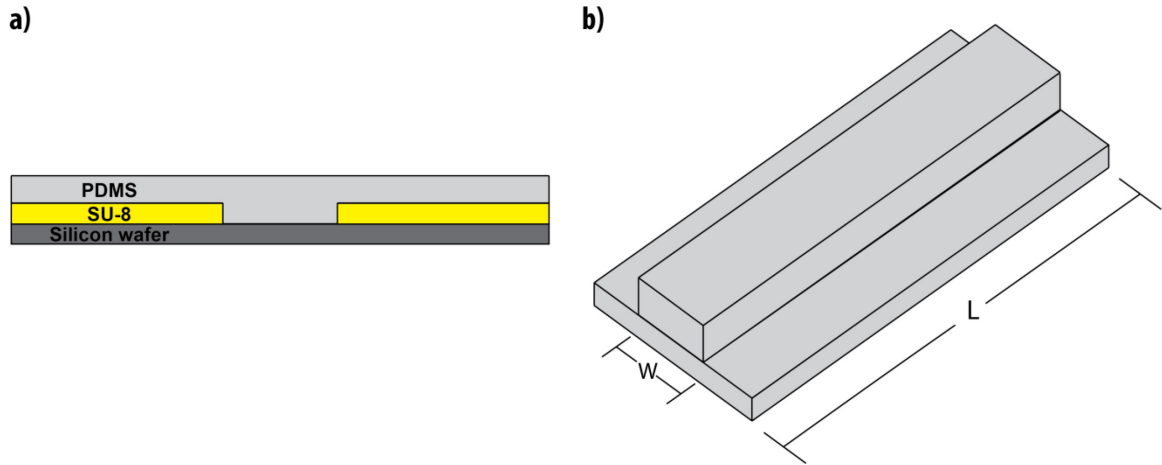


Figure 2.4: a) A photolithographic mold is made by spin coating SU-8 polymer onto a silicon wafer, and then shining UV light through a predesigned transparency mask. Liquid PDMS is then poured into the mold and heated until it becomes solid. The PDMS is then removed from the SU-8 mold. b) The resulting 3D PDMS device fabricated in a). The width (W) of the strip were between 250-500 μm , while the length (L) was as long as 70 mm.

2.2.2. Surface energy modification through self assembled monolayers

It is often desirable to change the wetting characteristics of a specific surface to fit a particular application. For example, the ease of use and relatively low cost of PDMS makes it a popular choice for fabrication of 3D micro structures, but its low surface energy makes it hydrophobic, resulting in poor wettability (high contact angle) with high surface energy liquids like water. One way to change the surface properties of a device is

to deposit a monolayer layer of molecules onto the surface that differ in wetting properties from the device itself. When the device is exposed to the molecules in either a liquid or vapor medium, it becomes entropically favorable for the molecules to form a dense, ordered monolayer on the surface of the device⁵⁷⁻⁵⁸ effectively changing its surface chemistry. This is known as a self assembled monolayer (SAM). For the devices used in chapter 3 and 4 of this thesis, mercaptohexadecanoic acid (MHA) molecules are deposited onto gold covered PDMS to make the surfaces hydrophilic. The gold is necessary to bind the sulfur terminated molecules to the PDMS. Figure 2.5 describes this process.

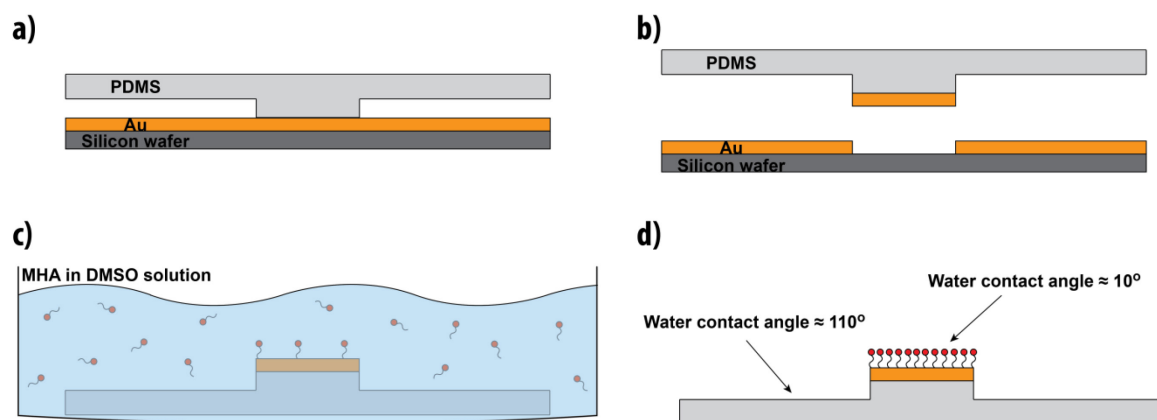


Figure 2.5: Illustration of forming a MHA SAM on a raised PDMS pillar. a), b) A layer of gold is transferred to PDMS to allow for the binding of the sulfur terminated molecules. c) The substrate is placed in a solution of 1 mM MHA in DMSO, where over the course of 24 hours a self assembled monolayer forms. d) The SAM changes the water contact angle of the gold coated PDMS, making it far more hydrophilic. See appendix A for a detailed experimental protocol. Note the size of the MHA molecules are dramatically increased for visualization and are not to scale.

2.3. The Surface Evolver finite element package

[This section has been adapted (and expanded) from a term paper for the course: Finite Element Methods (EN.5730.730)]

2.3.1. Introduction

In the field of interfacial and surface sciences, the Surface Evolver⁵⁹ (SE) finite element package has received much attention for its utility as an accurate, and easy to use tool to numerically analyze surface forces, energy and geometries. In its essence, the SE package constructs a geometric model based on a set of inputs from the user. Then, through many iterations, SE perturbs the system under a set of predetermined constraints until it reaches a global energy minimum. After each iteration, the systems volume, area, pressure, and energy can be queried.

Since the only information required by the user is desired constraints, nodal position, and connectivity, very complex problems are accessible to investigators with little knowledge of programming or the finite element method. While a low barrier to entry is valuable, a lack of understanding can lead to a misinterpretation or distrust in results. For these reasons it is important to have a basic understanding of both the mathematical model used in the coding and the limitations of such software. It is the purpose of this section to provide the reader with such an understanding. A general introduction to SE will be presented, in which the mathematical model and computation procedures of the software will be discussed.

2.3.2. Overview

SE's principle task is to take a predetermined geometry and minimize its total energy under a set of given constraints. In general, there are three "types" of energy that SE can calculate. Those associated with body forces such as gravity,

$$E_B = \iiint_V \rho \vec{g} \vec{z}(x, y) \cdot d\vec{V} \quad (2.9)$$

those associated with surface forces,

$$E_S = \iint_S \vec{T}(x, y, z) \cdot d\vec{S} \quad (2.10)$$

and those associated with line forces.

$$E_L = \int_{\partial S} \vec{T}_L(x, y, z) f(x, y, z) \cdot d\vec{l} \quad (2.11)$$

Where ρ is the body density, g is gravitational acceleration, $\vec{z}(x, y)$ is a vector position function, and T and T_L represent surface energy and line tension respectively. $f(x, y, z)$ is a scalar position function. In practice these integrals are discretized based on the density of the mesh, which is triangular in nature and is created by connecting neighboring nodes with vertices:

$$\int F(x) dx \approx \sum_1^n F_n(x_n) \quad (2.12)$$

Where n is the number of nodes. In principle, SE does not need the ability to solve volume integrals such as those in equation 2.9, since they can be expressed as area integrals using the divergence theorem:

$$\iiint_V (\vec{\nabla} \cdot \vec{F}) dV = \iint_S \vec{F} \cdot \vec{n} dS \quad (2.13)$$

It should be noted that one could not further decrease the order of these integrals using Stokes theorem, since they would then run into the problem that:

$$\vec{\nabla} \cdot (\vec{\nabla} \times \vec{F}) = 0 \quad (2.14)$$

Therefore it is still necessary that SE have the ability to solve both area and line integrals. Once the energy of each node is found, a nodal force vector is constructed by taking the negative gradient of that energy:

$$\vec{F}_n = -\vec{\nabla} E_n \quad (2.15)$$

Each node is allowed to move in the direction of its own prescribed force by a magnitude that is calculated internally by SE. (Note: the user is capable of setting this “scale” factor if desired).

This process is known as the method of gradient descent and is repeated arbitrarily until the user is satisfied the system is at a minimum. Since there is no definite “convergence test” it can often be difficult to determine whether or not the model is sufficiently refined. Simply running the code for a fixed time is not sufficient, since convergence speed can decrease as the system gets closer to equilibrium. To aid with this, SE provides the ability to converge quadratically using the “*Hessian*” command. Naturally, this allows for much faster convergence, but care must be taken to ensure that the Eigen values of the system are greater than zero (negative Eigen values correspond to movement *up* the gradient) so as not to cause the model to diverge. The command “*eigenprobe n*” lists the quantity of Eigen values in the system below, equal to, and

greater than the value n . This can be used to check if it is appropriate to use Hessian convergence.

It is also up to the user to insure that the system is not at a local, but a global, energy minimum. While this can be quite difficult for complex systems, SE has two built-in commands to aid with this. The first is “*jiggle*”, which perturbs all the nodes in a random direction by a prescribed magnitude. This allows models in shallow energy wells to be “kicked” into lower energy configurations. The second is “*saddle*” which finds the largest negative Eigen value of the system and moves a prescribed amount in that direction. This is a more focused way of accomplishing the same task as *jiggle*. In the end however, it is up to the user to define both convergence and minima criteria.

2.3.3. User generated file syntax

SE input files begin with a list of user defined variables. Strings can be set to values using the “PARAMETER string= ###” command and strings can be set to equations using “#define string = eqn”. Certain internally defined variables such as “gravity constant = #” exist for common used features such as gravity. Next, user defined constraints are listed (such as level set constraints). Then, the number, coordinates, and constraints of the nodes are defined under the “vertices” heading. Element edges are defined similarly under the “edges” heading and are connected together to form faces in the “faces” section. It is often useful to constrain a system by its volume, the “body” section allows the user to combine faces into a closed body and prescribe its volume. While this covers most of what is used for the purposes of this

thesis, the above description is far from exhaustive. A list of complete user file syntax can be found in the surface evolver manual, available free of charge online⁶⁰.

2.3.4. Dimensional analysis

Surface Evolver natively works in dimensionless units, meaning it is up to the user to define a unit convention for their particular system and apply it to their code. It is the purpose of this section to describe to the reader how to convert between unit systems in Surface Evolver.

In practice, one usually picks a characteristic length scale when they define the initial geometry in their input file, and then builds other dimensional quantities around that length. For example, if one defines a square surface to have the vertices $(-0.5, -0.5)$, $(-0.5, 0.5)$, $(0.5, -0.5)$ and $(0.5, 0.5)$ then the dimensionless length \bar{L} of a side, and the dimensionless area \bar{A} will equal 1. If we were to choose our characteristic length L_o to be 1 cm, then we could convert our dimensionless surface evolver output \bar{L} to dimensional value L through the equation

$$\bar{L} = \frac{L}{L_o} \tag{2.16}$$

Similarly we can calculate our dimensional areas and volumes by

$$\begin{aligned} \bar{A} &= \frac{A}{A_o} \\ \bar{V} &= \frac{V}{V_o} \end{aligned} \tag{2.17}$$

where

$$A_o = L_o^2 \quad (2.18)$$

$$V_o = L_o^3$$

From here, the energy can be nondimensionalized such that

$$\bar{E} = \frac{E}{E_o} = \frac{E}{\gamma_o A_o} \quad (2.19)$$

Where γ_o is the user defined characteristic surface tension. For water this would be approximately $72 \frac{ergs}{cm^2}$. From here it is trivial to dimensionalize other parameters such as force.

$$F = \frac{\partial E}{\partial z} = \left(\frac{\gamma_o A_o}{L_o} \right) \frac{\partial \bar{E}}{\partial \bar{z}} \quad (2.20)$$

$$\bar{F} = \frac{F}{\gamma_o L_o}$$

2.3.5. Example 1: 2D wire frame

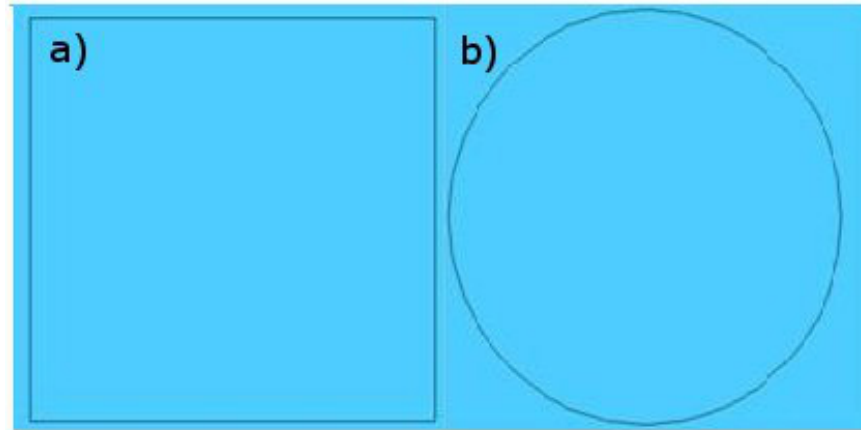


Figure 2.6: a) Starting geometry of wire frame. b) Final shape after frame converges to its energy minimum.

To help understand how SE calculates its queried values, it is useful to begin with a very simple system in which there exists an analytic solution. A logical place to start is then a 2D square wire frame with prescribed area A and surface energy T as shown in Figure 2.6 The energy of the system is going to be the tension on the wire integrated over the total length of the wire.

$$E = \oint T dr \quad (2.22)$$

$$dr = \sqrt{dx^2 + dy^2} = \sqrt{1 + \left(\frac{dy}{dx}\right)^2} dx \quad (2.23)$$

Parameterizing to polar coordinates gives the following relation,

$$\begin{aligned} x(t) &= r \cos(t) \\ y(t) &= r \sin(t) \end{aligned} \quad (2.24)$$

$$dx = -r \sin(t) \tag{2.25}$$

$$dy = r \cos(t)$$

Plugging the above two relations into equation 2.22 yields:

$$E = - \oint T \sqrt{1 + \cot^2(t)} r \sin(t) dt \tag{2.26}$$

Simplifying and applying limits of integration:

$$E = - \int_{2\pi}^0 T r dt = 2\pi r T \tag{2.27}$$

As one may have expected, the final shape is a circle. If this relationship is correct, it should be possible to graph the energy over the perimeter that SE outputs by the prescribed surface tension and retrieve a straight line with slope 1. Figure 2.7 shows this.

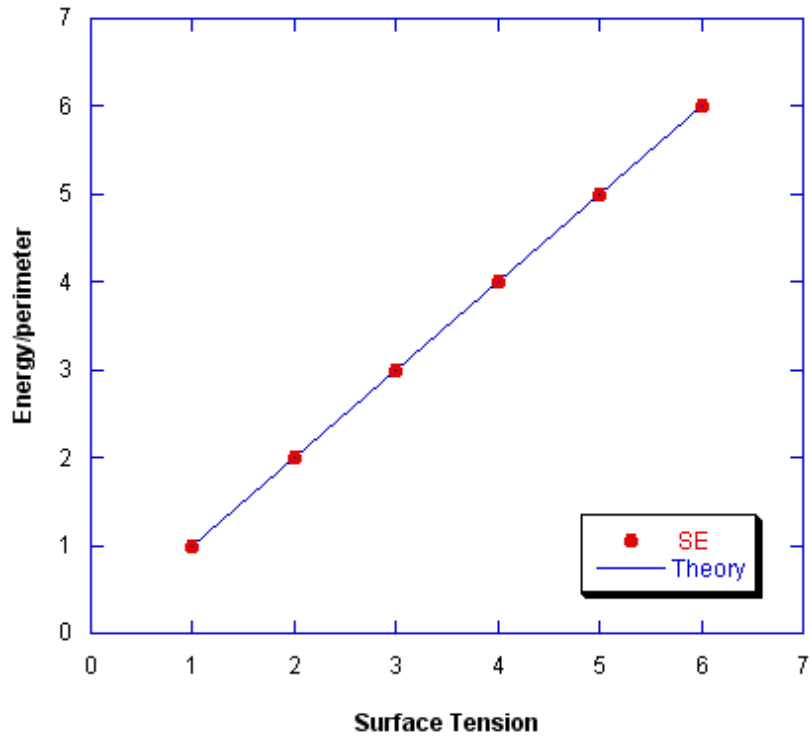


Figure 2.7: A graph of the energy/perimeter vs. surface tension (T) of the 2D wire frame. As predicted by theory, the SE points form a straight line. Error < 0.0016%

2.3.6. Example 2: cube in free space

[This section is a detailed extension of example 3.2 from the surface evolver manual⁶⁰]

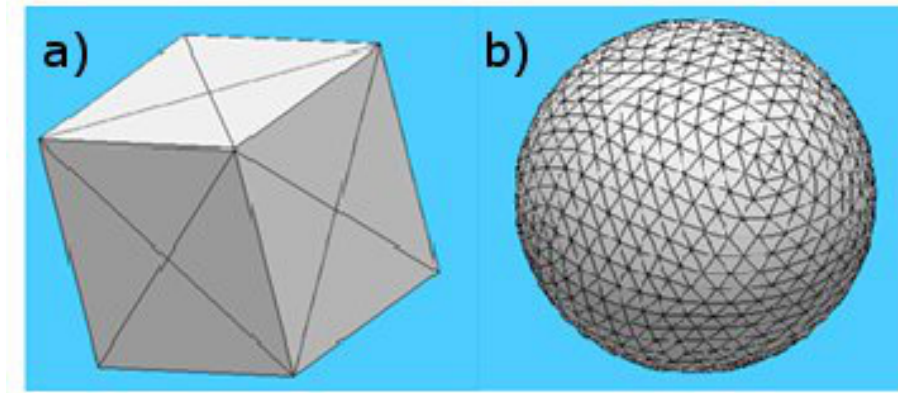


Figure 2.8: a) Starting geometry of cube in free space. b) Final shape after cube converges to its energy minimum. As predicted, it is a perfect sphere.

The next step is generalizing example 1 to three dimensions by analyzing a liquid cube in free space with prescribed volume V and surface tension T . Figure 2.8 shows the starting and evolved shapes. The process for obtaining the closed form solution to the energy integrals in this problem is pedagogically very similar to the previous example and therefore is not discussed in detail here. The only difference between the two problems is an order of dimensionality, therefore instead of the surface tension being multiplied by the circumference of a circle, it is multiplied (as one would expect) by the surface area of a sphere. This leaves us with the equation for energy:

$$E = 4\pi r^2 T \quad (2.28)$$

By normalizing the tension term to one, a simple comparison can be made between the energy and volume of the system. The result of this for both the analytic solution and the Surface Evolver output are seen in Figure 2.9.

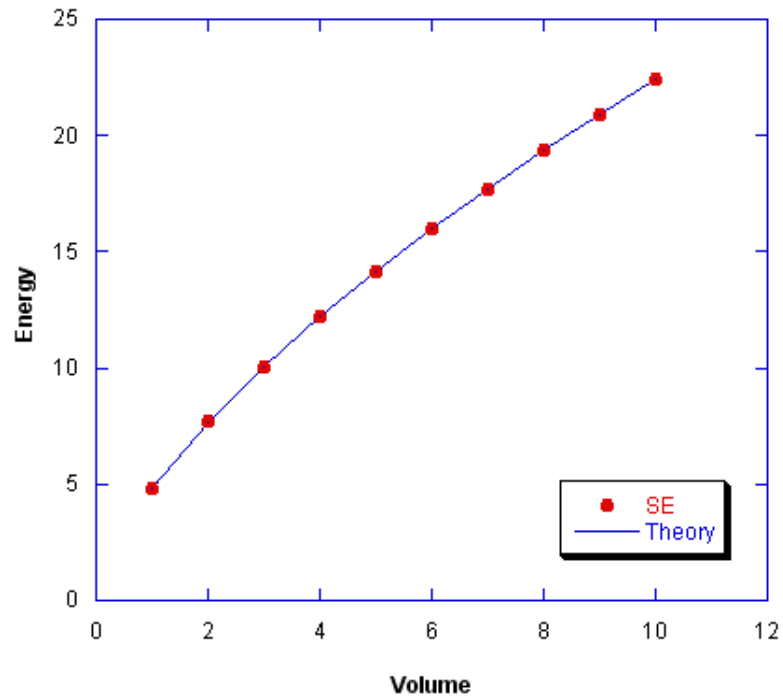


Figure 2.9: Energy vs. Volume graph of a cube in free space with surface tension term T set to one. Error < 0.001%.

2.3.7. Example 3: droplet on homogenous substrate

[This section is a detailed extension of example 3.3 from the surface evolver manual⁶⁰]

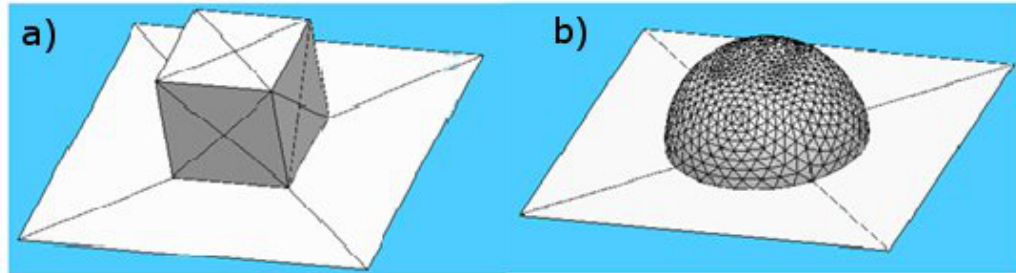


Figure 2.10: a) Starting geometry of a liquid cube on a homogeneous substrate. b) Final shape after evolution.

The final example studied here is that of a liquid drop sitting on a substrate with prescribed surface tension T without gravity. Figure 2.10 shows the initial and final evolved shape. Unlike the previous systems however, there are two components of the energy that need to be taken into account, the energy associated with the liquid/solid contact area, and the energy associated with the liquid vapor interface.

Computationally there are several ways we can address the set up of this system. The most intuitive method would be to take a cube (like in the previous example) and place it on a level set constraint that would represent the substrate. While possible, when the mesh refines there will be many vertices on the face of the cube touching the substrate that can potentially get in the way of the evolution of the system⁶⁰. Since the drops on the level set are confined to stay on the substrate, if the contact area of the drop on the substrate shrinks considerably there will be a much higher density of nodes per given area than on the liquid/vapor interface, for example. This discrepancy in mesh size coupled

with the close proximity of the nodes can lead to crashing of the software or stalling of the convergence. Therefore it is better to evoke Stokes theorem, eliminate the face of the cube touching the substrate and express the energy associated with its area as a line integral instead. This process is illustrated below.

We begin by writing the first term of the energy as the following surface integral.

$$E_L = \iint_{SL} \vec{T} \cdot d\vec{S} \quad (2.29)$$

SL is the total area of the liquid/solid contact area. If this area is laying in the xy plane then

$$\vec{T} = T_L \hat{k} \quad (2.30)$$

Is true. Using Stokes theorem the following integral can be reduced to one dimension.

$$\oint \vec{F} \cdot d\vec{r} = \iint_s (\vec{\nabla} \times \vec{F}) \cdot \hat{n} dS \quad (2.31)$$

$$\iint_s T_L \hat{k} \cdot d\vec{S} = \oint \vec{F} \cdot d\vec{r} \quad (2.32)$$

$$\begin{aligned} \vec{\nabla} \times \vec{F} &= T \hat{k} \\ \vec{F} &= -T y \hat{i} \end{aligned} \quad (2.33)$$

From basic vector calculus we can write \vec{r} as:

$$\begin{aligned}\vec{r}(t) &= x(t)\hat{i} + y(t)\hat{j} \\ d\vec{r} &= \frac{\partial x(t)}{\partial t}dt\hat{i} + \frac{\partial y(t)}{\partial t}dt\hat{j}\end{aligned}\tag{2.34}$$

simplifying our integral to the following relation

$$\oint \left(-T_L y \hat{i}\right) \cdot d\vec{r} = \oint -T_L y \frac{\partial x(t)}{\partial t} dt\tag{2.35}$$

Defining our coordinate transformation as in example 1:

$$\begin{aligned}x(t) &= r \cos(t) \\ y(t) &= r \sin(t)\end{aligned}\tag{2.36}$$

$$\int_0^{2\pi} -T_L y \frac{\partial x(t)}{\partial t} dt = \int_0^{2\pi} T_L r^2 \sin^2(t) dt\tag{2.37}$$

Solving this provides the following relation.

$$E_L = \pi r^2 T_L\tag{2.38}$$

The second component of the energy is analogous to the total surface energy of the cube in free space, with the only difference being that the final shape will be a spherical cap (dictated by the contact angle) as opposed to a whole sphere. This leaves two equations for the energy.

$$\begin{aligned}E_L &= \pi r^2 T_L \\ E_S &= A_S T_S\end{aligned}\tag{2.39}$$

T_L is the line tension associated with the triple contact line, T_S is the surface tension associated with the liquid vapor interface, and A_S is the surface area of the spherical cap. The total energy will be the addition of these two.

$$E_{tot} = E_L + E_S \quad (2.40)$$

While T_S is like the surface tension term in the cube example, T_L represents the tension associated with interplay between the liquid, vapor, and solid phases and is therefore slightly more complicated. The simplest way to express this tension is through the contact angle. From the Young-Laplace equation (section 2.1.1), we can write the force balance of a drop of liquid on a homogeneous substrate.

$$\gamma_{lv} \cos(\alpha) + \gamma_{sl} = \gamma_{sv} \quad (2.41)$$

γ represents the surface tension between either the liquid-vapor, solid-liquid or solid-vapor phases. By rearranging this equation we can see that the contact angle $\cos(\alpha)$ represents the balance between the surface tension of the three phases.

$$\cos(\alpha) = \frac{\gamma_{sv} - \gamma_{sl}}{\gamma_{lv}} \quad (2.42)$$

Therefore by defining the line tension term T_L as the contact angle, and forcing the liquid at the triple contact line to adhere to this angle, we can effectively represent the energy associated with the liquid-solid contact area. Note that there is no physical significance to forcing the liquid drop to a specific angle. Instead it is merely a convenient way to express the integral to get the correct energy. Hence this is known as a “virtual tension”⁶⁰.

By looking at the equation for line energy E_L a convenient choice of contact angle to simplify our system becomes apparent. It can be seen that if $\alpha = \pi/2$:

$$E_L = \pi r^2 T_L = \pi r^2 \cos\left(\frac{\pi}{2}\right) = 0 \quad (2.43)$$

By choosing a contact angle of ninety degrees the line integral term will not contribute to the energy. This also has the added bonus of forcing the liquid drop shape to adhere to that of a hemisphere, making the calculations of E_S much simpler as well. Now the total energy term can be expressed as:

$$E_{tot} = 2\pi r^2 T_S \quad (2.44)$$

Normalizing the surface tension term T_S to 1 for convenience, we can then compare our equation for energy to the queried SE results. This is shown in Figure 2.11.

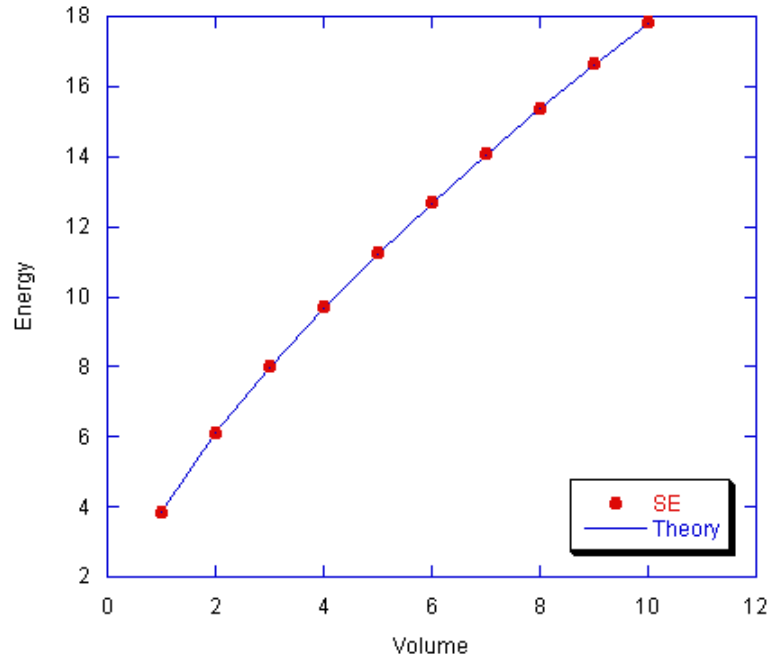


Figure 2.11: Energy vs. Volume of a liquid drop on a homogeneous substrate. Error < 0.0026%.

As can be seen, the SE output and the theoretical predictions match very well, with an average error of less than 0.0026%. An important subtlety should be mentioned. If we look at a similar graph comparing the volume to surface area of the liquid we obtain Figure 2.12. Since the surface tension T_s is normalized to one and our line integral contributes nothing, theory predicts that the energy should be equal in magnitude to the surface area of the drop. SE however seems to output an area significantly higher than the predicted value. The cause of this discrepancy is the area of the plate that the drop is sitting on. The actual physics of the system is modeled by the level set constraint defined in the code, the face of the plate itself only serves to make a more aesthetic diagram. There are two options to adjust for this. The nodes, edges and facets that define the plate

can simply be removed from the code, or we can subtract our total area by the area of the plate, which in our case is 9. By doing this the graph in Figure 2.11 is recovered.

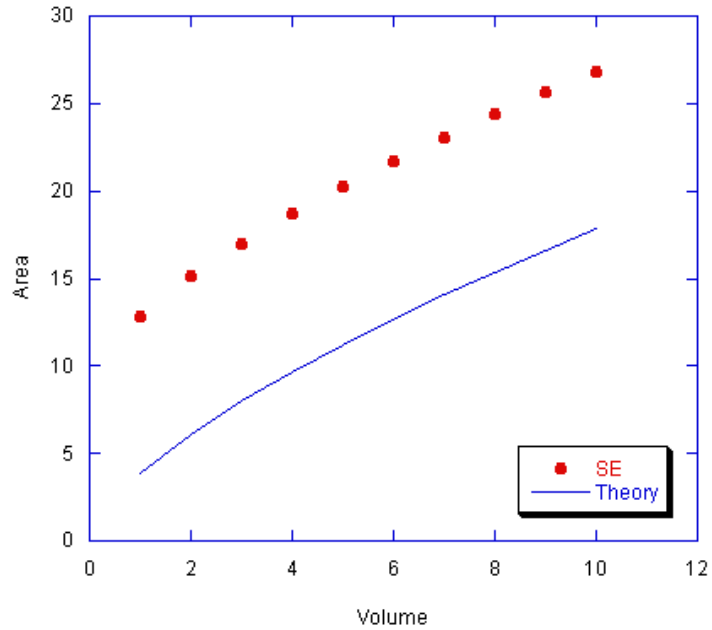
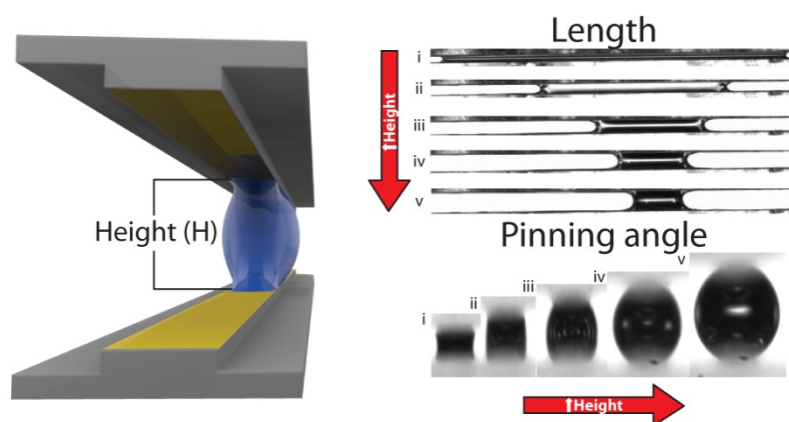


Figure 2.12: Area vs. Volume for a liquid drop on a homogeneous substrate. Since SE includes the area of all facets in its calculation, we must subtract out the area of the substrate. Note that since $T_L = 0$ the substrate does not contribute to the total energy of the system and Figure 2.11 remains correct. Had a different contact angle been chosen, this would not have been true.

From concave to convex: capillary bridges in slit pore geometry



[This chapter is reprinted (with minor modifications) with permission from: Broesch, D; Frechette, J. *Langmuir* **2012**, 28, 15548 - 15554 Copyright © 2012 American Chemical Society and D. J., Frechette, J. And Fabrication and Visualization of Capillary Bridges in Slit Pore Geometry. *J. Vis. Exp.* (83), e51143, doi:10.3791/51143 (2014).]

3.1. Introduction

Capillary bridges between solid substrates are critical to a multitude of industrial and natural processes. For example, they provide the cohesion force necessary to give structure to wet granular materials such as sand castles³⁻⁶. Additionally, liquid bridges inside the beaks of shore birds allow them to trap and consume prey⁷⁻⁹. In confined

geometry capillary condensation is responsible for unwanted adhesion in microelectromechanical systems (MEMS) and atomic force microscopy¹⁰⁻¹⁵ or the spontaneous filling of porous materials⁶¹. Capillary bridges within a reservoir create an additional pressure that needs to be overcome in the oil recovery process². The dynamics of capillary bridges is also central for inkjet and gravure printing, especially to the stability and liquid transfer rates between moving substrates⁶²⁻⁶⁶. The curvature of fluid bridges creates a Laplace pressure which, when combined with the vertical component of the surface tension force at the triple contact line, causes long range forces between the intervening substrates. This force dominates over body forces as the size of the system decreases below the capillary length ($l_c=2.2$ mm for water), and as a result has been successfully harnessed for self-assembly^{45, 55, 67-72} or controlled adhesion⁷³⁻⁷⁵.

The relationship between the capillary force and the morphology of fluid bridges has led to extensive theoretical²⁶⁻²⁹, experimental^{30, 32-35, 76}, and modeling³⁶⁻³⁸ investigations aimed at predicting the profile and forces of axisymmetric bridges formed across flat surfaces, spheres, or cylinders. These efforts also focused on the case where the capillary bridges are bounded by two physically and chemically uniform surfaces (no contact line pinning). The high levels of symmetry in these fluid bridges led to elegant analytical solutions for both the surface profile of the bridges and the capillary forces²⁷⁻²⁹.

With the advent of patterning and lithography, surfaces can be created with heterogeneous physical or chemical boundaries that pin the triple contact line of fluids. Pinning of the triple contact line on a surface alters the shape of a capillary bridge and allows for the design of surface patterns that lead to pre-determined capillary forces⁷⁷⁻⁸⁰ or bridge morphology⁸¹⁻⁸⁴. While the number and complexity of surface patterns that can

bound capillary bridges is virtually unlimited, even simple cases that rely on high levels of symmetry have shown promise in micro & nanoscale systems. For example, chemical patterns have been utilized to direct liquid flow between substrates without the need of a traditional four wall enclosure¹⁶⁻¹⁸ and the “flip-chip” assemblies rely on the capillary forces between chemically or physically patterned surfaces for alignment of microelectronic components^{45, 85-90}.

One of the simplest ways to break symmetry is to form a capillary bridge in slit pore geometry (Figure 3.1).⁹¹⁻⁹⁵ In this configuration a capillary bridge with a high aspect ratio (length/width) is formed across two long narrow strips. The triple contact line is pinned on the length of the bridge but is free to advance or recede along the strip. Previous theoretical and computational efforts aimed at predicting the morphology and associated capillary forces caused by liquid bridges in slit pore geometry have yielded drastically different morphology based on the different constraints and approximations employed. Anvil shape bridges are observed when the fluid bridge is treated as a fully 3D system on a perfectly wettable strip⁹², a feature not observed when the bridge is treated as a 2D system⁹¹.

Here we report the results of experiments and numerical simulations aimed at characterizing the morphology of capillary bridges in slit pore geometry (Figure 3.1). We investigate how the strip width, fluid volume, and pore height influence the morphology of the capillary bridges. At constant volume, we observe the counterintuitive result where the Laplace pressure goes from negative to positive as the height of the capillary bridge is increased. Using scaling that collapses our data into universal curves, we show that this transition in the sign of the Laplace pressure is universal for capillary bridges with high

aspect ratios. We also find that even if the Laplace pressure is increasingly positive as the height of the bridge is increased, the total capillary force is dominated by the surface tension component and remains attractive at all separations. Finally, we highlight the importance of the wetting angle along the strip in the determination of the bridge morphology, more specifically in predicting whether or not “anvil” bridges will be formed.

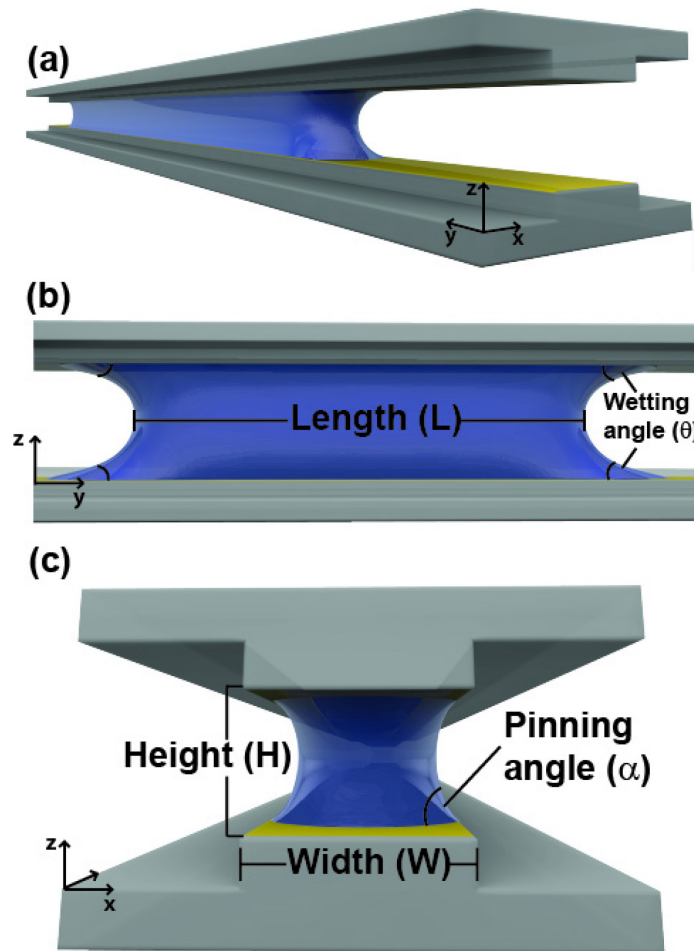


Figure 3.1: Experimental parameters for the characterization of capillary bridges in slit pore geometry. (a) Three quarters view, (b) Side view and (c) Front view. Images were rendered in Cinema 4D using data from Surface Evolver simulations.

3.2. Materials and Methods

3.2.1. Fabrication of the substrates

The capillary bridges were formed between two opposing faces of hydrophobic rectangular pillars (see Figure 3.1). The pinning of the capillary bridges on the length of the strip was achieved by rendering hydrophilic the opposing faces, therefore creating both a chemical and physical heterogeneity for the contact line. The pillars were made by casting PDMS (polydimethylsulfoxide, Sylgard 184) into a mold made from SU-8 2050 (MicroChem). The SU-8 mold was fabricated using standard photolithographic techniques⁹⁶. The pillars had a height of 100 μm , a length of 40 mm, and the width was varied between 250-500 μm . In all the experiments described in this work the length of the pillar was much longer than the length of the capillary bridges. The top faces of the pillars were made hydrophilic by first adding a gold layer and then functionalizing the gold layer with a hydrophilic thiol monolayer following a similar protocol as in Childs et al.⁹⁷. Briefly, a 20 nm gold layer using microcontact printing was deposited on the PDMS pillar. Bonding between the gold film and the PDMS pillar was ensured by using the MPTS (mercaptopropyltrimethoxysilane, Gelest) coupling agent that was deposited on the gold via spin casting from a 2mM MPTS/toluene solution. Prior to stamping, the gold surface was rinsed with DI water and placed in a 10mM HCL solution for 5min to hydrolyze the MPTS and the PDMS pillars were exposed to oxygen plasma. Once the transfer of the gold film on the pillars was completed, the gold was functionalized with a hydrophilic MHA monolayer (mercaptohexadecanoic acid, 90% Sigma-Aldrich) using a 1mM solution in dimethyl sulfoxide for 24 hours. After rinsing, the advancing contact

angle on the gold surface is $10\pm 2^\circ$ and the receding angle is 0° indicative of an ordered monolayer of MHA⁵⁷⁻⁵⁸. The rest of the pillar has a contact angle of $111\pm 2^\circ$. DMSO was chosen over other solvents like ethanol due to its low PDMS swelling factor⁹⁸.

3.2.2. Experimental device

The experimental device can be broken up into four main parts: 1) the top substrate stage, 2) the bottom substrate stage, 3) the syringe/ syringe xyz-translation stage and 4) the camera/optics and camera holder. The details of each follow:

- 1) **Top substrate stage.** A digital translation stage is attached to a P-series mounting clamp via a custom machined connector piece. The mounting clamp is connected to a variable height P-post which is anchored to a bread board via a P-series clamping fork. A custom connection piece attaches to a custom machined glass slide holder to the translation stage, providing $1\ \mu\text{m}$ displacement resolution in the z-direction.
- 2) **Bottom substrate stage.** A xy linear translation with z-axis rotation stage is attached to the bread board via 8 post extension pieces. A custom machined substrate holder is attached to the top of the xy linear translation with z-axis rotation stage, allowing the bottom substrate to be positioned with $10\ \mu\text{m}$ translational resolution and rotated with 1 degree resolution.
- 3) **Syringe/syringe xyz translation stage.** For xyz positioning of the syringe used to fill the gap between the pillars, a 5uL syringe with a 30 gauge needle is attached to a xy

translation stage. The xy stage is then attached to a z translation stage via a 90° connector piece.

- 4) **Camera/ optics and camera holder.** For imaging of the liquid bridges, a CCD camera is attached to a variable zoom optics piece. At maximum zoom, this gives a resolution of 3.3 $\mu\text{m}/\text{pixel}$. The camera is attached to a laboratory scissor jack, which can be positioned to image the liquid bridge from different angles.

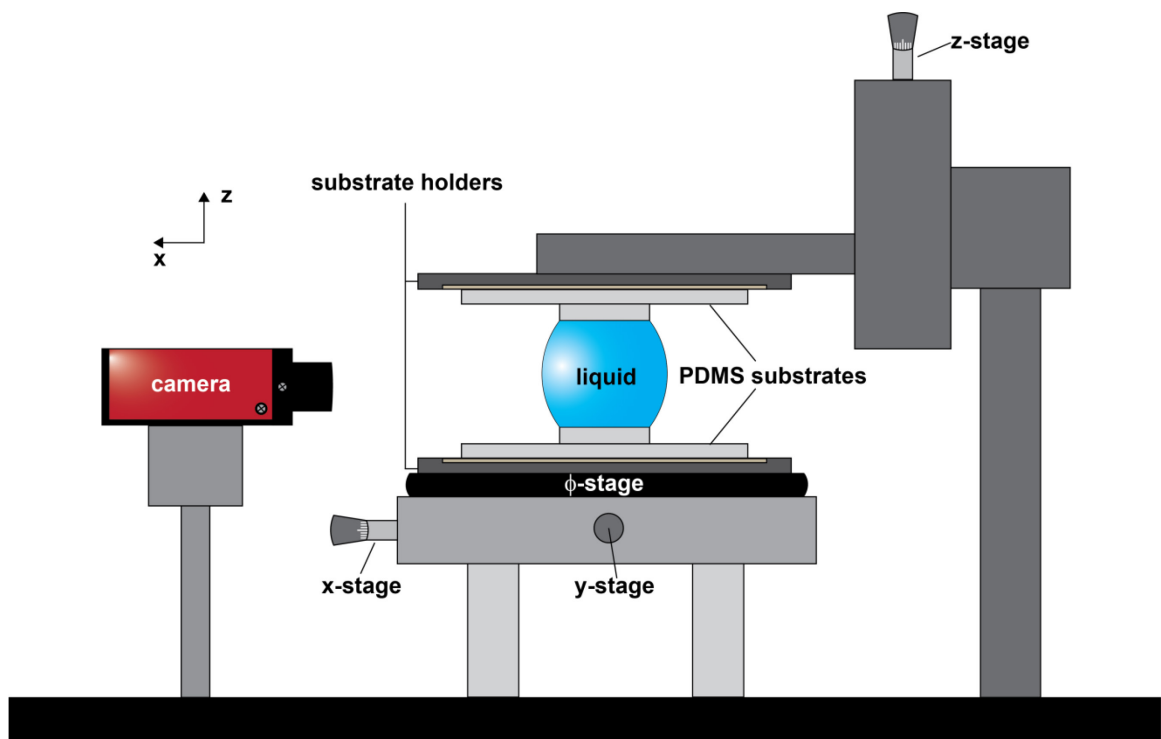


Figure 3.2: Schematic of experimental device. x, y, z, and ϕ stages allow for four special degrees of freedom.

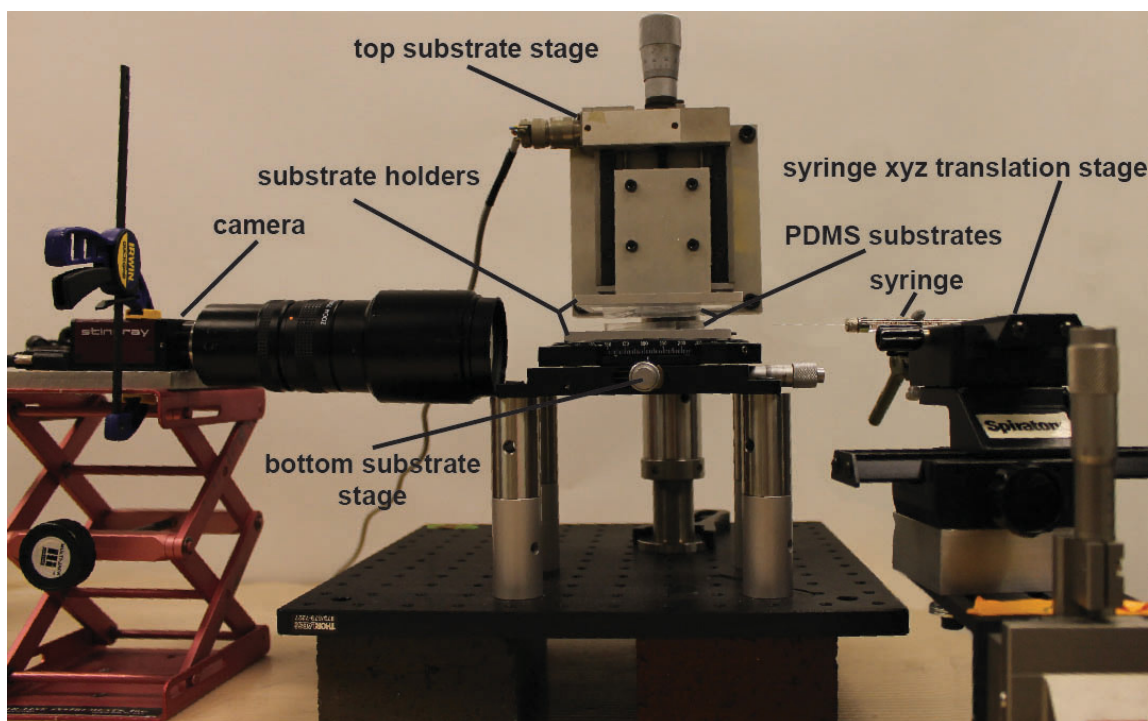


Figure 3.3: Picture of complete experimental set up. The PDMS substrates are held at a variable distance apart through a combination of x,y,z and rotation stages. A separate set of microstages (far right) holds the syringe to introduce the liquid into a narrow gap to create the capillary bridge in a slit-pore geometry. A CCD camera (pictured left) is used to image the resulting capillary bridges as the pore separation is changed. The resulting images can then be analyzed in the open source image analysis software ImageJ.

3.2.3. Formation and characterization of the capillary bridges

The rectangular pillars were aligned so that their long axis were on top and parallel to each other using the experimental device described above. Efforts were made

to measure and reduce the tilt angle between the two pillars to less than 0.1° . The separation between the opposing surfaces of the pillars was measured using a digital micrometer and zero separation was defined as when the two pillars first make contact. After the alignment, the capillary bridge was created by injecting a mixture of glycerol and water (approximately 4:1, to reduce evaporation) between the opposing pillars when they were separated by about $200\ \mu\text{m}$ using a micro-syringe (Hamilton 5uL PN#87930). The separation between the pillars was sometimes increased as liquid was added to ensure that the capillary bridge did not reach the end of the hydrophilic strips. Once the desired volume was attained, the syringe was removed and the height of the capillary bridges (H) was varied in $50\ \mu\text{m}$ increments by moving the upper pillar and images of the bridge length (L) or pinning angle (α) were taken at each step (see Figure 3.1). Once the final height was reached (usually between 0.75-1.5 mm) the height of the capillary bridge was decreased and the length and pinning angle measured again to check for hysteresis. After each increment, we waited for 1-2 min to ensure that equilibrium morphology had been reached. In general, the maximum bridge height ($\sim 1.5\ \text{mm}$) was lower than the capillary length of the fluid ($l_c = 2.2\ \text{mm}$) to minimize the role played by gravity. All the data sets presented in this work have been repeated at least 3 times and the error bar corresponds to the standard deviation of the average between data sets. Images were analyzed using the open source software package ImageJ.

3.2.4. Surface Evolver simulations

The finite element package Surface Evolver⁵⁹ was employed to model our experimental system. This software uses the gradient descent method to minimize the free energy of the system. Convergence was defined as a change of less than 10^{-7} energy units after at least 4 iterations. To reduce computational time we exploit the planes of symmetry along the length and width, the plane of symmetry along the height was not used due to instability modes that can alter bridge break up in that direction⁹². Therefore, we generally modeled a quarter of the total bridge system, of which constituted on average roughly 2500 individual nodes. In the simulations, the wetting angle of the hydrophilic strip was set to 15° to represent our experimental data and to ensure that the bridge length remained independent of the strip length. To normalize the force (Figure 3.11b) we used the measured value for the water-glycerol surface tension (51 dynes/cm). Since the range of experimental pore separations (H) took place below the capillary length of our liquid, gravity was not included in our simulations.

3.3. Results and Discussion

3.3.1. Bridge morphology and scaling

The shapes of the capillary bridges were characterized by measuring the pinning angle (α) and the overall dimensions of the bridges, which we defined by the midway length (L), height (H), and width (W) (see Figure 3.1). Shown in Figure 3.4a are representative curves of the measured aspect ratios (L/W) of the bridges as the surfaces

are pulled apart at constant volume. Also seen in Figure 3.4a is the wide range of bridge aspect ratios ($1 < L/W < 120$) covered in this work. As expected, we observe that an increase in volume for a given width leads to longer bridges, and that at a given volume a wider confining strip leads to shorter bridges. The good agreement observed for the whole parameter space explored in this work between our experimental results and simulations using the Surface Evolver package is also shown in Figure 3.4a. The curves in Figure 3.4 were obtained by increasing the bridge height, but the same morphology is observed when the height is decreased. A small amount of hysteresis, however, is present, see in Figure 3.5 for two consecutive cycles. As the height of the bridges gets close to the capillary length ($l_c = \sqrt{\frac{\gamma}{\rho g}} = 2.3 \text{ mm}$), the effect of gravity starts to deform the bridges, therefore we do not take measurements much past this limit.

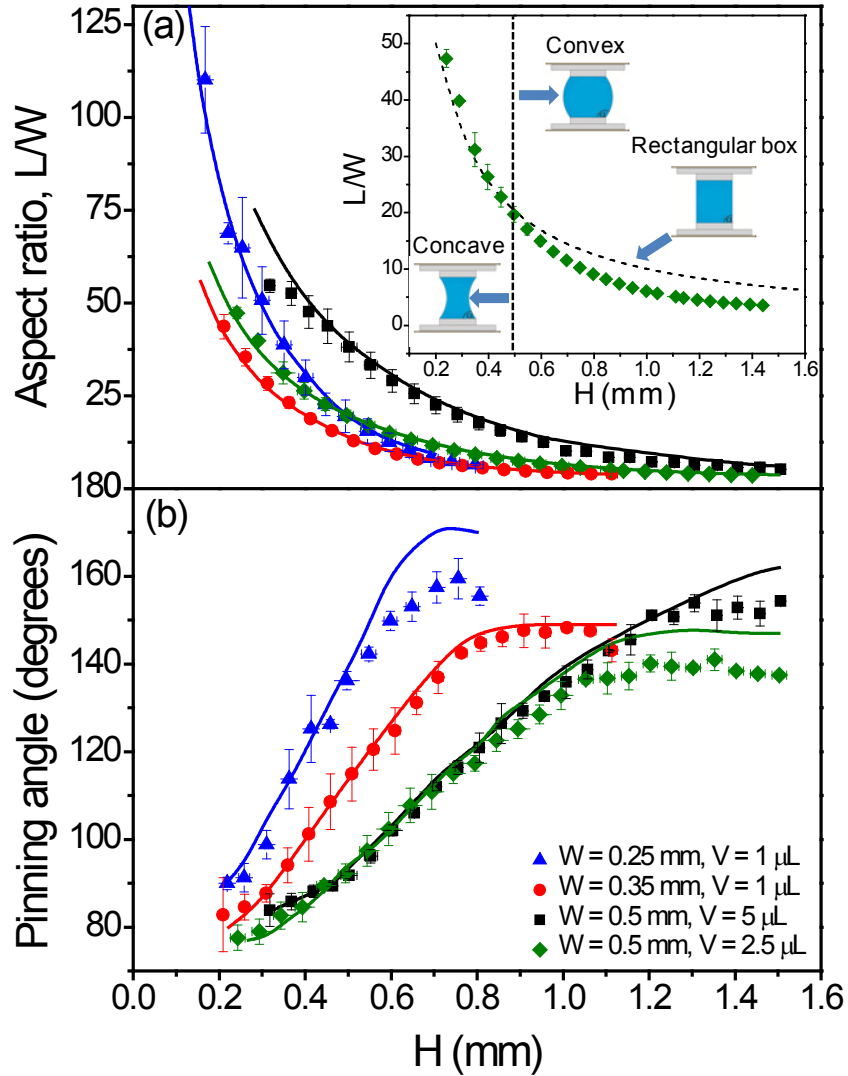


Figure 3.4: (a) Aspect ratio (L/W), and (b) pinning angle (α) as a function of the bridge height (H) taken for different volumes and strip widths. The data points are from experimental measurements and the solid lines are the results of the Surface Evolver simulations. The dashed line in the inset corresponds to the aspect ratio of a rectangular box (i.e. $\alpha = 90^\circ$), when the experimental data is above the dashed line the pinning angle must be less than 90° and when it is below the dashed line the pinning angle must be greater than 90° , as illustrated by the schematic.

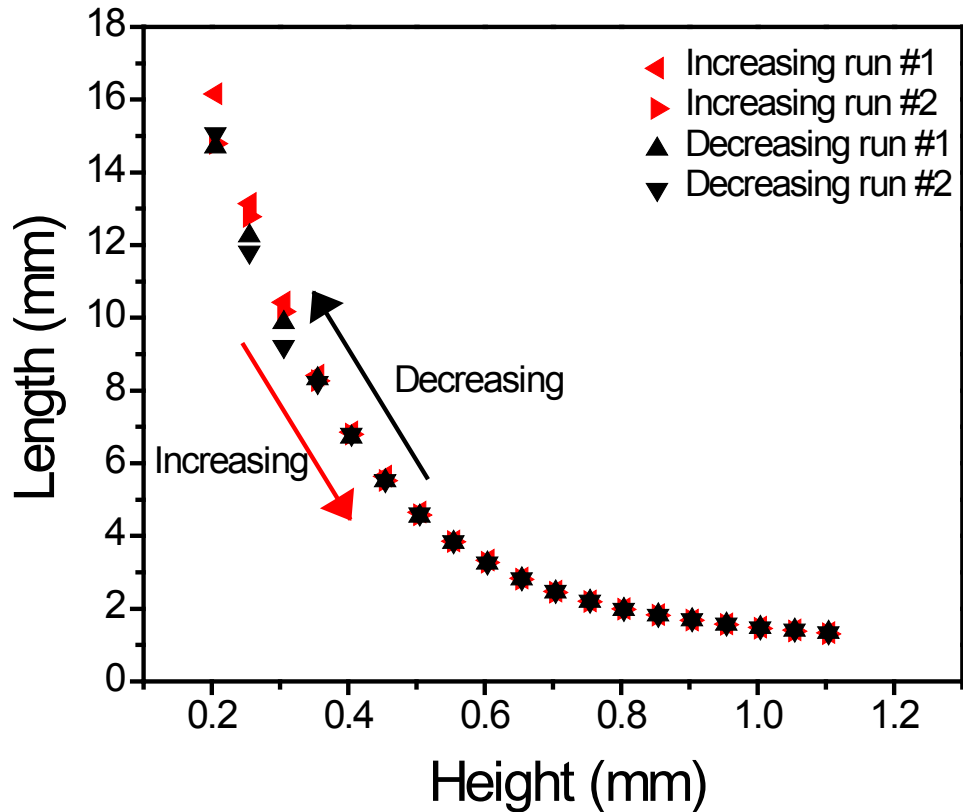


Figure 3.5: Hysteresis in the measurement of the length for a capillary bridge with width = 0.35 mm and volume = 1 μ L. The liquid was induced between the substrates at 0.2 mm, then the separation was increased to 1.1 mm, and decreased back down to 0.2 mm.

While the relationship between L and H appears to be inversely proportional, a closer look shows that it is not the case (Figure 3.4a inset). Indeed, a $L \propto H^{-1}$ relationship would imply that the pinning angle stays constant at 90° as the surfaces are pulled apart. As seen from the inset, our experimental data is initially larger than $1/H$ until $H=0.5$ mm, and then crosses the $1/H$ curve to reach lower values. The presence of this crossover implies that the pinning angle not only changes as the surfaces are pulled

apart, but *increases* and transitions from an initial value that is less than 90 degrees to a final one that is significantly larger than 90 degrees (see schematic inside Figure 3.4a). This counterintuitive increase in the pinning angle as the supporting plates are pulled apart is observed experimentally: the pinning angle is usually less than 90 degrees at low height and reaches values that can be as large as 160 degrees as the height is increased (Figure 3.4b). This increase in pinning angle implies that the curvature of the capillary bridges along their lengths goes from concave to convex as the surfaces are pulled apart, a feature that we observe experimentally and with the surface evolver simulations (Figure 3.6). The measured values for the pinning angle are also in quantitative agreement with Surface Evolver simulations at low H , but as the height is increased, we see that the simulation results overestimate the measured value (Figure 3.4b). We suspect that the deviation observed at high H is caused by limitations in imaging; mainly it is challenging to focus on the bridges as they recede towards the middle of the strip. As a bridge recedes, the images have a baseline that is shifted upwards (due to the distance between the end of the strip and the liquid bridge being near the maximum depth of field of the optics), which leads to a systematic error such that the images taken underestimate the real pinning angle values. Additionally, we note that we achieve very good agreement between simulations and experiments for measurements where focusing is not a problem (such as for the length for example), which is consistent with the discrepancy in pinning angle being an artifact of our imaging technique. Finally, a small effective tilt of 0.1 degrees between the two supporting plates is not uncommon and is incorporated in the analysis and surface evolver simulation. We found that the surface evolver values underestimated the measured pinning angle if the tilt was not taken into account. Tilt

leads to a change in the height between the plates and the pinning angle depends on the height (see Figure 3.4b). Note in these simulations, symmetry along the length is broken, and therefore half of the bridge was modeled as opposed to one quarter.

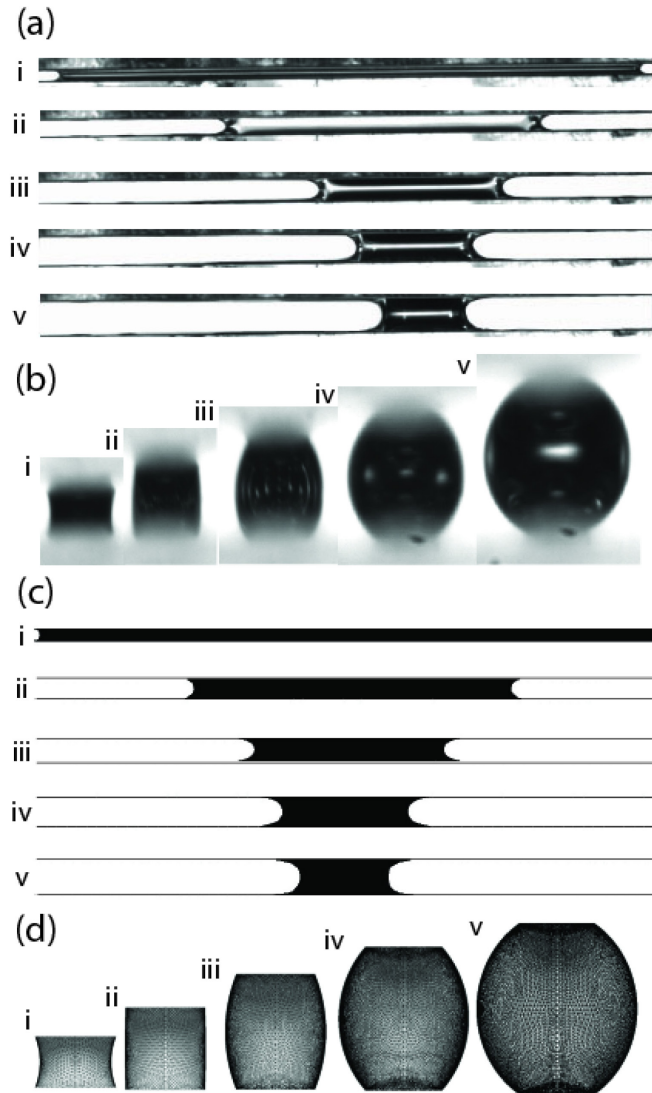


Figure 3.6: Experimental (a, b) and simulated (c, d) images of liquid bridges with volume = 2.5 μL , strip width = 0.5 mm and height i) 0.3, ii) 0.5, iii) 0.7, iv) 0.9 and v) 1.1 mm. The side view showing the bridge length is shown in (a) and (c) and the front view showing the pinning angle is shown in (b) and (d).

We observe that all the curves describing the change in length (or aspect ratio) with height collapse into a single curve when the length is scaled by an effective length V/W^2 , where V is the volume of the liquid, and the height is scaled by the width, H/W , as shown in Figure 3.7a. A similar collapse is also observed when the length is scaled by HW/V in Figure 3.8. We also find that the pinning angle at a given H/W is independent of the volume of the bridge (Figure 3.7b). The fluid volume does not influence the pinning angle because adding liquid on a long strip causes the bridge to increase its length while keeping its curvature constant (unless the bridge reaches the end of the strip), a feature also observed by Valencia et al.⁹². The pinning angle, however, depends on volume at $H/W > 2$. At these large H/W , the aspect ratio of the bridges is less than 20 and the bridge cannot be considered translationally invariant (i.e. the cross section in the z-x plane changes along the length of the bridge) and a unique pinning angle does not effectively describe the whole bridge (see Figure 3.9 for values of the pinning angle along the bridge length). The fact that features of the bridge such as the length and the pinning angle scale with the width of the strip and the fluid volume suggests that our observations obtained here with macroscopic (mm) bridges would be similar for bridges in slit pore geometry at the microscale. For nanoscale bridges, however, we would expect other effects that have been neglected here, such as line tension, to also play a role.

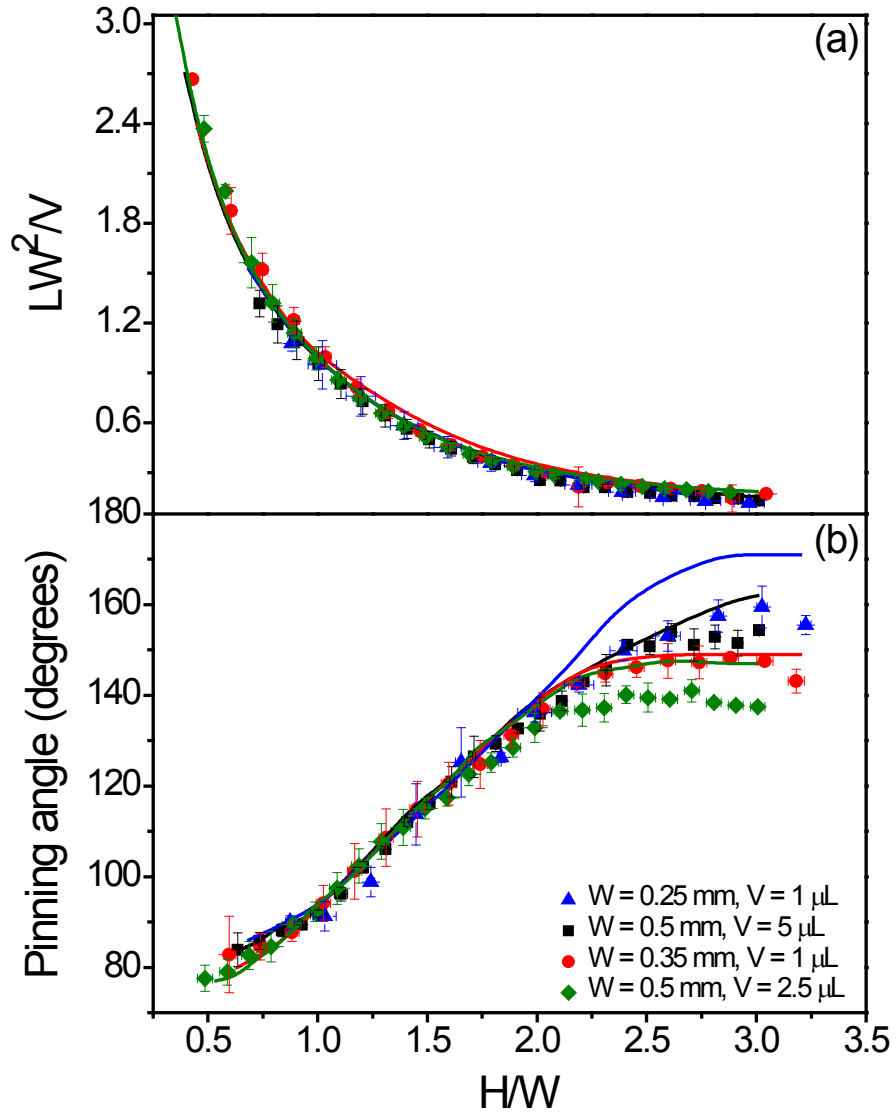


Figure 3.7: Scaling of the length (a) and of the pinning angle (b) as the height of the capillary bridge is increased. The data points correspond to experimental results and the solid lines correspond to the Surface Evolver simulations.

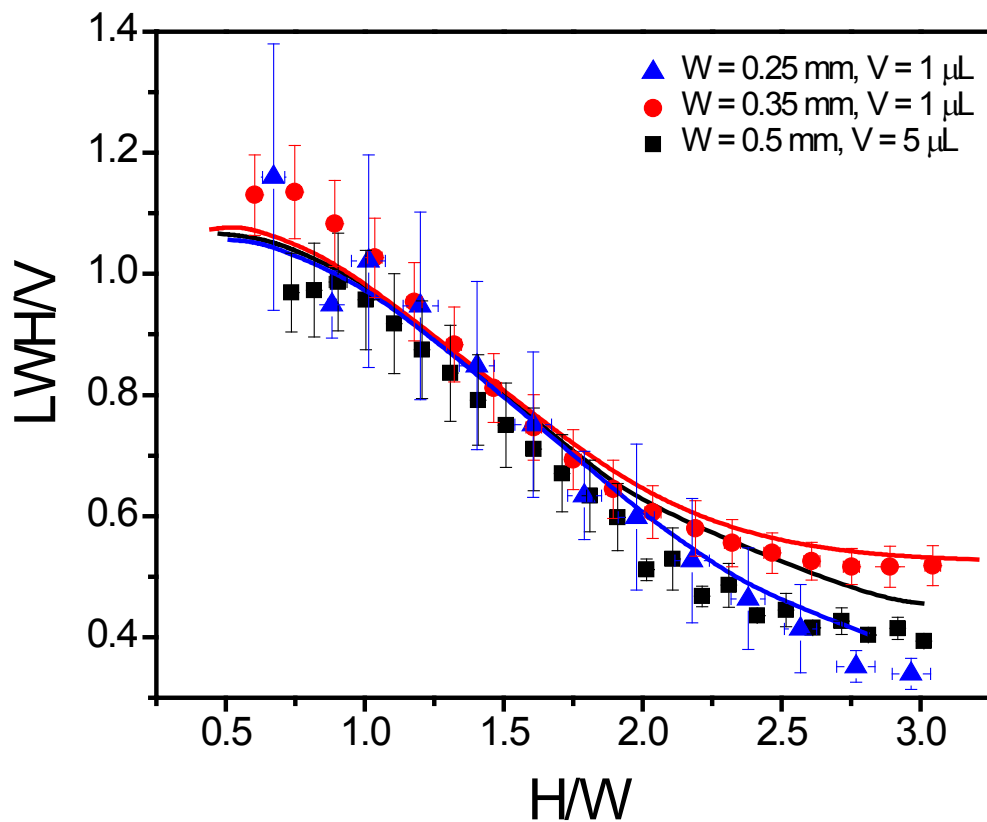


Figure 3.8: Volume of liquid bridges normalized by the “box” ($\alpha = 90^\circ$) volume vs. H/W . The data collapses when the pinning angle is near 90° , and deviates as α increases or decreases from this value.

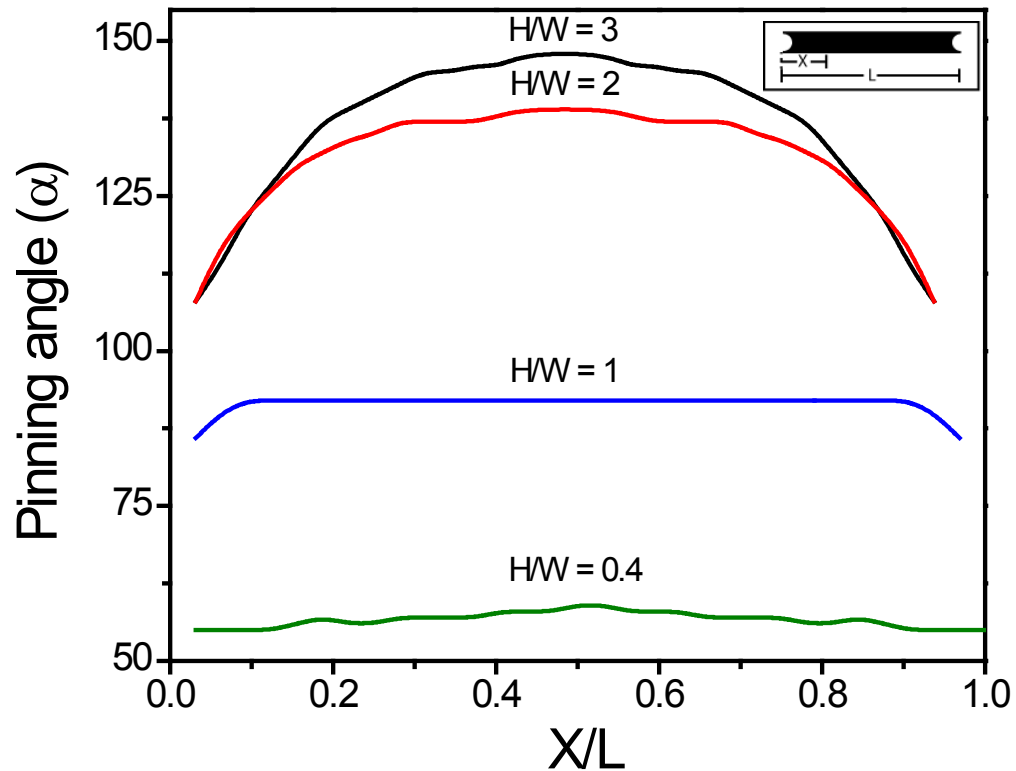


Figure 3.9: Simulated data for pinning angle (α) at various positions (X) along the length of liquid bridge (width = 0.35 mm, volume = $1\mu\text{L}$.)

Bridge break up was observed to occur at H/W values significantly larger than the ones shown in Figure 3.4 and we observed that a lower reduced volumes (V/W^3) leads to break up at lower H/W . Figure 3.10 shows the simulated mean curvature and pinning angles for different reduced volumes V/W^3 spanning two orders of magnitude. It can be seen that even over such a large range of volumes, all of the trials collapse onto a single universal curve. As V/W^3 decreases however, the reduced separation H/W where the data departs from the universal behavior also decreases. This departure occurs when the liquid

bridge is no longer highly asymmetric ($L/W \gg 1$) and thus, the bridges behave similarly to the axisymmetric case in this regime. As expected, the pinning angle reaches a maximum and then starts to decrease before eventually rupturing into two separate drops (Figure 3.10b). Bridge break up occurs at around $H/W = 1.1$ for the $V/W^3 = 0.65$ case, and around $H/W = 1.6$ for the $V/W^3 = 2$ case. Higher V/W^3 bridge broke at $H/W > 6$ (data not shown).

For the experiments shown here, the height at break up was always larger than the capillary length, and therefore gravity caused the liquid bridge to become asymmetric along its height and bulged near the bottom surface. Therefore, after rupture, significantly more liquid was left on the lower pillar than on the upper one. In general bridge rupture did not cause the liquid to break off of the pillars and spill onto the hydrophobic PDMS.

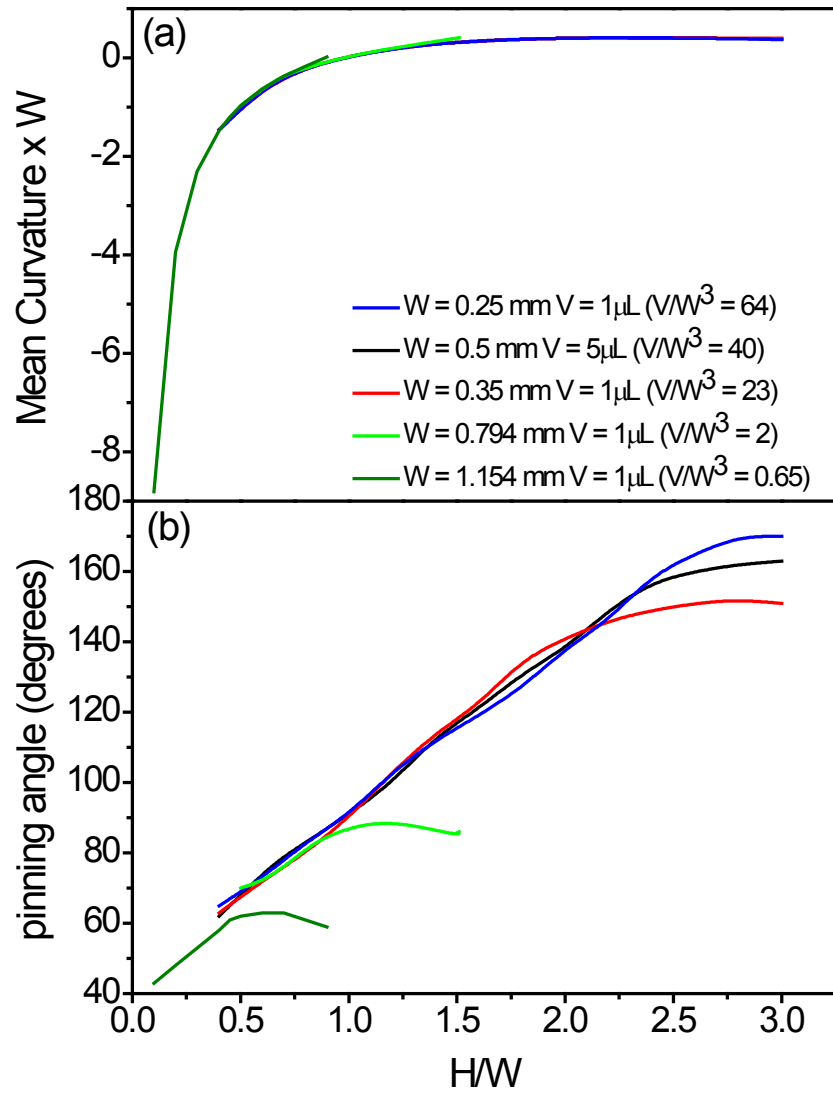


Figure 3.10: (a) Mean curvature normalized by width and (b) pinning angle vs. H/W for a large range of V/W^3 . Bridges with lower reduced volumes deviate from universal behavior at lower H/W .

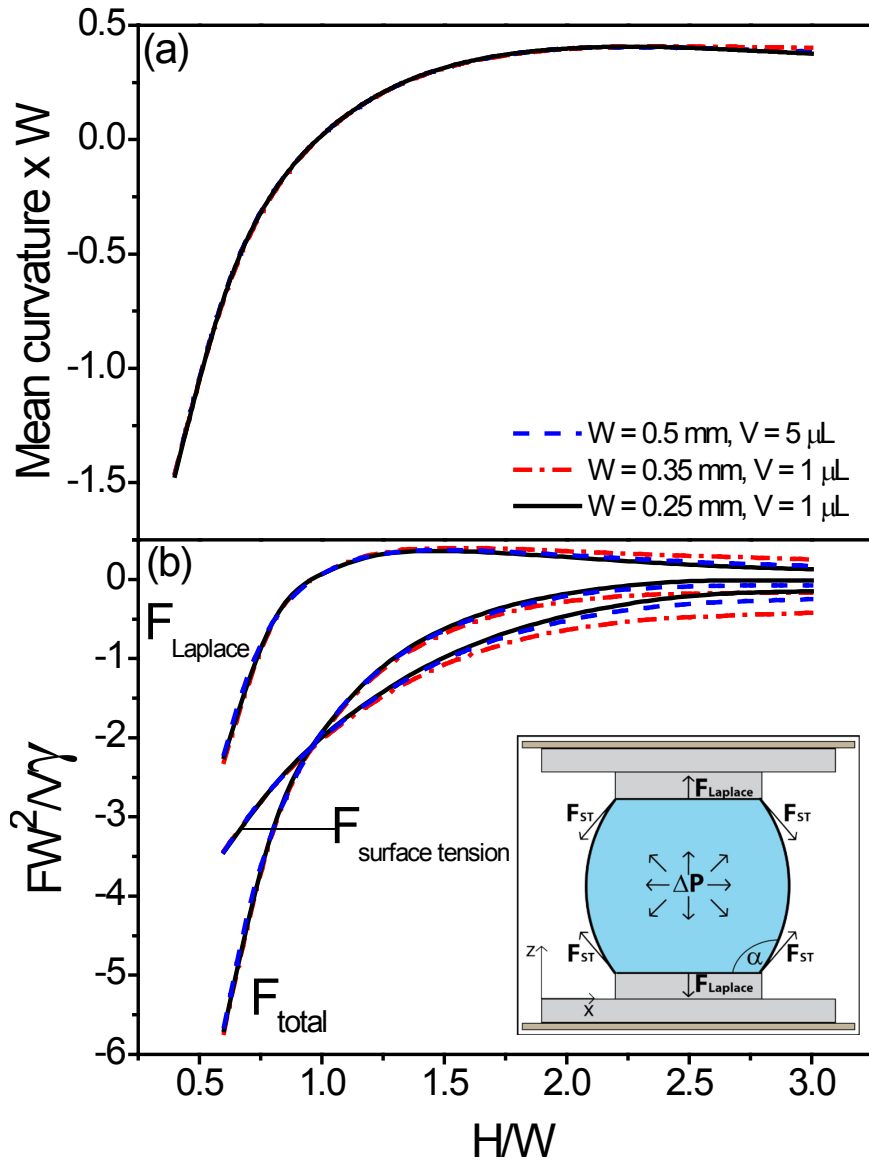


Figure 3.11: (a) Change in mean curvature (scaled by the width) as the bridge height is increased. A sign change from negative to positive occurs at around $H/W = 1.0$. (b) Normalized total force and normalized Laplace and surface tension components of the capillary force between the substrates. The curves are obtained from Surface Evolver simulations. The inset shows the projections of the surface tension (F_{ST}) and Laplace (F_{Laplace}) force components.

3.3.2. Curvature and capillary force

Figure 3.11a shows the calculated mean curvature normalized by the width as a function of H/W . Here we can see a transition from negative to positive values at around $H/W = 1$ (for the strip wetting angle $\theta = 15^\circ$). The mean curvature of the liquid bridges changes from concave (negative) to convex (positive) as the bridge height is increased at constant volume. This corresponds directly to the transition in the pinning angle from less than 90° to greater than 90° observed in Figure 3.4b. In addition, when the normalized mean curvature is plotted against H/W , we see that it is independent of volume for all the volumes investigated here, which is in agreement with the simulations of Valencia et al.⁹² who investigated bridge morphology in a similar configuration. Princen⁹⁹ investigated the case of capillary bridges between two cylinders both experimentally and analytically. He reports that for sufficiently long bridge lengths the mean curvature is independent of volume, similar to what we see in Figure 3.11a. Transitions from negative to positive mean curvature have also been observed for axisymmetric bridges when the volume is increased and the triple contact line is pinned in all directions⁸¹, here the change in the sign of the mean curvature occurs at constant volume.

Swain and Lipowski⁹¹ developed an elegant theory to predict the morphology of capillary bridges in slit pore geometry in which they considered the bridges as a translationally invariant 2D system. The theory predicted morphological transitions where the pinning angle (α) would decrease as the bridge height is increased (the opposite of what we observe here). The discrepancy between their results and ours is not due to the constraint of translational invariance imposed by Swain and Lipowski: we observe the change in sign in mean curvature at large aspect ratios where the capillary

bridge is essentially translationally invariant. Instead, we suspect the predictions of a decrease in the pinning angle as the height is increased stems from their effective 2D geometry preventing the movement of the triple contact line along the length of the bridge. Using molecular dynamic simulations, Yaneva et al. reports a decrease in pinning angle as the height of a capillary bridge in slit pore geometry is increased⁹⁴ (opposite to what we see). There are, however, significant differences between our work and that of Yaneva and coworkers. First, they work at a much larger wetting angle ($\theta \approx 73^\circ$) and with lower reduced volume ($V/W^3 = 0.65$) at heights closer to the break up point. Surface Evolver simulations ran under these conditions also showed a decrease in the pinning angle as the height is increased for $H/W = 0.5$ to 0.95 . For $0.3 < H/W < 0.5$ we see an increase in the pinning angle not shown in their work, which could be due to factors unique to the nanoscale.

Valencia et al.⁹² simulated capillary bridges in slit pore geometry of finite length and with a strip wetting angle $\theta = 0^\circ$. The liquid morphologies they obtained are quite different than the ones described in our work. They observe the appearance of long thin sleeves that extend from the center of the bridge all the way to the end of the confining strip, creating capillary bridges that have an “anvil-like” shape. These sleeves are present in their system whenever the mean curvature is greater than zero. The presence of these tails leads to bridge lengths (and overall morphology) that depend on the length of the slit pore itself. In our work we found that the appearance of these long tails depends strongly on the wetting angle of the strip. For instance, using a wetting angle of 15° in the simulations is sufficient to prevent the appearance of these tails and leads to bridge lengths that are independent of the strip length. It is interesting that a small difference in

the wetting angle (from 0° to 15°) is sufficient to create such a difference in the final morphology of the capillary bridges.

The capillary force associated with the Laplace pressure reaches a maximum at around $H/W = 1.4$ (Figure 3.11b). The total force between the plates caused by the capillary bridge can also be calculated using Surface Evolver by differentiating the total energy obtained from the simulations as the height of the bridge is increased (Figure 3.11b). Interestingly, we see that while the Laplace force component crosses from attractive to repulsive as the height is increased, the total force is always attractive, and monotonically increases towards zero. Qualitatively, this trend in total force is similar to what is expected for an axisymmetric bridge between two homogenous plates when the triple contact line is not pinned. The surface tension component is responsible for keeping the total force attractive as it is always attractive and dominates (in magnitude) over the Laplace pressure component as the height is increased. We also find that the force data collapses onto a single curve for most values of H/W when the force is normalized by the surface tension (γ) and the characteristic length V/W^2 . As the separation increases, however, the force curves begin to depart from one another. We believe this is due to the increasing contribution of the end caps of the bridge that become more relevant at lower aspect ratios. These end caps likely do not scale.

For constant strip width (W) and volume (V), an increase in the wetting angle shifts the normalized mean curvature to higher values. The qualitative trend of changing sign from negative to positive as H/W increases is still observed with larger wetting angle (see Figure 3.12). Note that the total force between the substrates remains attractive for the entire range of wetting angles and heights probed (data not shown).

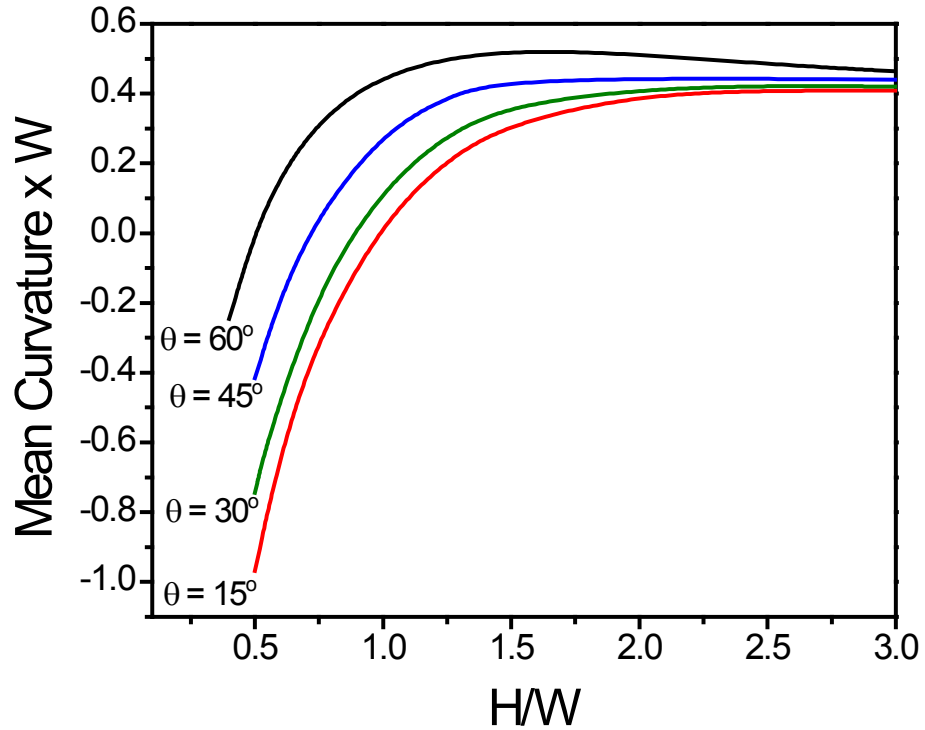


Figure 3.12: Simulated data for Volume = $2.5\mu\text{L}$, width = 0.5 mm. The normalized height at which the sign change in curvature occurs decreases as the wetting angle increases.

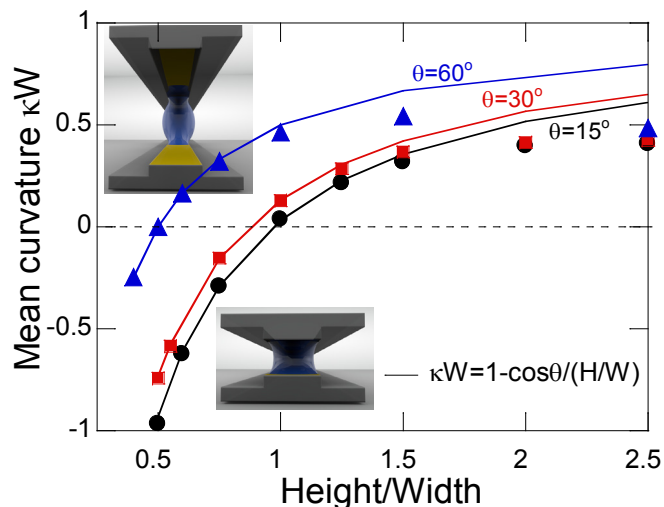
3.4. Conclusion

We performed experiments and numerical simulations to characterize the morphology of liquid bridges confined within a slit pore of variable height. We showed that as the pore height is increased, the aspect ratio of the bridge (length/width) decreases while the pinning angle increases. The increase in the pinning angle observed was significant, ranging from 70° to 160° for the values of H/W probed here. The increase in

pinning angle was found to be associated with a transition in mean curvature from concave (negative) to convex (positive) as the bridge height was increased at constant volume. The transition from concave to convex occurred when H/W was around 1. Interestingly, the presence of a finite wetting angle (15° as opposed to 0°) greatly changes the morphology of the liquid bridges, preventing “anvil-like” bridges observed in previous work⁹² with sleeves that extend to the ends of the strip.

Additionally, we demonstrated that scaling the bridge length by an effective length V/W^2 and the height by the width led to a collapse of the morphological characteristics of the bridge into universal curves. The observed scaling suggests that the morphological transitions observed here with millimeter bridges would also be observed at the microscale. Finally, the total force between the plates was found to be always attractive, and collapsed onto a universal curve for a large range of H/W . Although the Laplace component of the force was repulsive for larger separations, the surface tension component is always attractive and dominates in this regime such that the total force is always attractive. While these conclusions apply to static bridges, it would be interesting to investigate the role played by dynamics, since viscous or inertial effects^{31, 100} can be important in flip-chip alignment or printing.

Curvature of capillary bridges as a competition between wetting and confinement



[This chapter is reprinted (with minor modifications) with permission from: Broesch, D; Dutka F; Frechette, J. *Langmuir* **2013**, 29, 15558-15564 Copyright 2013 © American Chemical Society]

4.1. Introduction

In a narrow slit pore geometry a capillary bridge is confined between two long solid plates or strips, as illustrated in Figure 4.1. The narrow slit pore geometry is a simple model system for the infiltration of fluid in porous media^{2-4, 61, 101}, the investigation of capillary condensation and nucleation⁴⁰⁻⁴⁴, the design of microfluidic channels¹⁶⁻¹⁸, bio-inspired adhesion³⁶, or for dispensing fluid³⁹. In the case where the

plates supporting the bridge do not have an infinite width, the capillary bridge has anisotropic wetting properties: the fluid can spread along the length of the solid strip but is pinned by its width, see Figure 4.1. Recently we showed how capillary bridges in a narrow slit pore geometry were created by inserting a liquid drop across two rectangular pillars that possessed both a physical and chemical heterogeneity.⁵² These experiments allowed us to visualize the morphological evolution of the bridges as they were stretched at constant volume. Our results highlighted how confinement by the strip leads to a surprising result: the Laplace pressure created by the capillary bridge goes from negative to positive as the height of the slit pore is increased (see Figure 4.1). Said differently, the width of the capillary bridge becomes larger than the width of the supporting strip with an increase in height such that the mean curvature of the bridge changes sign and goes from negative (concave bridge) to positive (convex bridge). These experimental results were also in excellent quantitative agreement with Surface Evolver simulations.

A change in sign from negative to positive in the mean curvature of a liquid bridge at constant volume appears in other cases where a bridge is supported by anisotropic surfaces. For example, simulations of a capillary bridge across two perfectly wetting strips also displayed a region where the mean curvature was independent of volume and where a change in sign in mean curvature was observed as the pore height was increased.⁹² A similar wetting transition was also predicted for the capillary filling of electrospray ionization sources³⁹. Similarly, in wedge geometry¹⁰²⁻¹⁰³ it was found that increasing the opening angle of the wedge resulted in an increase in the mean curvature of the liquid bridge and also changed its sign from negative to positive.

Here we report of a simple theory that predicts the transition from a negative to positive Laplace pressure as the height of a capillary bridge in slit pore geometry is increased at constant volume. The theory provides a simple and intuitive physical description for our experimental results that is significantly less computationally intensive than Surface Evolver simulations. The theory relies on three approximations for the geometry of the bridge. The resulting analytical form is in good agreement with experimental results for the increase in the pinning angle as the bridge height is increased. We also show excellent agreement with the change in mean curvature and can predict at which height the bridge will go from concave to convex. We found that at large slit pore heights this analytical argument starts to fail and discuss the origin of this departure for different wetting angles of the solid strip.

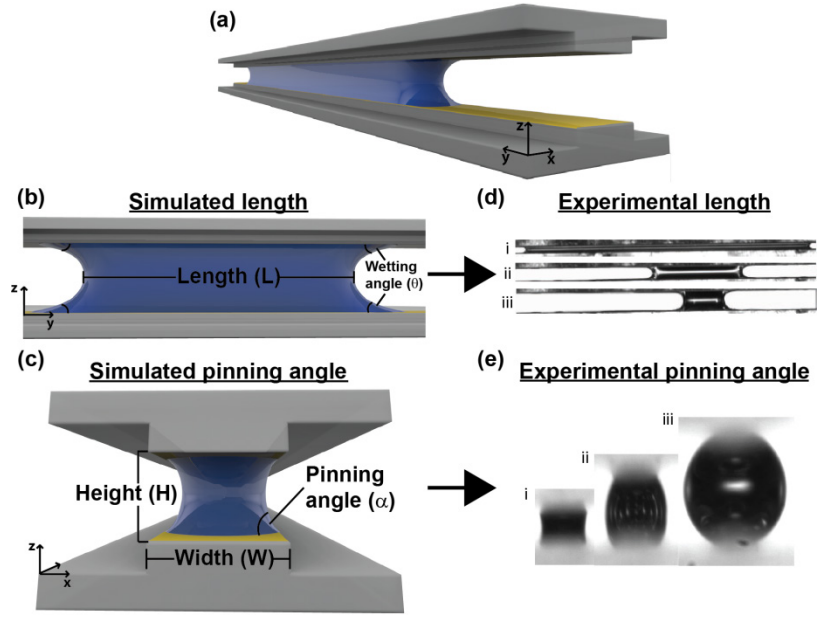


Figure 4.1: Capillary bridge in slit pore geometry. (a) Three quarters view, (b) Side view and (c) Front view. Images were rendered in Cinema 4D using data from Surface Evolver simulations. Representative experimental results for the length (d) and the pinning angle (e) are also shown.

4.2. Materials and Methods

4.2.1. Simulations

We employ the Surface Evolver software⁵⁹ package in which a finite element method is employed to minimize the free energy of solid-liquid-vapor systems under a set of user-defined constraints. The package uses the gradient descent method to minimize the free energy of the system so as to obtain properties at equilibrium such as Laplace pressure, area of the liquid-vapor interface, and energy. For the slit pore geometry, symmetry along the length and width of the capillary bridges is exploited to reduce the

computational time of the simulations. Symmetry along the height cannot be exploited due to instability modes that can affect bridge break up in that direction⁹². The system is considered to be at equilibrium when a change of less than 10^{-7} energy units is observed after at least four gradient descent iterations. Three different wetting angles are explored in our simulations, $\theta = 15^\circ$, 30° , and 60° , which are accessible experimentally. The range of pore heights (H) probed in the simulations are always lower than the capillary length of the system, so body forces such as gravity are not considered. The pinning angles (α) are extracted from the center of the liquid bridges (L/2) by using the image analysis software ImageJ to measure the angle the liquid-vapor interface makes with the solid substrate.

The mean curvature of the liquid bridges is calculated directly from the simulations using the Lagrange multiplier of the volume constraint (pressure) obtained at equilibrium and the surface tension using the Young-Laplace equation ($\Delta P = 2\kappa\gamma$). Here κ is the mean curvature, γ is the surface tension (measured value for water-glycerol was 51 dyn/cm), and ΔP is the Laplace pressure. Local radii of curvature at different points on the capillary bridge are calculated manually from the position of the vertices that represent the surface of the capillary bridge with minimal energy. The least square method is used to find the radius that best fits the vertices adjacent to and within the plane of the point of interest.

4.2.2. Experiments

The experiments were described in our previous work and only the salient points are mention here for clarity.^{52, 54} Liquid bridges were formed in a slit pore that consisted

of two aligned long pillars that were mounted facing each other. The pillars were hydrophobic with a top surface that was functionalized to provide a large wetting contrast between the top surface and the sidewalls ($\Delta\theta \approx 100^\circ$) and the liquid was a water-glycerol mixture. A custom-built microstage apparatus was employed to align the pillars and to vary the height of the pore in increments of $1\mu\text{m}$. A CCD camera was then used to image the pinning angle and length of the capillary bridges. The pictures were analyzed using the ImageJ software package.

4.3. Results and Discussion

4.3.1. Theory

At a given volume consider a liquid bridge in a narrow slit pore with a height H and constrained on a strip with a width W (see Figures 4.1 and 4.2). We assume that a bridge is formed at the given volume, width of the strip, and wetting angle. The morphological transition between the bridge state and the sessile droplet attached to one of the wall is beyond the scope of this article⁹⁴. Here we consider the case where the wetting strip is always much longer than the length of the capillary bridge. In this limit the contact angle formed at the end of the strip is determined by the wetting angle of the strip, θ (Figure 4.1b), and this wetting angle is maintained as the bridge advances or recedes. In contrast, a physical and/or chemical heterogeneity pins the triple contact line on the length of the bridge as characterized by the pinning angle, α (Figure 4.1c). In this limit we have shown that the pinning angle is only a function of H/W and θ and is independent of the volume of the capillary bridge⁵². In the absence of body forces (the

case considered here), the mean curvature, κ , must be the same at all points on the surface of the bridge. In Equation 4.1 we equate the mean curvature estimated at two particular points on the bridge, labeled M and N in Figure 4.2.

$$\kappa = -\frac{1}{2r} = \frac{1}{2} \left(\frac{1}{R_2} - \frac{1}{R_1} \right) \quad (4.1)$$

When the bridge has a high aspect ratio (L/W), we first approximate that the curvature of the bridge surface at point M in the C_1C_2 -plane can be neglected when compared with $1/r$, meaning that we have translational invariance along the length of the bridge. As such, the mean curvature at point M is $\kappa = -1/2r$. If we make a second approximation that the shape of the bridge interface in the A_1A_2 - and B_1B_2 -planes can be described by the arcs of circles, the radii of curvature are equal to:

$$R_1 = \frac{H}{2\cos\theta} \quad (4.2)$$

$$r = \frac{H}{2\cos\alpha} \quad (4.3)$$

where θ and α are the wetting and pinning angles, respectively. We make a final approximation that the radius R_2 can be approximated by $W/2$ (see Figure 4.2d). Then Equation 4.1 can be rewritten as:

$$\kappa = -\frac{\cos\alpha}{H} = \frac{1}{W} - \frac{\cos\theta}{H} \quad (4.4)$$

Equation 4.4 now provides a simple expression relating the mean curvature at point N with the height (H/W) of the pore and wetting properties of the strip (θ). From this

expression we see that when increasing the height of the bridge the mean curvature also increases, in agreement with our results from experiments and simulations.⁵²

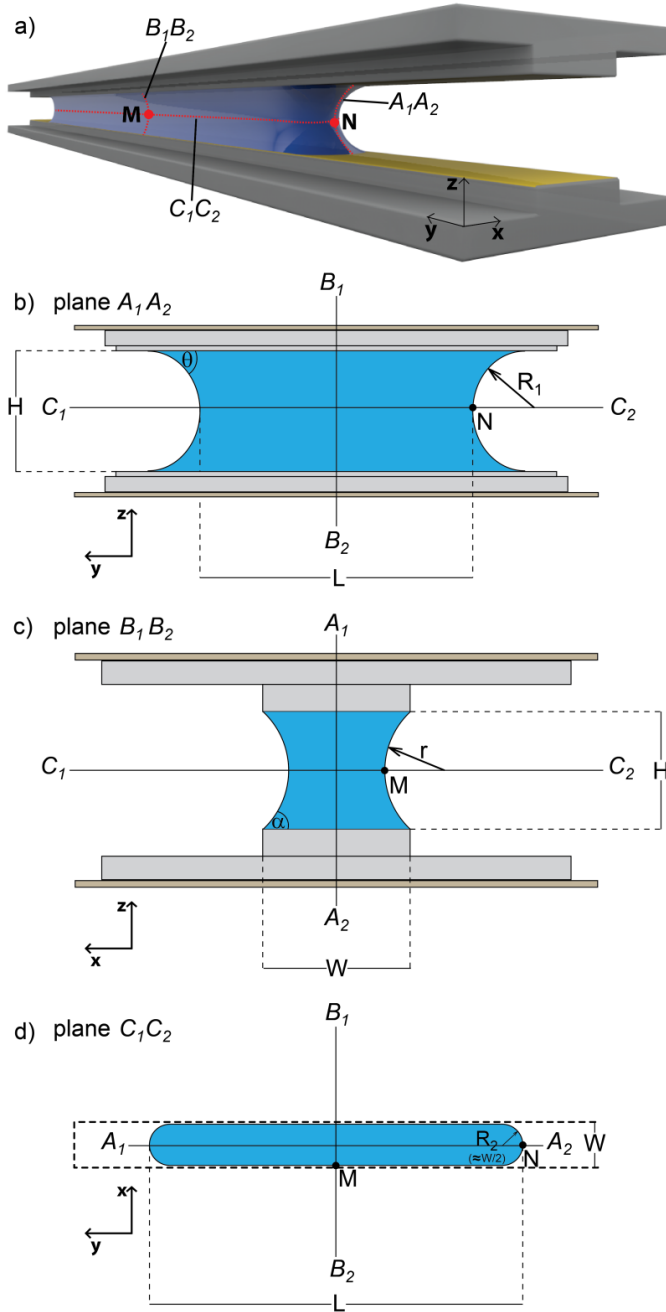


Figure 4.2: Schematic of the capillary bridge. The theory estimates the curvature at points M and N on the bridge.

Based on these approximations we can predict the mean curvature solely based on the wetting properties of the strip and its width. We do not need to know anything else about the capillary bridge (such as its volume or its length for example) and we can obtain the mean curvature without having to perform energy minimization on the complex slit pore geometry. For instance, this equation can be re-arranged (Equation 4.5) to show that the pinning angle, which is a parameter that can be readily measured experimentally, increases with an increase in height, as we observe in our experiments.

$$\cos\alpha = -\frac{H}{W} + \cos\theta \quad (4.5)$$

This analysis provides a very intuitive understanding of our experimental results. As seen in Equation 4.5, it is the balance between the confinement (H/W) and wetting properties ($\cos\theta$) of the strip that dictates the mean curvature or the pinning angle ($\cos\alpha$) of a capillary bridge in slit pore geometry. For instance we see from Equations 4.4-4.5 that for $H/W = \cos\theta$ the curvature changes sign from negative to positive as the pinning angle α becomes greater than $\pi/2$. We also see that as the confinement of the bridge decreases by having strips with larger width, the contribution of the wetting properties become more important and the bridge needs a larger height for its curvature to change sign. Moreover, we recover the case of an un-pinned capillary bridge with fixed contact angle θ at infinite width. Finally this analysis would predict that the transition between negative and positive mean curvature would occur at lower H/W as the wetting angle of the strip increases.

The arguments presented above are based on three simple assumptions for the geometry of the capillary bridge (Figure 4.2):

- I. Translational invariance: the curvature of the bridge surface at point M in the C_1C_2 -plane can be neglected compared to $1/r$, because of the large aspect ratio (L/W) of the bridge;
- II. Circle approximation: the shape of the bridge in the A_1A_2 - and B_1B_2 -planes can be described by arcs of circles;
- III. The radius R_2 can be approximated by $W/2$.

Note that only the last two approximations are necessary to predict the mean curvature (and associated Laplace pressure) of the capillary bridge (using Equation 4.4). The first approximation is necessary to predict a pinning angle (Equation 4.5).

The validity of the first approximation was briefly discussed in our previous publication⁵², and we suspect that it is the approximation that introduces the smallest error relative to the experiments and simulations. The second approximation is often employed in papers describing capillary bridges^{28, 104}, but it is also known to cause large errors¹⁰⁵⁻¹¹⁰, when compared with more accurate description of the bridge surface. The third approximation is solely based on physical intuition as an order of magnitude. One can roughly inscribe a circle in the bridge surface in the C_1C_2 -plane, and thus one can approximate $R_2 = W/2$. To a first order we assume that R_2 would remain constant with the height of a capillary bridge confined by a strip of width W . To assess the validity of this simple theory we need to compare its predictions with simulations and experimental results. When comparing with the simulations, the approach we employ is twofold: 1) we extract local radii of curvature on the bridge by fitting circles to the vertices at the point of interest, and 2) we compare the predicted mean curvature of the bridge based on individual assumptions with the one obtained from the pressure in the simulations.

Finally we use Equation 4.5 to compare the pinning angle measured experimentally with the one predicted based on the properties of the confining strip. Note that Equations 4.1-4.5 should also apply for $\theta > 90^\circ$. In this case, the curvature should always be positive as there is no interplay between positive and negative curvatures at point N, as it is for $\theta < 90^\circ$. Therefore, the bridge should remain convex upon changing the height of the slit. There are no limitations for the wetting angles within this theory as long as the liquid forms a bridge in the slit. The mean curvature in the limiting case of $\theta = 90^\circ$ is shown in Figure 4.7.

Test of the individual assumptions

I. Translational invariance

In Figure 4.3 we map sections of capillary bridges in the C_1C_2 -plane (see Figure 4.2d). For both wetting angles shown we can qualitatively see that the width of the bridge does not change along its length, except near the very end of the bridge, confirming that the curvature at point M in the C_1C_2 -plane is essentially zero at all heights shown. We also see that by increasing the wetting angle to $\theta = 60^\circ$ the bridge tends to be more axisymmetric and that the assumption of translational invariance should be less accurate for $H/W > 1.5$. Increasing the wetting angle decreases the aspect ratio (L/W) of the bridge, which, in turn, introduces curvature in the C_1C_2 -plane at point M.

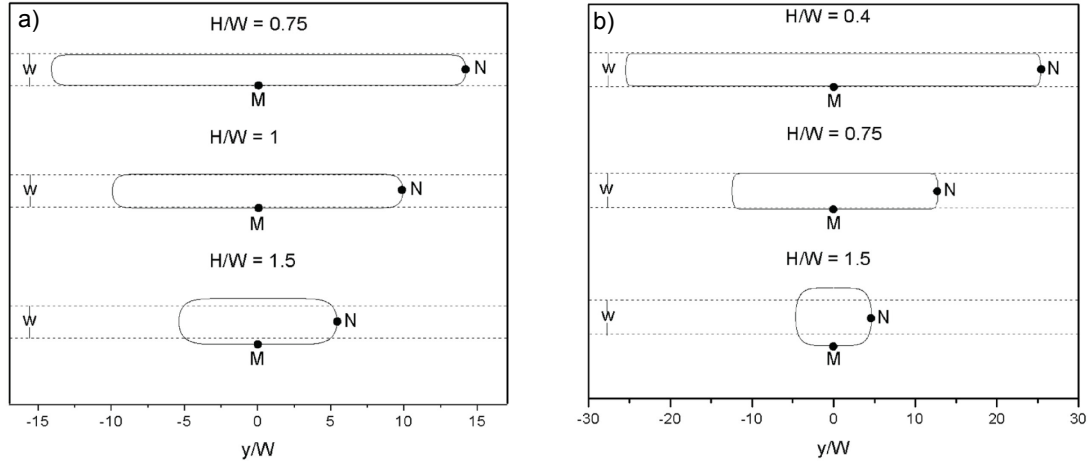


Figure 4.3: Section of the capillary bridge in the C_1C_2 -plane (see Figure 4.2d for the definition of the plane and coordinate system) extracted from the minimal energy shape obtained from Surface Evolver simulations at different heights and for a wetting angle of a) 15° , and b) 60° . Also shown is the transition from a bridge with negative mean curvature to a bridge with positive mean curvature: the width of the bridge is less than the width of the strip at low H/W and increases to become larger than the width as H/W increases.

The curvature at point M calculated using Equation 4.4 relies on both translational invariance and the circle approximation. However, we can test only the validity of the first approximation more specifically and quantitatively by measuring the radius of curvature r at point M (Figure 4.2c) from the position of the vertices in the minimal energy shape obtained from the Surface Evolver simulations. We then calculate the mean curvature ($\kappa = -1/2r$) assuming translational invariance and compare this predicted mean curvature with the one from the output of the energy minimization of the full capillary bridge in the Surface Evolver simulations. As we see from Figure 4.4, the translational invariance approximation is quite successful to describe the curvature of the

bridge for $H/W < 2$ for the three wetting angles investigated here. We see that as $H/W > 2$ the assumption tends to underestimate the mean curvature as the capillary bridges become more axisymmetric and end effects become more important. Note that this assumption works particularly well in the region where the mean curvature of the bridge changes sign.

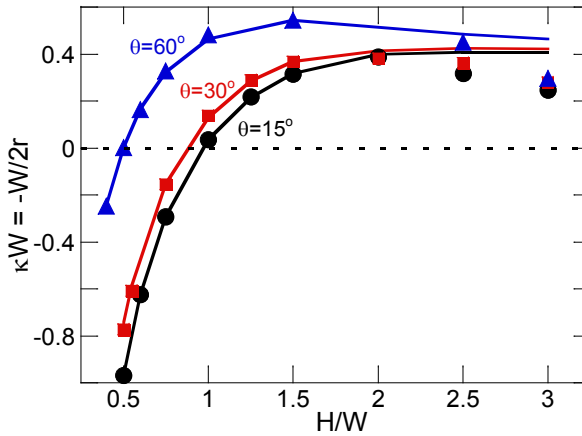


Figure 4.4: Comparison between theory and simulations to test the translational invariance assumption for capillary bridges formed on strips with three different wetting angles. The mean curvature normalized by the width of the strip, κW , has been obtained in two separate ways. The lines correspond to the mean curvature obtained from the Laplace pressure of the capillary bridge based on Surface Evolver simulations while the data points represent the predictions based on extracting r at point M from Surface Evolver simulations and using Equation 4.1.

II. Circle approximation

We use the circle approximation at points M and N (Equations 4.2 and 4.3). Testing this assumption at point N is straightforward: we can compare the curvature R_1 obtained from the surface of the capillary bridges with minimal energy with the value predicted based only on the height and the wetting angle. As shown in Figure 4.5a we see that the curvature obtained based on the circle approximation follows the general trend obtained in the simulations but overestimates the values from the Surface Evolver at most heights. The average error in estimating the curvature using the circle approximation is 30% for $H/W < 1.5$ for $\theta = 15^\circ$. As the wetting angle increases there is better agreement between the theory and the simulations, for example the average error due to the circle approximation is only 10% for $H/W < 1.5$ for $\theta = 60^\circ$. This trend is the same as the one observed for interacting spheres (or a sphere and a plane) where the error introduced by the circle approximation decreases with an increase in wetting angle^{28, 105}. In all these cases the circular approximation overestimates the curvature, as is also in our case where the curvature in A_1A_2 plane equals $-1/R_1$, (see Figure 4.5a). We note that in the limit of $\theta=0^\circ$ the bridges form long tails⁹² that can reach the end of the strip and the role of the precursor film (which we ignore in both the simulations and theory) might be important¹¹¹.

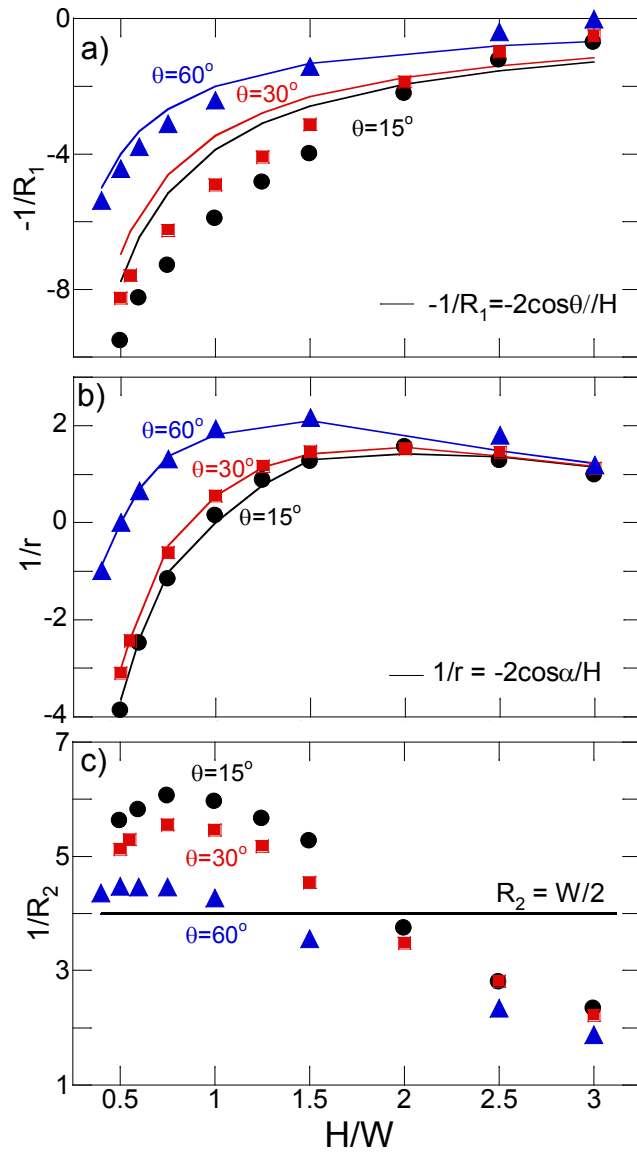


Figure 4.5: Individual radii of curvature (in mm-1) calculated at a,c) point N, and b) point M. The data points correspond to curvatures calculated based on the Surface Evolver simulations for a width of 0.5 mm and a volume $(V/W^3)=20$. The radii of curvature were obtained for three different contact angles for the solid strip supporting the bridge (with \bullet for $\theta = 15^\circ$, \blacksquare for $\theta = 30^\circ$, and \blacktriangle $\theta = 60^\circ$). The solid lines correspond to theoretical predictions for the three wetting angles considered here.

At point M we need the value of the pinning angle (α) to test the validity of the circle approximation. We use the output of the Surface Evolver simulations to extract the values of the pinning angle in the middle of the bridge (at $y/W = 0$, see Figure 4.3) and we then use Equation 4.3 to calculate r . We then compare the predicted value of r with the one obtained by fitting a circle at point M from the morphology of the bridge obtained from Surface Evolver simulations. As seen in Figure 4.5b, the circle approximation works quite well at Point M for all H/W and wetting angles considered. Therefore at Point M the main error introduced is with the translational invariance approximation (Figure 4.4) for which we start to see deviation at $H/W > 2$.

III. The radius R_2 can be approximated by $W/2$

The final approximation is that of a constant radius of curvature $R_2 = W/2$ at Point N. We test this approximation by measuring the local radius of curvature R_2 at point N from the simulations and compare it with the predicted value of $W/2$ (see Figure 4.5c). Similarly to what we observe with the other principal radius at Point N (Figure 4.5a) we find that this approximation introduces significant error, especially for the case of $\theta = 15^\circ$ where the average error is 30% for $H/W < 2$. We also see that contrary to the approximation, R_2 is not constant at all heights. This error decreases with the increase in wetting angle to reach 10% for $\theta = 60^\circ$. As expected, when the pinning angle $\alpha < 90^\circ$ (small values of H/W), then the width of the bridge in C_1C_2 plane is smaller than W (see Figures 4.2c and 4.3) and $R_2 < W/2$. So in this case the theoretical assumption $R_2 = W/2$ underestimates the curvature in C_1C_2 plane (see Figure 4.5c). On the other hand, for $\alpha >$

90°, the radius $R_2 > W/2$ and the theoretical assumption overestimates the curvature in the C_1C_2 plane.

Based on the circle and $R_2=W/2$ approximations we can test the validity of the theory in predicting the mean curvature of the capillary bridge (and by extension its Laplace pressure and capillary forces). Note that we have shown previously that the simulations are also in excellent agreement with experiments.⁵² Shown in Figure 4.6 is the comparison between the mean curvatures obtained from the theory at Point N and the values obtained from the Surface Evolver simulations. Somewhat surprisingly we find excellent agreement between the theory and the simulation for $H/W < 1.5$. The theory works especially well to predict at which height the curvature changes sign (go from concave to convex) and the dependence on wetting properties for this transition. Interestingly, only parameters that are known *a priori* (height, width, and wetting angle) are necessary to predict the mean curvature of a capillary bridge in slit pore geometry. The agreement shown in Figure 4.6 is unexpected as there is significant error introduced by the theory in the values of both R_1 and R_2 (Figure 4.5). Basically, at low H/W the magnitude of R_1 and R_2 is similar. As we explained above the theory overestimates the curvature in A_1A_2 plane, but underestimates the curvature in C_1C_2 plane, and according to Equation 4.1 the introduced errors cancel each other, and thus we get so good quantitative agreement of theory and simulation. As the height increases the contribution of R_2 to the mean curvature starts to dominate ($1/R_2 \gg -1/R_1$) and there is no longer cancellation of errors and we see that the mean curvatures predicted by the theory overestimate the ones from Surface Evolver (and experiments). Therefore the third approximation is the one that introduces the most error in the analysis at Point M.

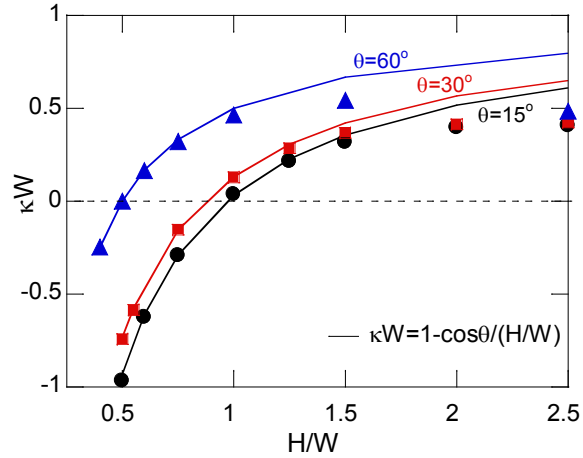


Figure 4.6: Mean curvature normalized by the width (κW) as a function of height for different wetting angles (with \bullet for $\theta = 15^\circ$, \blacksquare for $\theta = 30^\circ$, and \blacktriangle for $\theta = 60^\circ$). The lines represent predictions from the theory for the mean curvature at point N ($\kappa W = 1 - \frac{\cos \theta}{H/W}$). The data points correspond to the results of Surface Evolver simulations with volume $V/W^3 = 20$ and width $W = 0.5\text{mm}$.

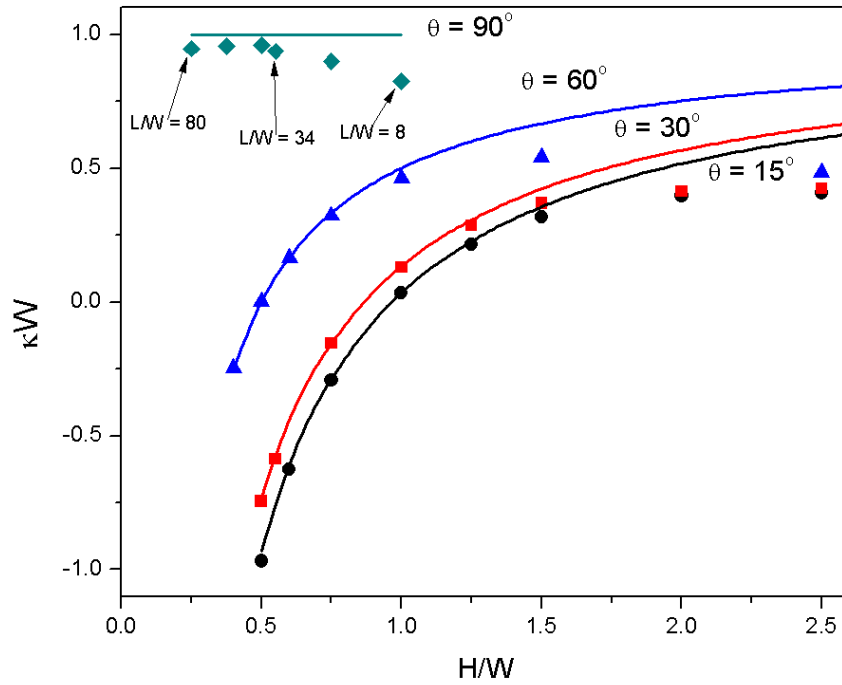


Figure 4.7: Mean curvature normalized by the width (κW) as a function of height for different wetting angles (with \bullet for $\theta = 15^\circ$, \blacksquare for $\theta = 30^\circ$, \blacktriangle $\theta = 60^\circ$ and \blacklozenge $\theta = 90^\circ$). The lines represents predictions from the theory for the mean curvature at point N ($\kappa W = 1 - \frac{\cos \theta}{H/W}$). The data points corresponds to the results of surface evolver simulations with volume $V/W^3 = 20$ and width $W = 0.5$ mm.

4.3.2. Overall comparison with experimental data

We can also compare the predictions from the theory to our experimental results using Equation 4.5 in which we predict a linear relationship between $\cos \alpha$ and the height

of the bridge. Shown in Figure 4.8a are our experimental results along with the predictions from the theory. We see good agreement between the theory and the experiments for $1.0 < H/W < 1.5$. For other heights, however we see clear differences between the theory and the experiments. For $H/W > 1.5$ the discrepancies between the theory and the experiments are due to the breakdown of the first and (mostly) the third approximation, as discussed in the previous sections. For $H/W < 1$ the difference between the theory and the experiments are not due to a failure of any of the approximations. Rather the differences are caused by the fact that a small tilt (ϕ) is present between the two strips ($\phi \approx 0.1^\circ$). At low H/W the capillary bridge is long and the effect of the tilt is significant. We can confirm that the deviation between the theory and the experiments at low H/W is due to the tilt by comparing our experimental results with Surface Evolver simulation with and without a 0.1° tilt (Figure 4.8b). As seen, the theory and simulation in the absence of tilt agree very well at low H/W , but for $H/W < 1$, tilt has to be included in the simulation to obtain agreement with our experimental results (see the difference between the solid and dashed lines for $H/W < 1$ in Figure 4.8b). This simple theory, as is, does not account for tilt between the supporting pillars. The tilt is real and is observed experimentally. It is understandable that the tilt will affect the pinning angle as it changes the height locally. We suspect that experiments without tilt would show agreement with the theory based on the agreement with the simulations at low H/W .

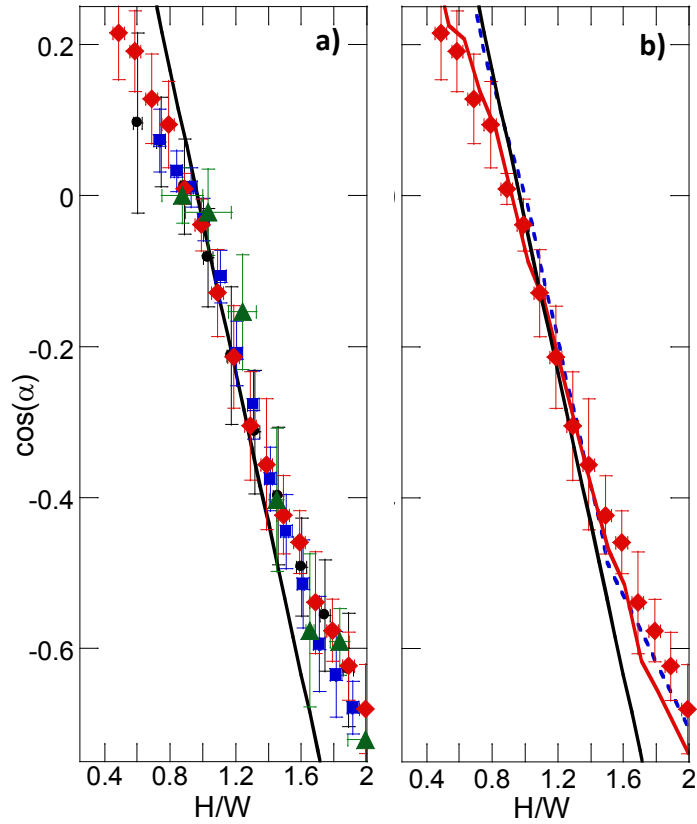


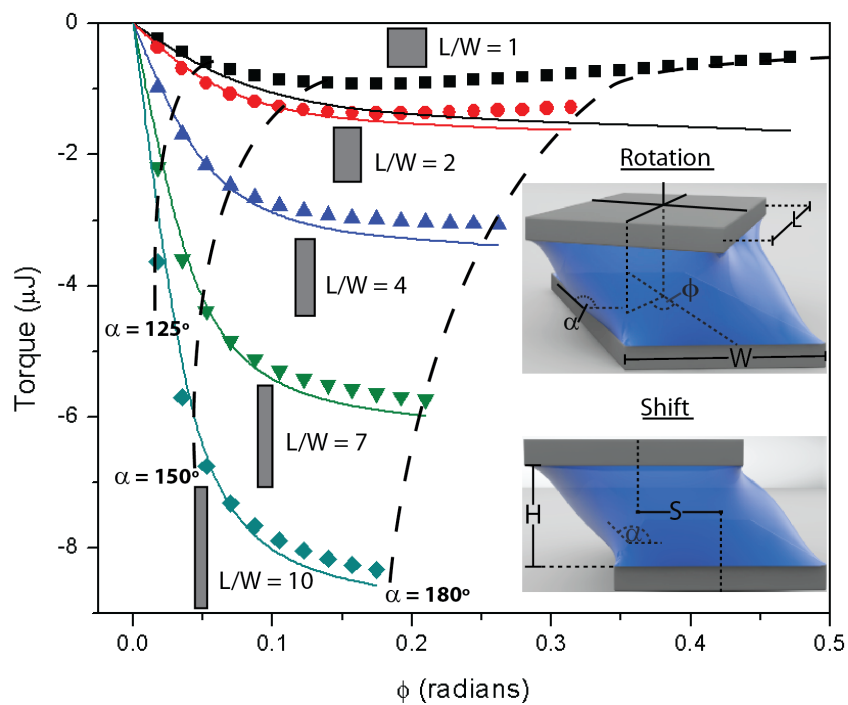
Figure 4.8: Comparison between experiments, SE simulations, and theory. a) experimental results along with prediction for the theory (line). The conditions for the experiments are \blacktriangle for $V=1\mu\text{L}$ and $W = 0.25$ mm, \bullet for $V = 1\mu\text{L}$ and $W = 0.35$ mm, \blacklozenge for $V = 2.5 \mu\text{L}$ and $W = 0.5$ mm, and \blacksquare for $V = 5 \mu\text{L}$ and $W = 0.5$ mm. b) Comparison between Surface Evolver simulation, theory, and experiments for $V = 2.5 \mu\text{L}$ and $W = 0.5$ mm. The solid black line corresponds to the theory, the dashed line to the simulation without tilt, and the thin red line the simulation with a 0.1 degree tilt.

4.4. Conclusions

We present a simple theory to predict the morphological evolution of a capillary bridge in slit pore geometry. The theory is based on three simple geometric arguments (translational invariance, the circle approximation, and the relationship between the radius of curvature and the width of the confining strip). The theory highlights how the competition between the wetting and confinement of the supporting solid substrates lead to a change in sign in the mean curvature of the bridge. We show good agreement between the theory, Surface Evolver simulations, and experimental results. More specifically we can predict very well the height at which the curvature of the capillary bridge will change sign. However, the range of height for which the theory and the experiments agree is more limited due the tilt present between the plates in the experiments. As the height of the bridge increases we show that the approximations behind the theory start to break down and that the theory overestimates the mean curvature of the capillary bridge. We show that cancellation of errors in the estimation of the curvature plays an important role in demonstrating the agreement between theory and simulation. The first approximation to fail is that of $R_2 = W/2$, which occurs at $H/W > 1.5$.

Role of substrate aspect ratio on the robustness of capillary alignment

[This chapter is adapted from a manuscript accepted to Applied Physics Letters]



Capillary forces originate from the tendency of a fluid interface to minimize its area and are a powerful means to direct the assembly of solid objects^{45, 112-114}. In particular, capillary forces where a liquid meniscus is present in the form of a capillary bridge have been exploited for the passive assembly of 3D structures²²⁻²⁵ and to align large numbers of submicron-sized devices in parallel¹⁹⁻²¹. An example is the capillary-

based alignment scheme known as “flip-chip assembly”, which has evolved as an advancement of traditional pick and place circuit packaging^{20, 45-51}. In flip-chip assembly, molten solder is the most common liquid medium due to its high surface tension and good conductivity.^{20, 45-46}

The shape of the substrates, along with the choice of liquid, dictate the aligning forces and torques exerted by a capillary bridge. The majority of flip-chip devices and investigations of their alignment are limited to simple (square or circular) substrate shapes with very high levels of symmetry.^{20, 55, 86, 115-121} Moreover, the majority of studies on the role of substrate shapes focus on restoring forces associated with lateral substrate perturbations (see Figure 5.1b).¹²¹⁻¹²⁹ Torques associated with rotational perturbations have been explored through simulation for liquid bridges between square pads²⁴, cylindrical rods¹³⁰⁻¹³¹, and experimentally for substrates with sinusoidal perturbations⁸⁰. Here, we study the effect of substrate geometry on capillary interactions by extending the standard square substrate design to rectangles with increasing aspect ratio (see Figure 5.1). We explore both restoring forces and torques when the substrates are perturbed either laterally or rotationally away from equilibrium. Simulated results are obtained using the finite element software package Surface Evolver⁵⁹ and a theory and experiments are presented that validate the simulations.

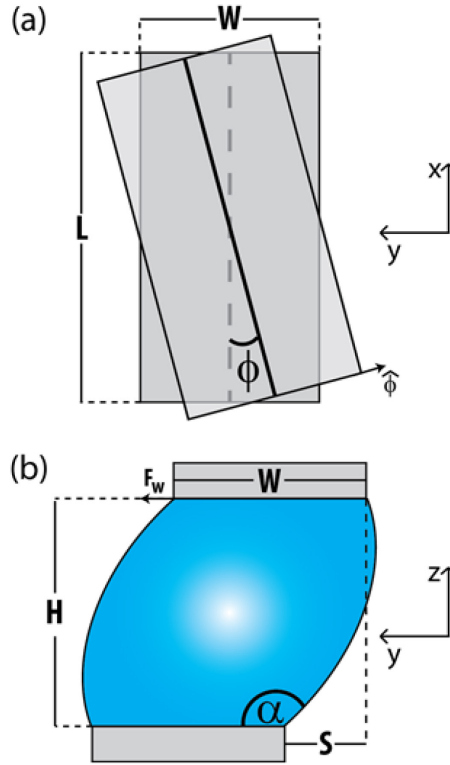


Figure 5.1: (a) Top down view of substrates under a rotational perturbation ($\hat{\phi}$) and (b) frontal view of substrates under a shift perturbation (S). F_w is the shift restoring force associated with a displacement S .

Each simulation involves a capillary bridge (with a volume V) formed between two identical substrates (with area, A , and aspect ratio, L/W) facing each other and separated by a height, H . For each simulation the height was set as the equilibrium height between two perfectly aligned substrates ($\phi = 0$ and $S = 0$). Next, the top substrate is either rotated around its center or shifted perpendicular to the strip. After each perturbation, the configuration of minimum energy is obtained and the associated capillary forces and torques are calculated. The criterion for convergence is a change of

less than 10^{-6} energy units after at least four convergence iterations. An additional constraint for the simulations is that the triple contact line is confined to the substrate's surface but is not forced to be pinned to its edges.

The simulations show that larger torques are necessary to rotate substrates with increasing aspect ratios (for a constant area and volume, see Figure 5.2). This implies that increasing L/W leads to a higher resistance of the substrates towards rotational perturbations. We find that as the substrate aspect ratio increases, so too does the maximum local pinning angle (α) at a given rotation as shown by the dashed lines in Figure 5.2. These trends can be understood in terms of a larger misalignment between substrates with higher aspect ratios at a given rotation ϕ , which is characterized by the arc length $L\phi/2$. Note that the pinning angle along the triple contact line of the bridge is not constant and varies along the perimeter of the substrates. The maximum pinning angle is observed on the rotating substrate near the corners that lie in the opposite direction of the rotation vector (see $\hat{\phi}$ in Figure 5.1 and Figure 5.3). Corners that lie in the direction of the rotation vector are points of pinning angle minima. Data for rotation angles larger than the smallest one displaying a local pinning angle of 180° are not shown. We would expect most experimental systems to surpass their canthotaxis limit once $\alpha = 180^\circ$, causing depinning of the liquid from the substrate surface.⁵⁵ It is likely that larger rotations are not experimentally accessible configurations. A consequence of maintaining a constant liquid volume and substrate area (as in Figure 5.2) is that the bridge equilibrium height will remain constant for different substrate aspect ratios. We can estimate the equilibrium height in the absence of body forces as $H = V/A$.^{55, 118, 129} As long as the liquid volume

and the substrate area are maintained, the equilibrium height is invariant with aspect ratio. Scripts were written in Surface Evolver to find the equilibrium height of perfectly aligned substrates before they were either shifted or rotated. Figure 5.4 shows that for all aspect ratios, liquid volumes, and substrate areas, the equilibrium height is equal to the volume divided by the substrate area ($V = AH$).

Therefore, increasing the aspect ratio could be a favorable method for increasing alignment torques in currently established self-alignment systems (such as flip-chips or packaging), since liquid volume and height tolerances should not need to be changed.

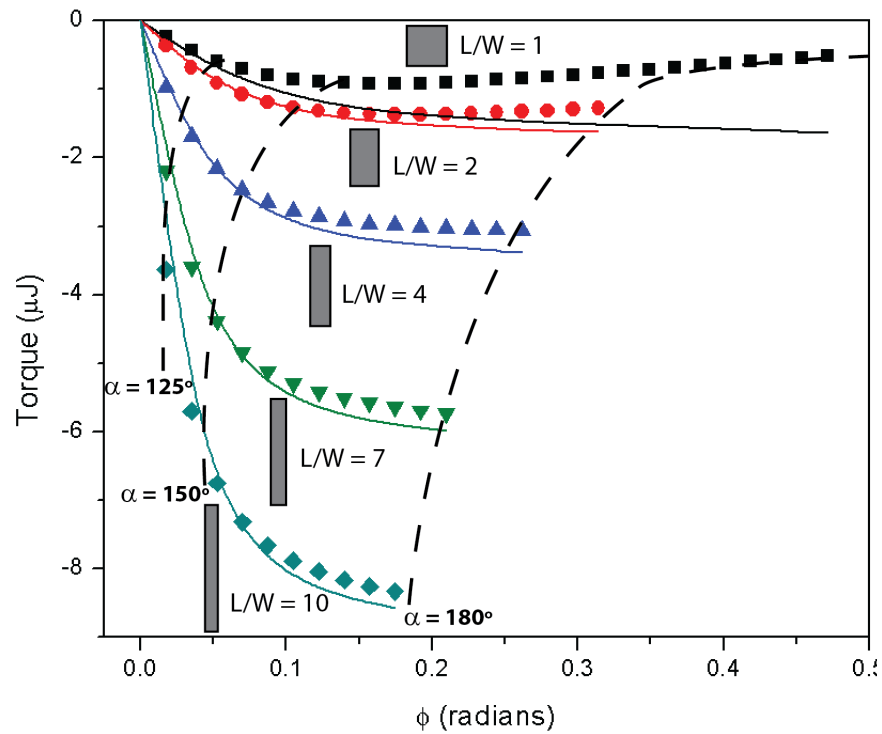


Figure 5.2: Simulated restoring torque for different rotation angles obtained for capillary bridges formed between substrates of different aspect ratios. The volume of liquid is $4.9 \mu\text{L}$ and the substrate area is 25 mm^2 . The solid lines are predictions from Equation 5.1. Dashed lines represent maximum local pinning angle observed.

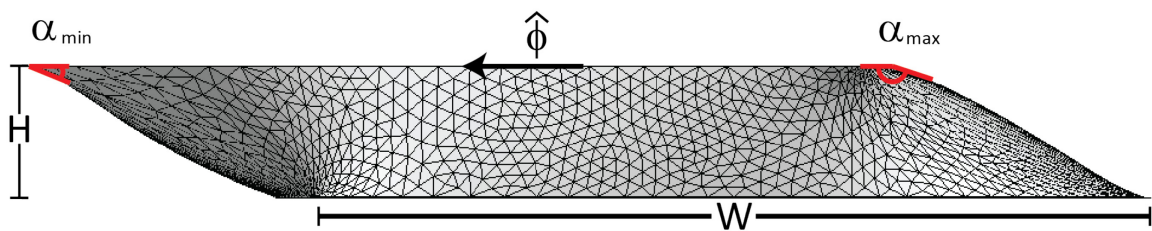


Figure 5.3: View of capillary bridge normal to the width of the top substrate when $\phi = 10^\circ$. $L/W = 4$, $V = 9.8 \mu\text{L}$.

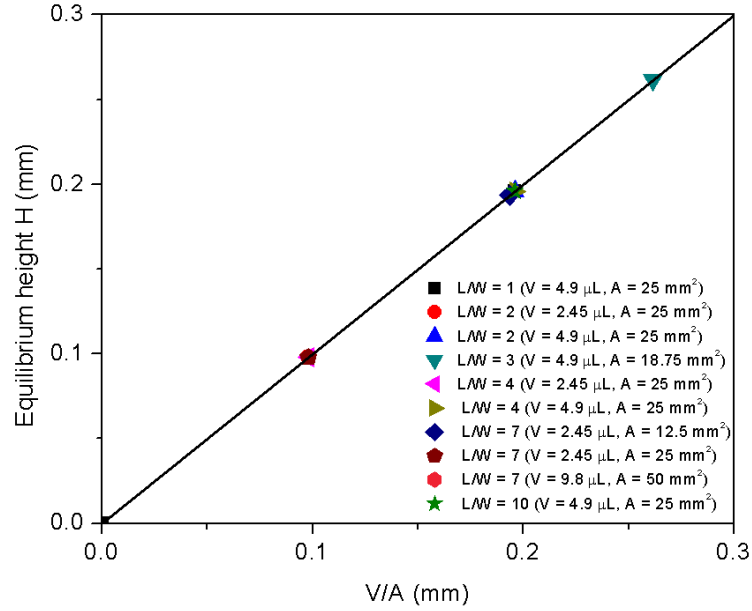


Figure 5.4: Simulated equilibrium heights vs. liquid volume over substrate area for different aspect ratios, volumes, and substrate areas. The solid line represents a slope of 1.

A simple geometric argument can be used as a theory to predict the restoring torques shown in Figure 5.2. The restoring torque is estimated as an integral of the projected surface tension force in the ϕ direction (see Equation 5.1).

$$T = 4 \int_0^{L/2} \gamma \cos(\alpha) x dx \quad (5.1)$$

where γ is the liquid-vapor surface tension and (x) is the coordinate that lies in the direction of the substrate length (see Figure 5.1). The pinning angle is a function of the equilibrium height of the substrates, the substrate width, and the rotation angle ($\alpha = f(H, x, W, \phi)$).

To solve Equation 5.1, an explicit form for the pinning angle must be determined. Here we present a functional form for the pinning angle and the restoring torque given three assumptions: 1) the liquid interface is flat, 2) only the length contributes to the restoring torque, and 3) the triple contact line remains pinned to the sides of the substrate edge along its length. From Figure 5.5a we can see that an arbitrary point along the length of the substrate ($x, W/2$) will follow a circular trajectory as ϕ is increased. The position of this point in the y direction can be expressed as a function of x and ϕ .

$$y' = x \sin \phi + \frac{W}{2} \cos \phi \quad (5.2)$$

Figure 5.5b shows that when the liquid vapor interface is flat:

$$\alpha = \pi - \beta \quad (5.3)$$

where:

$$\beta = \tan^{-1} \left(\frac{H}{y' - \frac{W}{2}} \right) \quad (5.4)$$

$$\beta = \tan^{-1} \left(\frac{H}{x \sin \phi + \frac{W}{2} (\cos \phi - 1)} \right) \quad (5.5)$$

therefore the torque can be expressed as:

$$T = 4 \int_0^{L/2} \gamma \cos \left[\pi - \tan^{-1} \left(\frac{H}{x \sin \phi + \frac{W}{2} (\cos \phi - 1)} \right) \right] x dx \quad (5.6)$$

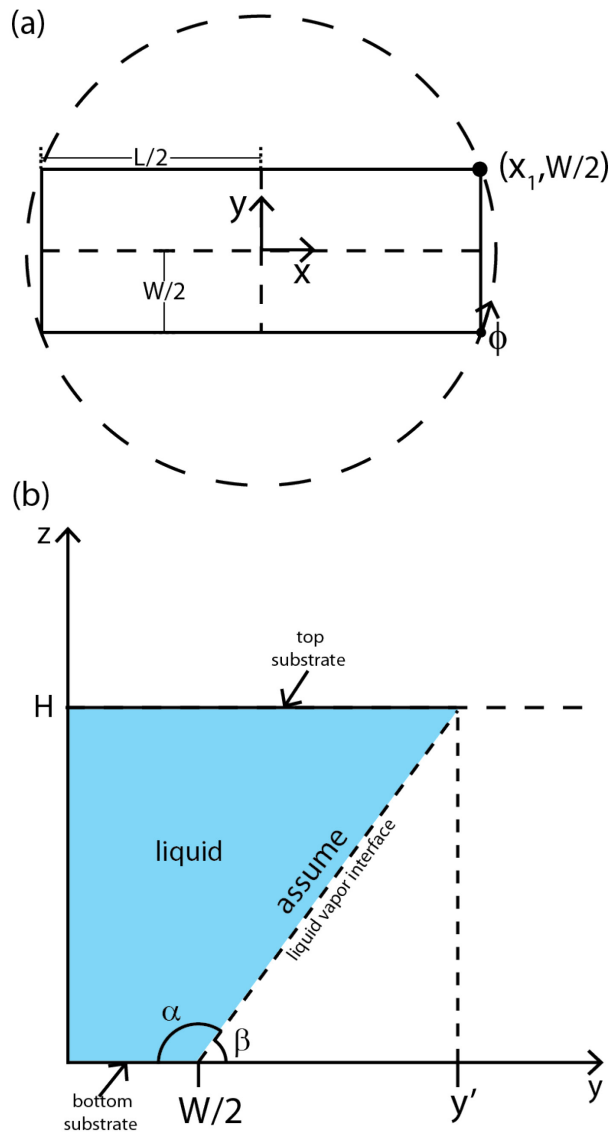


Figure 5.5: Schematic illustrating the assumptions present in deriving Equation 5.1. a) Top down view of flip-chip device ($\phi = 0$). b) Front view of flip-chip device (normal to width, $\phi > 0$). This perspective shows the pinning angle of the liquid bridge when the liquid vapor interface is assumed to be flat.

Solving this integral numerically leads to the solid lines in Figure 5.2. Despite the rather simple assumptions, the theory captures well both the trend and magnitude of the restoring torque as a function of the rotation angle. We can see that as the aspect ratio increases, the agreement between the theory and the simulations improves. This is an interesting result, as assumption 1 should get worse with increasing aspect ratio due to higher values of α reported for a given rotation angle (see Figure 5.2). Assumptions 2 and 3 however improve with increasing aspect ratio, leading to better agreement between Equation 5.1 and the simulations. Note that for the case of $L/W = 1$, the result from the theory was doubled to include contributions from all four sides.

To validate the simulations, experiments were performed to determine the role of aspect ratio on the maximum perpendicular shift or rotation achievable before the occurrence of depinning of a capillary bridge. The experiments were performed with pairs of plasma-treated PDMS rectangles of varying aspect ratios. The PDMS rectangles are placed facing each other in a custom built multi-axis microstage⁵²⁻⁵⁴ and a capillary bridge is formed by introducing water between PDMS surfaces. The bottom substrate is then rotated in increments of 1 degree or shifted by 100 μm until depinning of the liquid off of the substrate surface is observed (determined by imaging). Figure 5.6 shows the maximum achievable rotation angle or shift for the experiments was found to decrease as the substrate aspect ratio increases, in agreement with the simulations. Additionally, we can use the maximum rotation or shift obtained from the experiments as an input in the Surface Evolver simulation to extract a maximum local pinning angle. We find that the maximum pinning angle before depinning occurs is around 170° and only varies by about

10° for $1 \leq L/W \leq 6$, consistent with the fact that the maximum pinning angle should depend only on the sharpness of the substrate edge⁵⁵, which is invariant with aspect ratio.

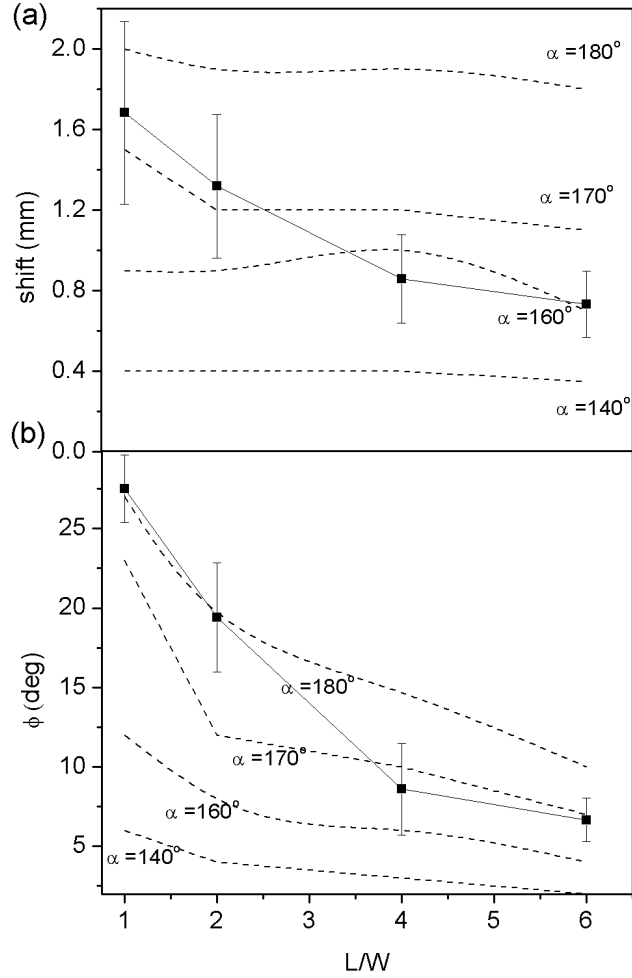


Figure 5.6: Maximum (a) shift normal to the length, and (b) rotation angle, ϕ , for substrates of different aspect ratios. Points represent experimental data while error bars represent the standard deviation of values obtained from multiple trials over three separate sample sets for each aspect ratio. The solid lines are meant to guide the eye, while the dashed lines represent pinning angle values obtained from simulations. Volume = 39 μL and substrate area = 1 cm^2 .

The importance of the aspect ratio on the restoring torque for different substrate areas, perimeters, and liquid volumes is shown in Figure 5.7a. Here we only show the data taken at the rotation angle where $\alpha = 180^\circ$ is first observed. In most cases, values reported in Figure 5.7a represent the maximum torques or restoring forces that can be achieved before depinning occurs. The torque increases with aspect ratio whether any two of the area, perimeter, or volume is kept constant, indicating that the higher torque values are truly an effect of aspect ratio, and not an artifact resulting from changes to other parameters. The increase in torque with aspect ratio scales with area when the area and volume are changed such as to keep the equilibrium height constant (Figure 5.7a). This illustrates the intrinsic importance of equilibrium height (a combination of volume and substrate area) to the magnitude of the restoring torques. For low aspect ratios ($L/W < 4$), the torque does not depend on the equilibrium height, volume or perimeter, as the curves in Figure 5.7a all collapse. For $L/W > 4$, we see departure from the master curve for trials with larger equilibrium heights. For the case of constant perimeter (Figure 5.7a), the magnitude of the torque increases more slowly with aspect ratio than for the constant area trials. This is expected, since increasing aspect ratio under constant perimeter (P) and volume requires a decrease in area, and hence, the equilibrium height must increase ($P = 2W \left(\frac{L}{W} + 1 \right)$). The inverse relationship between equilibrium height and restoring torque is in agreement with observations from the literature for square pad shapes.⁵⁵

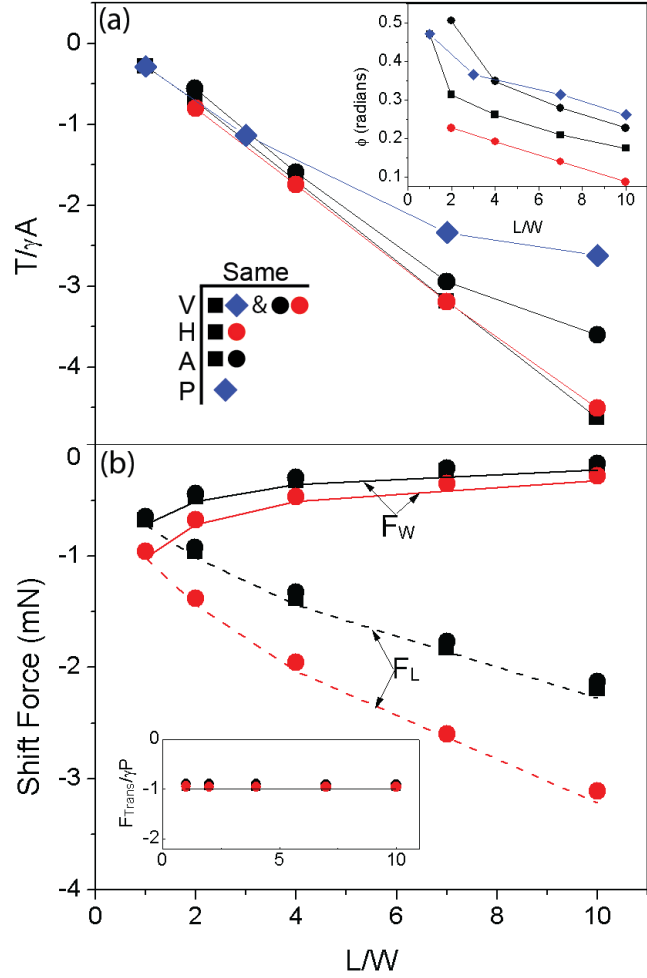


Figure 5.7: Simulated restoring torques and shift restoring forces when $\alpha = 180^\circ$. (a) Torque values normalized by surface tension and substrate area. (\blacksquare) $V = 4.9 \mu\text{L}$, $A = 25 \text{ mm}^2$, $H = 196 \mu\text{m}$. (\bullet) $V = 9.8 \mu\text{L}$, $A = 25 \text{ mm}^2$, $H = 392 \mu\text{m}$. (\bullet) $V = 9.8 \mu\text{L}$, $A = 50 \text{ mm}^2$, $H = 196 \mu\text{m}$. (\blacklozenge) $V = 4.9 \mu\text{L}$, Perimeter = 20 mm. Inset: rotation angle at $\alpha = 180^\circ$. The lines are meant to guide the eye. (b) Shift restoring forces. Data points represent Surface Evolver simulations while lines represent theoretical predictions. F_W and F_L are the restoring forces when the substrate is shifted normal to its width or length respectively. The inset shows the total translational force $F_{Trans} = F_W + F_L$ normalized by the surface tension and substrate perimeter (P).

The rotation angle at which a maximum pinning angle of 180° is first observed is not constant for all the trials. The inset in Figure 5.7a shows that bridges with larger equilibrium heights can be rotated more before α reaches 180° . Even in the cases where the equilibrium height was kept constant, the maximum rotation angle is not constant. This indicates that increasing the substrate area reduces the maximum rotation angles before depinning occurs. One method for exploring further the effect of substrate area and shape on restoring torques is to calculate the substrates projected area. Projected area is defined as the area of two identical substrates superimposed (bottom at $\phi = 0$, top at $\phi > 0$) subtracted and normalized by the area of a single substrate. Substrates with higher aspect ratios have higher projected areas for a given rotation angle, and thus have higher restoring torques (see Figure 5.8). This trend holds true not only for rectangular substrate shapes, but for normal crosses, and for the trivial case of circular shapes (data not shown). This simple observation based on the geometry of the substrates can be used as a computationally inexpensive tool for the design of self-alignment devices.

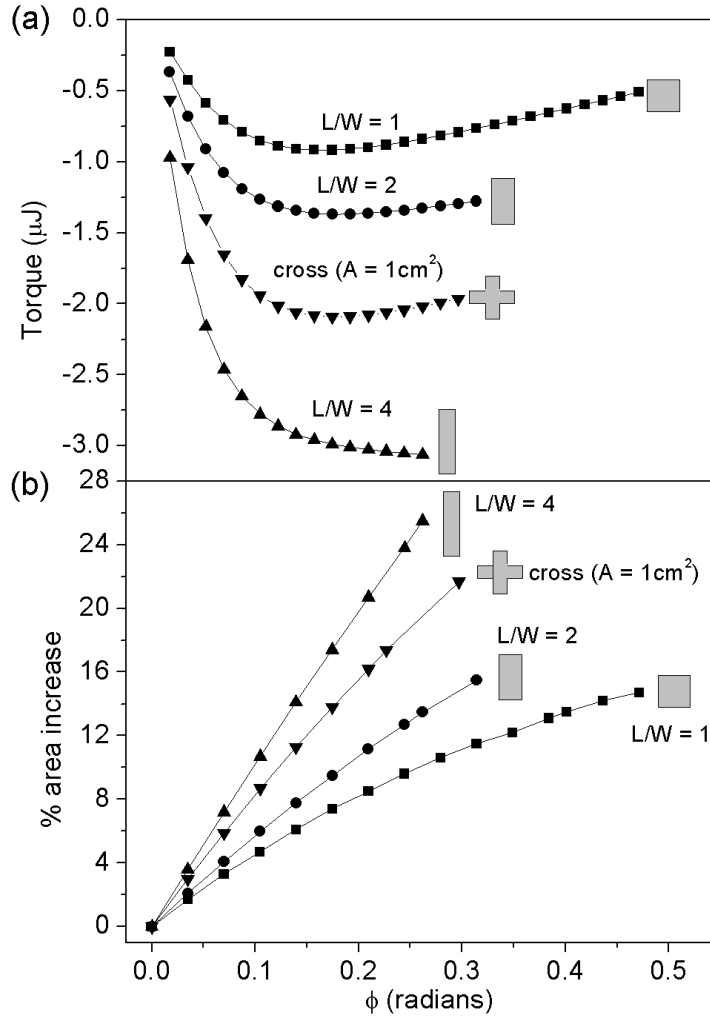


Figure 5.8: (a) Simulated restoring torque for substrates with area = 1 cm^2 , volume = $39\ \mu\text{L}$, and different shapes. (b) projected area increase of substrates with area = 1 cm^2 , and different shapes vs. rotation angle.

The simulations also allow us to investigate how shift restoring forces are affected by increasing the aspect ratio. In Figure 5.7b F_w and F_L are the restoring forces when the top substrate is perturbed laterally normal the width or the length, respectively. Data points correspond to Surface Evolver simulations while lines represent the equations $F_w =$

$2\gamma W$, and $F_L = 2\gamma L$. As predicted for square substrates, the shift restoring forces are directly proportional to the length of their respective sides.⁵⁵ The inset shows that the total translational force, $F_{\text{Trans}} = F_W + F_L$, is proportional to the perimeter of the substrate. Because holding the substrate area constant while increasing the aspect ratio requires the perimeter to increase (see above), an increase in aspect ratio leads to a larger F_{Trans} . The increase in both restoring torque and shift restoring force with higher aspect ratio show that self-alignment devices with higher aspect ratios will be more difficult to perturb away from their aligned configuration, leading to reduced chances of misalignment after initial bridge formation occurs¹²⁹.

Figure 5.9 compares the relative importance of the shift (F_{trans}) to rotational ($F_{\text{rot}} = \frac{2T}{L}$) restoring forces at $\alpha = 180^\circ$. The rotation forces are of the same order as the shift forces for all aspect ratios examined, but are near unity for $L/W > 4$. Since most perturbations to flip-chip devices result in a combination of rotational and lateral offsets¹¹⁸, having strong rotation forces are necessary to maintain good alignment. The sharp decrease in $F_{\text{trans}}/F_{\text{rot}}$ as L/W goes from 1 to 4, followed by a leveling off of the force ratio implies that larger aspect ratios (>6) are not necessary to achieve similar shift and rotation forces. Interestingly, substrate area, liquid volume, and equilibrium height do not seem to affect the relative importance of shift to rotational forces at moderate aspect ratios. For lower aspect ratios, larger substrate areas and smaller equilibrium heights lead to a lower ratio of shift to restoring forces. The inset in Figure 5.9 shows the ratio of shift to rotation forces when the maximum pinning angle is 150° . The rotational restoring forces also become more important as the aspect ratio increases (but also go through a

maximum at $L/W = 2$ for one trial). This indicates that rotational alignment forces might be even more important for small perturbations (yielding to lower maximum pinning angle) than when the substrate is close to its depinning limit. Regardless, Figure 5.9 shows that rotational alignment forces are comparable to shift alignment forces for both square and rectangular substrate shapes, and should not be neglected when studying chip alignment.

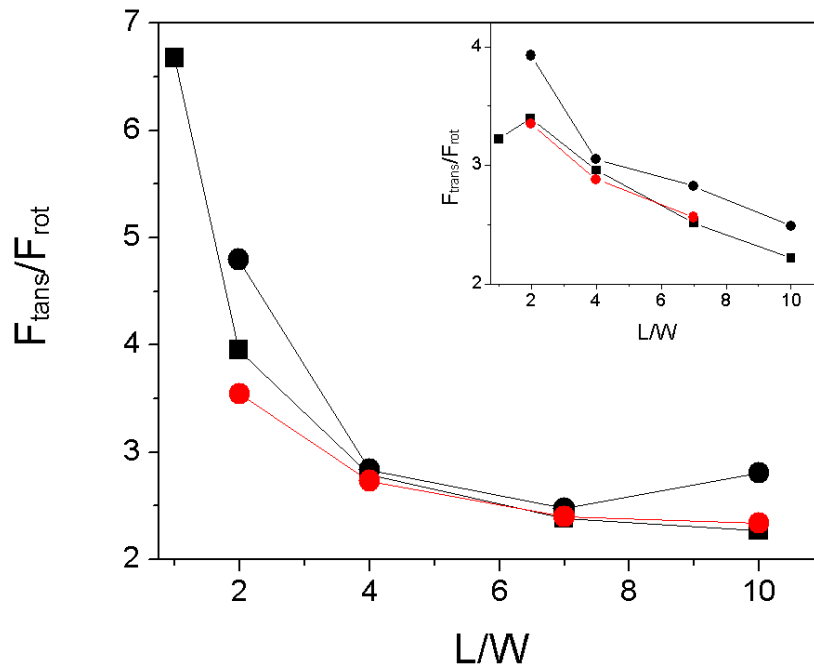


Figure 5.9: Translational force (F_{trans}) over rotational force (F_{rot}) for different volumes and areas at $\alpha = 180^\circ$. Data points represent Surface Evolver simulations while lines are meant to guide the eye. (▪) $V = 4.9 \mu\text{L}$, $A = 25 \text{ mm}^2$, $H = 196 \mu\text{m}$. (●) $V = 9.8 \mu\text{L}$, $A = 25 \text{ mm}^2$, $H = 392 \mu\text{m}$. (●) $V = 9.8 \mu\text{L}$, $A = 50 \text{ mm}^2$, $H = 196 \mu\text{m}$. Inset shows $F_{\text{trans}}/F_{\text{rot}}$ at $\alpha = 150^\circ$.

Lastly, we can predict the effect that increasing aspect ratio has on actual flip-chip self-alignment devices. The data points in Figure 5.10 represent the lateral restoring force as a function of the displacement of a flip-chip device fabricated by Josell et. al.⁸⁶ The lines in Figure 5.10 represent simulated shift restoring forces, but with rectangular pad shapes of different aspect ratios (holding liquid volume, substrate area, and surface tension constant to the ones in Ref. ⁸⁶). It is shown that by simply changing the substrate shape to a square, the restoring forces is improved considerably. This is likely due to the increased edge length perpendicular to the shift direction of the square substrate and the squares sharp corners¹²⁴ (see Figure 5.7). As the aspect ratio is increased, the restoring force normal to the length increases substantially over the circular pad shape. While the force normal to the width decreases with increasing aspect ratio (Figure 5.7b), the magnitude of F_w at $L/W = 4$ is still comparable to the shift restoring force of the circular pads. Aspect ratio is an ideal parameter for tuning restoring force, since improvements can be made while holding substrate area, liquid volume, and equilibrium height constant. One disadvantage of using rectangular substrate shapes however is a highly directionally dependent force profile. In the case of flip-chip alignment schemes, where multiple bridges and substrates are often used for alignment, the orientation of the substrates could be optimized to eliminate this directional dependence.

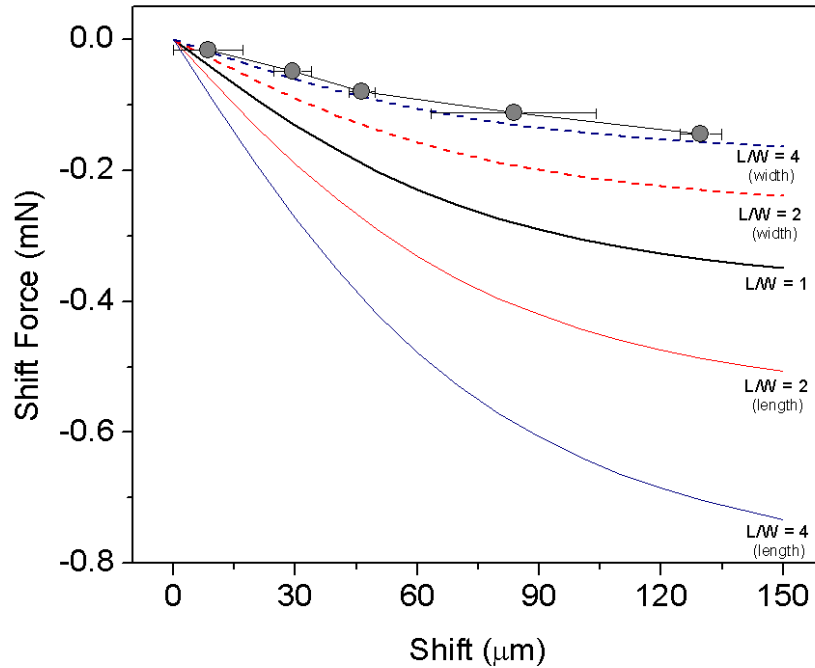


Figure 5.10: Experimental and simulated shift restoring forces for substrates with different aspect ratios. The data points correspond to the experimental data of Josell et. al.⁸⁶ for shift restoring force of circular pads with area = 0.32 mm^2 , liquid volume = $0.029 \text{ } \mu\text{L}$, and surface tension = 0.4 N/m . Black, red, and blue lines represent simulated shift forces for rectangular substrates with aspect ratio 1, 2, and 4 respectively while keeping the same area, liquid volume, and surface tension of the experimental points. Solid lines represent shift forces normal to the substrate's length, while dashed lines represent shift forces normal to substrate's width.

In summary, we performed simulations and experiments that explore the effect of substrate aspect ratio on the capillary interactions due to the presence of liquid bridges between misaligned rectangular substrates. Increasing aspect ratio, even while holding

substrate area and equilibrium height constant, was found to increase alignment forces and torques associated with lateral and rotational perturbations. A simple theoretical model based on the geometry of the substrates and the liquid-vapor surface tension for both the torques and restoring forces was presented that shows excellent agreement with the simulations. The effect of substrate perimeter, liquid volume, and substrate area were explored, and the increase in forces and torques was found to be directly related to an increase in aspect ratio. It was also found that rotational restoring forces are of the same order as the shift restoring forces, and therefore should not be neglected. Finally, simulations were run using input parameters from an experimental flip-chip system to show how aspect ratio can be used as a method to increase capillary-based restoring forces.

Conclusion

6.1. Concluding remarks

The goal of this thesis has been to explore the morphology and capillary forces of liquids confined to a slit pore geometry, and to investigate restoring forces of liquids bridged between misaligned high aspect ratio solid substrates. Experimental methods along with finite element simulations using the software package Surface Evolver were utilized to develop a better understanding of the often counterintuitive changes in morphology and forces when the geometry of the slit pore was varied. Analytic expressions for morphology, force, and torque were presented when possible to provide an understanding of the underlying mechanisms of the pinned capillary bridges in this work.

6.2. Impact and contributions

In chapter 3 we performed experiments and simulations to characterize the morphology and forces of liquid bridges confined within a slit pore of variable height. We found, somewhat counter intuitively, that the mean curvature of the liquid bridge changed sign from negative to positive (concave to convex pinning angle) when the ratio of pore height to width (H/W) was greater than one. This was significant, since previous

theoretical models in the literature that looked at similar systems in 2D predicted an opposite effect⁹¹. Additionally we showed that the presence of a finite wetting angle ($\theta > 0$) dramatically changed the morphology of the liquid bridge, preventing “anvil-like” long tailed bridges described in previous work⁹². The mean curvature of the bridge was also found to be independent of the liquid volume (as long as the liquid bridge did not reach the end of the strip), which is in agreement with the system previously explored of a liquid bridge between two cylinders⁹⁹. Lastly, we showed that while the mean curvature (and subsequently the Laplace pressure) changed sign when the height of the pore was increased, the force between the two plates always remained attractive.

In chapter 4 we presented a simple theory to predict the morphological evolution of a capillary bridge in a slit pore geometry based on three assumptions (translational invariance, the circle approximation, and an intuitive estimation of the radius of curvature based on the width of the strip). This theory is useful because it not only accurately predicts the mean curvature in the region where the sign change occurs, but frames the change as a competition between the wetting angle of the strip (θ) and the geometric confinement (H/W).

Chapter 5 used simulation and experiments to quantify the effect that substrate aspect ratio (L/W) has on capillary restoring forces and torques. We showed that increasing the aspect ratio (even when substrate area is held constant) led to both higher lateral restoring forces and torques when the substrates were perturbed away from their equilibrium state. A simple theoretical model was presented that accurately predicts shift restoring forces and rotational torques the liquid induces on the substrates. Importantly,

we show that the rotational restoring forces are of order the shift restoring forces and should not be neglected. Finally, simulation were run using parameters from an experimental flip-chip system found in the literature to demonstrate how aspect ratio could be used as a method for increasing capillary restoring forces.

6.3. Future direction

The slit pore as a model system is useful for extending the analysis of axisymmetric bridges to more arbitrary morphological profiles. Removing the constraint that the aspect ratio of the liquid bridge equals one, the system can be generalized to model more complex systems, such as "wallless" microfluidic channels¹⁶⁻¹⁸ or stiction between MEMs and atomic force microscopy components¹⁰⁻¹⁵. Conversely, the relatively simple geometry of a slit pore still allows for the use of assumptions (such as translational invariance in chapters 3 and 4) that can greatly simplify analysis. For the work done in this thesis, the liquid induced in the slit pore was a mixture of glycerol and water, and the geometry of the pore was varied slowly to eliminate dynamic effects. It would be worthwhile to explore how the morphology and capillary forces change when either the liquid medium (nonnewtonian fluids for example) or the speed at which the pore separation was varied. This would have direct applications in printing, where dispensing speed and liquid composition can vary dramatically.

Additionally, investigating further the effect that shape has on capillary restoring forces would be meaningful. Currently, an impressive body of (mainly simulated) work has been dedicated to predicting the restoring forces of laterally perturbed capillary bridges between substrates with more complex geometries (stars, polygons, etc.). These investigations would be complemented greatly by both measuring experimentally the forces they predict, as well as addressing rotational, and coupled (rotation and lateral) perturbations. The work of Takei et. al.⁸⁰ is an example of such an extension. In their work however torques are measured using powerful electromagnetic fields (using a SQUIDS device), which has the downside of requiring the substrates (and subsequently the liquid bridge not to be) magnetic. This constraint could prove difficult for biomimetic applications, or for electronic packaging where liquid mediums are often solder based. An experimental investigation of capillary restoring forces and torques that were not magnetic based would therefore be quite useful. This could be achieved by designing a cantileaver deflection based device similar to the work of Mastrangeli¹¹⁷ or through modification of a commercial unit such as the FemtoTools FT-FS1000. It would also be useful to further explore the concept presented in Figure 5.8 of per cent area overlap. Currently, a relationship between increasing area overlap and torque for circles, squares, rectangles, and crosses has been established, but a relation for more general geometries has not been explored. Establishing an expression for torque as a function of area increase would also prove valuable, as it would eliminate the need for time consuming computer simulations or the numerical solution of integrals.

References

1. Horton, R. E., The role of infiltration in the hydrologic cycle. *Transactions-American Geophysical Union* **1933**, *14*, 446-460.
2. Morrow, N. R., Wettability and its effect on oil-recovery. *J. Petrol. Tech.* **1990**, *42*, 1476-1484.
3. Hornbaker, D. J.; Albert, R.; Albert, I.; Barabasi, A. L.; Schiffer, P., What keeps sandcastles standing? *Nature* **1997**, *387*, 765-765.
4. Scheel, M.; Seemann, R.; Brinkmann, M.; Di Michiel, M.; Sheppard, A.; Breidenbach, B.; Herminghaus, S., Morphological clues to wet granular pile stability. *Nature Mater.* **2008**, *7*, 189-193.
5. Scheel, M.; Seemann, R.; Brinkmann, M.; Di Michiel, M.; Sheppard, A.; Herminghaus, S., Liquid distribution and cohesion in wet granular assemblies beyond the capillary bridge regime. *J. Phys.: Condens. Matter* **2008**, *20*, 1-7.
6. Rahbari, S. H. E.; Vollmer, J.; Herminghaus, S.; Brinkmann, M., Fluidization of wet granulates under shear. *Phys. Rev. E* **2010**, *82*, 061305-1 - 061305-9.
7. Prakash, M.; Quere, D.; Bush, J. W. M., Surface tension transport of prey by feeding shorebirds: The capillary ratchet. *Science* **2008**, *320*, 931-934.
8. Rubega, M. A., Surface tension prey transport in shorebirds: How widespread is it? *Ibis* **1997**, *139*, 488-493.
9. Bush, J. W. M.; Peaudecerf, F.; Prakash, M.; Quere, D., On a tweezer for droplets. *Adv. Colloid Interface Sci.* **2010**, *161*, 10-14.
10. Sedin, D. L.; Rowlen, K. L., Adhesion forces measured by atomic force microscopy in humid air. *Anal. Chem.* **2000**, *72*, 2183-2189.
11. van Spengen, W. M.; Puers, R.; De Wolf, I., A physical model to predict stiction in MEMS. *J. Micromech. Microeng.* **2002**, *12*, 702-713.
12. Maboudian, R.; Howe, R. T., Critical review: Adhesion in surface micromechanical structures. *J. Vac. Sci. Technol., B* **1997**, *15*, 1-20.
13. Chini, S. F.; Amirfazli, A., Understanding Pattern Collapse in Photolithography Process Due to Capillary Forces. *Langmuir* **2010**, *26*, 13707-13714.
14. Malotky, D. L.; Chaudhury, M. K., Investigation of capillary forces using atomic force microscopy. *Langmuir* **2001**, *17*, 7823-7829.

15. Weeks, B. L.; Vaughn, M. W.; DeYoreo, J. J., Direct imaging of meniscus formation in atomic force microscopy using environmental scanning electron microscopy. *Langmuir* **2005**, *21*, 8096-8098.
16. Greenwood, J. D.; Liu, Y.; Busacker, D. E.; Cheng, D.; Jiang, H., Collection of Gaseous and Aerosolized Samples Using Microfluidic Devices With Gas-Liquid Interfaces. *IEEE Sens. J.* **2010**, *10*, 952-959.
17. Zhao, B.; Moore, J. S.; Beebe, D. J., Principles of surface-directed liquid flow in microfluidic channels. *Anal. Chem.* **2002**, *74*, 4259-4268.
18. Zhao, B.; Viernes, N. O. L.; Moore, J. S.; Beebe, D. J., Control and applications of immiscible liquids in microchannels. *J. Am. Chem. Soc.* **2002**, *124*, 5284-5285.
19. Xiong, X. R.; Hanein, Y.; Wang, W. H.; Schwartz, D. T.; Bohringer, K. F., Multi-batch micro-selfassembly via controlled capillary forces. *IEEE/Rjs Proc. Int. Conf. Intel. Robo Syst* **2001**, 1335-1342.
20. Morris, C. J.; Parviz, B. A., Micro-scale metal contacts for capillary force-driven self-assembly. *J. Micromech. Microeng.* **2008**, *18*.
21. Srinivasan, U.; Liepmann, D.; Howe, R. T., Microstructure to substrate self-assembly using capillary forces. *J. Microelectromech. Syst.* **2001**, *10*, 17-24.
22. Gracias, D. H.; Boncheva, M.; Omoregie, O.; Whitesides, G. M., Biomimetic self-assembly of helical electrical circuits using orthogonal capillary interactions. *Appl. Phys. Lett.* **2002**, *80*, 2802-2804.
23. Gracias, D. H.; Tien, J.; Breen, T. L.; Hsu, C.; Whitesides, G. M., Forming electrical networks in three dimensions by self-assembly. *Science* **2000**, *289*, 1170-1172.
24. Breen, T. L.; Tien, J.; Oliver, S. R. J.; Hadzic, T.; Whitesides, G. M., Design and self-assembly of open, regular, 3D mesostructures. *Science* **1999**, *284*, 948-951.
25. Terfort, A.; Bowden, N.; Whitesides, G. M., Three-dimensional self-assembly of millimetre-scale components. *Nature* **1997**, *386*, 162-164.
26. de Boer, P. C. T.; de Boer, M. P., Rupture work of pendular bridges. *Langmuir* **2008**, *24*, 160-169.
27. Mayer, R. P.; Stowe, R. A., Nodoids and toroids: comparison of two geometries for the meniscus profile of a wetting liquid between two touching isolated spheres and extensions to the model of a collection of packed spheres. *J. Colloid Interface Sci.* **2005**, *285*, 781-788.

28. Orr, F. M.; Scriven, L. E.; Rivas, A. P., Pendular rings between solids - meniscus properties and capillary force. *J. Fluid Mech.* **1975**, *67*, 723-742.
29. Rose, W., Volumes and surface areas of pendular rings. *J. Appl. Phys.* **1958**, *29*, 687-691.
30. De Souza, E. J.; Gao, L. C.; McCarthy, T. J.; Arzt, E.; Crosby, A. J., Effect of contact angle hysteresis on the measurement of capillary forces. *Langmuir* **2008**, *24*, 1391-1396.
31. Dodds, S.; Carvalho, M.; Kumar, S., Stretching liquid bridges with moving contact lines: The role of inertia. *Phys. Fluids* **2011**, *23*.
32. Erle, M. A.; Dyson, D. C.; Morrow, N. R., Liquid bridges between cylinders, in a torus, and between spheres *Aiche Journal* **1971**, *17*, 115-121.
33. Goegelein, C.; Brinkmann, M.; Schroeter, M.; Herminghaus, S., Controlling the Formation of Capillary Bridges in Binary Liquid Mixtures. *Langmuir* **2010**, *26*, 17184-17189.
34. Lambert, P.; Chau, A.; Delchambre, A.; Regnier, S., Comparison between two capillary forces models. *Langmuir* **2008**, *24*, 3157-3163.
35. Mason, G.; Clark, W. C., Liquid Bridges Between Spheres. *Chem. Eng. Sci.* **1965**, *20*, 859-866.
36. De Souza, E. J.; Brinkmann, M.; Mohrdieck, C.; Arzt, E., Enhancement of capillary forces by multiple liquid bridges. *Langmuir* **2008**, *24*, 8813-8820.
37. Peng, Y. F.; Li, G. X., An elastic adhesion model for contacting cylinder and perfectly wetted plane in the presence of meniscus. *J. Tribol.-T. ASME* **2007**, *129*, 231-234.
38. van Honschoten, J. W.; Tas, N. R.; Elwenspoek, M., The profile of a capillary liquid bridge between solid surfaces. *Am. J. Phys.* **2010**, *78*, 277-286.
39. Brinkmann, M.; Blossey, R.; Arscott, S.; Druon, C.; Tabourier, P.; Le Gac, S.; Rolando, C., Microfluidic design rules for capillary slot-based electrospray sources. *Appl. Phys. Lett.* **2004**, *85*, 2140-2142.
40. Fan, C.; Do, D.; Nicholson, D., On the cavitation and pore blocking in slit-shaped ink-bottle pores. *Langmuir* **2011**, *27*, 3511-3526.
41. Palmer, J. C.; Moore, J. D.; Brennan, J. K.; Gubbins, K. E., Simulating local adsorption isotherms in structurally complex porous materials: A direct assessment of the slit pore model. *J. Phys. Chem. Lett.* **2011**, *2*, 165-169.

42. Talanquer, V.; Oxtoby, D., Nucleation in a slit pore. *J. Chem. Phys.* **2001**, *114*, 2793.
43. Evans, R.; Marconi, U. M. B.; Tarazona, P., Capillary condensation and adsorption in cylindrical and slit-like pores. *J. Chem. Soc., Faraday Trans. 2* **1986**, *82*, 1763-1787.
44. Schoen, M.; Diestler, D.; Cushman, J., Fluids in micropores. I. Structure of a simple classical fluid in a slit-pore. *J. Chem. Phys.* **1987**, *87*, 5464.
45. Mastrangeli, M.; Ruythooren, W.; Celis, J. P.; Van Hoof, C., Challenges for Capillary Self-Assembly of Microsystems. *IEEE T. Compon. Pack* **2011**, *1*, 133-149.
46. Saeedi, E.; Abbasi, S.; Bohringer, K.; Parviz, A., Molten-Alloy Driven Self-assembly for Nano and Micro Scale System Integration. *Fluid. Dyn. Mater. Process.* **2006**, *2*, 221-245.
47. Tu, K. N., Recent advances on electromigration in very-large-scale-integration of interconnects. *J. Appl. Phys.* **2003**, *94*, 5451-5473.
48. Zeng, K.; Tu, K. N., Six cases of reliability study of Pb-free solder joints in electronic packaging technology. *Mater. Sci. Eng. R-* **2002**, *38*, 55-105.
49. Wierer, J. J.; Steigerwald, D. A.; Krames, M. R.; O'Shea, J. J.; Ludowise, M. J.; Christenson, G.; Shen, Y. C.; Lowery, C.; Martin, P. S.; Subramanya, S.; Gotz, W.; Gardner, N. F.; Kern, R. S.; Stockman, S. A., High-power AlGaInN flip-chip light-emitting diodes. *Appl. Phys. Lett.* **2001**, *78*, 3379-3381.
50. Yeh, E. C. C.; Choi, W. J.; Tu, K. N.; Elenius, P.; Balkan, H., Current-crowding-induced electromigration failure in flip chip solder joints. *Appl. Phys. Lett.* **2002**, *80*, 580-582.
51. Shchekin, O. B.; Epler, J. E.; Trottier, T. A.; Margalith, T.; Steigerwald, D. A.; Holcomb, M. O.; Martin, P. S.; Krames, M. R., High performance thin-film flip-chip InGaN-GaN light-emitting diodes. *Appl. Phys. Lett.* **2006**, *89*.
52. Broesch, D. J.; Frechette, J., From Concave to Convex: Capillary Bridges in Slit Pore Geometry. *Langmuir* **2012**, *28*, 15548-15554.
53. Broesch, D. J.; Dutka, F.; Frechette, J., Curvature of Capillary Bridges as a Competition between Wetting and Confinement. *Langmuir* **2013**, *29*, 15558-15564.
54. Broesch, D. J.; Frechette, J., Fabrication and visualization of capillary bridges in slit pore geometry. *J. Vis. Exp.* **2014**, *83*, e51143.

55. Berthier, J.; Brakke, K.; Grossi, F.; Sanchez, L.; Di Cioccio, L., Self-alignment of silicon chips on wafers: A capillary approach. *J. Appl. Phys.* **2010**, *108*, 054905-1 - 054905-10.
56. de Gennes, P.-G.; Brochard-Wyart, F.; Quere, D., *Capillarity and Wetting Phenomena*. Springer: New York, 2004.
57. Bain, C. D.; Troughton, E. B.; Tao, Y. T.; Evall, J.; Whitesides, G. M.; Nuzzo, R. G., Formation of monolayer films by the spontaneous assembly of organic thiols from solution onto gold. *J. Am. Chem. Soc.* **1989**, *111*, 321-335.
58. Olivier, G. K.; Shin, D.; Gilbert, J. B.; Monzon, L. A. A.; Frechette, J., Supramolecular Ion-Pair Interactions To Control Monolayer Assembly. *Langmuir* **2009**, *25*, 2159-2165.
59. Brakke, K., The Surface Evolver. *Exper. Math.* **1992**, *1*, 141-165.
60. Brakke, K. The Surface Evolver Webpage.
<http://www.susqu.edu/brakke/evolver/evolver.html>.
61. Washburn, E. W., The dynamics of capillary flow. *Phys. Rev.* **1921**, *17*, 273-283.
62. Davis, A. M. J.; Frenkel, A. L., Cylindrical liquid bridges squeezed between parallel plates - exact Stokes-flow solutions and hydrodynamic - forces *Phys. Fluids A, -Fluid Dyn.* **1992**, *4*, 1105-1109.
63. Dodds, S.; Carvalho, M. d. S.; Kumar, S., Stretching and slipping of liquid bridges near plates and cavities. *Phys. Fluids* **2009**, *21*, 092103-1 - 092103-15.
64. Eggers, J., Nonlinear dynamics and breakup of free-surface flows. *Rev. Mod. Phys.* **1997**, *69*, 865-929.
65. Huang, W.-X.; Lee, S.-H.; Sung, H. J.; Lee, T.-M.; Kim, D.-S., Simulation of liquid transfer between separating walls for modeling micro-gravure-offset printing. *Int. J. Heat Fluid Fl.* **2008**, *29*, 1436-1446.
66. Wiklund, H. S.; Uesaka, T., Simulations of shearing of capillary bridges. *Journal of Chemical Physics* **2012**, *136*, 094703-4-1 - 092103-9.
67. Leong, T. G.; Lester, P. A.; Koh, T. L.; Call, E. K.; Gracias, D. H., Surface tension-driven self-folding polyhedra. *Langmuir* **2007**, *23*, 8747-8751.
68. Whitesides, G. M.; Boncheva, M., Beyond molecules: Self-assembly of mesoscopic and macroscopic components. *Proc. Natl. Acad. Sci. USA* **2002**, *99*, 4769-4774.

69. Syms, R. R. A.; Yeatman, E. M.; Bright, V. M.; Whitesides, G. M., Surface tension-powered self-assembly of micro structures - The state-of-the-art. *J. Microelectromech. Syst.* **2003**, *12*, 387-417.
70. Kim, J. M.; Yasuda, K.; Fujimoto, K., Resin self-alignment processes for self-assembly systems. *J. Electron. Packaging* **2005**, *127*, 18-24.
71. Botto, L.; Yao, L.; Leheny, R. L.; Stebe, K. J., Capillary bond between rod-like particles and the micromechanics of particle-laden interfaces. *Soft Matter* **2012**, *8*, 4971-4979.
72. Lewandowski, E. P.; Cavallaro, M., Jr.; Botto, L.; Bernate, J. C.; Garbin, V.; Stebe, K. J., Orientation and Self-Assembly of Cylindrical Particles by Anisotropic Capillary Interactions. *Langmuir* **2010**, *26*, 15142-15154.
73. Cheung, E.; Sitti, M., Adhesion of biologically inspired oil-coated polymer micropillars. *J. Adhes. Sci. Technol.* **2008**, *22*, 569-589.
74. Vogel, M. J.; Steen, P. H., Capillarity-based switchable adhesion. *Proc. Natl. Acad. Sci. USA* **2010**, *107*, 3377-3381.
75. Obata, K. J.; Motokado, T.; Saito, S.; Takahashi, K., A scheme for micro-manipulation based on capillary force. *J. Fluid Mech.* **2004**, *498*, 113-121.
76. Dodds, S.; Carvalho, M. S.; Kumar, S., Stretching Liquid Bridges with Bubbles: The Effect of Air Bubbles on Liquid Transfer. *Langmuir* **2011**, *27*, 1556-1559.
77. Su, Y.; Ji, B.; Huang, Y.; Hwang, K., Effects of contact shape on biological wet adhesion. *J. Mater. Sci.* **2007**, *42*, 8885-8893.
78. De Souza, E. J.; Brinkmann, M.; Mohrdieck, C.; Crosby, A.; Arzt, E., Capillary forces between chemically different substrates. *Langmuir* **2008**, *24*, 10161-10168.
79. Kusumaatmaja, H.; Lipowsky, R., Equilibrium Morphologies and Effective Spring Constants of Capillary Bridges. *Langmuir* **2010**, *26*, 18734-18741.
80. Takei, A.; Matsumoto, K.; Shimoyama, I., Capillary Torque Caused by a Liquid Droplet Sandwiched between Two Plates. *Langmuir* **2010**, *26*, 2497-2504.
81. Gillette, R. D.; Dyson, D. C., Stability of fluid Interfaces of revolution between equal solid circular plates. *Chem. Eng.* **1971**, *2*, 44-54.
82. Gillette, R. D.; Dyson, D. C., Stability of axisymmetric liquid-fluid interfaces towards general disturbances. *Chem. Eng. J.* **1972**, *3*, 196-199.

83. Padday, J. F.; Petre, G.; Rusu, C. G.; Gamero, J.; Wozniak, G., The shape, stability and breakage of pendant liquid bridges. *J. Fluid Mech.* **1997**, *352*, 177-204.
84. Zhang, X.; Padgett, R. S.; Basaran, O. A., Nonlinear deformation and breakup of stretching liquid bridges. *J. Fluid Mech.* **1996**, *329*, 207-245.
85. Fennell, B.; Lee, S.; Baldwin, D. F., Translation Solder Self-Alignment Mechanics Modeling for a Flip Chip in the Presence of a Viscous Fluid. *J. Electron. Packaging* **2010**, *132*, 041013-1 - 041013-6.
86. Josell, D.; Wallace, W. E.; Warren, J. A.; Wheeler, D.; Powell, A. C., Misaligned flip-chip solder joints: Prediction and experimental determination of force-displacement curves. *J. Electron. Packaging* **2002**, *124*, 227-233.
87. Lin, W.; Patra, S. K.; Lee, Y. C., Design of Solder Joints for Self-Aligned Optoelectronic Assemblies. *IEEE T. Compon. Pack B* **1995**, *18*, 543-551.
88. Patra, S. K.; Lee, Y. C.; Ieee, Modeling of Self-Alignment Mechanism in Flip-Chip Soldering .2. Multichip Solder Joints. *1991 proc.: 41st Elec. comp. Tech. con.* **1991**, 783-788.
89. Yannou, J.-M.; Zinck, C. *Flip-Chip: technologies, application market report*; Yole Developpement: 2011; pp 1-307.
90. Yost, B.; McGroarty, J.; Borgesen, P.; Li, C. Y., Shape of a Nonaxisymmetric Liquid Solder Drop Constrained by Parallel Plates *IEEE T. Compon. Hybr.* **1993**, *16*, 523-526.
91. Swain, P. S.; Lipowsky, R., Wetting between structured surfaces: Liquid bridges and induced forces. *Europhys. Lett.* **2000**, *49*, 203-209.
92. Valencia, A.; Brinkmann, M.; Lipowsky, R., Liquid bridges in chemically structured slit pores. *Langmuir* **2001**, *17*, 3390-3399.
93. Bucior, K.; Yelash, L.; Binder, K., Molecular-dynamics simulation of evaporation processes of fluid bridges confined in slitlike pores. *Phys. Rev. E* **2009**, *79*, 031604-1 - 031604-12.
94. Yaneva, J.; Milchev, A.; Binder, K., Polymer droplets on substrates with striped surface domains: molecular dynamics simulations of equilibrium structure and liquid bridge rupture. *J. Phys.: Condens. Matter* **2005**, *17*, S4199-S4211.
95. Schoen, M., Fluid bridges confined between chemically nanopatterned solid substrates. *Phys. Chem. Chem. Phys.* **2008**, *10*, 223-256.

96. Duffy, D. C.; McDonald, J. C.; Schueller, O. J. A.; Whitesides, G. M., Rapid prototyping of microfluidic systems in poly(dimethylsiloxane). *Anal. Chem.* **1998**, *70*, 4974-4984.
97. Childs, W. R.; Nuzzo, R. G., Large-area patterning of coinage-metal thin films using decal transfer lithography. *Langmuir* **2005**, *21*, 195-202.
98. Lee, J. N.; Park, C.; Whitesides, G. M., Solvent compatibility of poly(dimethylsiloxane)-based microfluidic devices. *Anal. Chem.* **2003**, *75*, 6544-6554.
99. Princen, H. M., Capillary Phenomena in Assemblies of Parallel Cylinders .3. Liquid Columns Between Horizontal Parallel Cylinders. *J. Colloid Interface Sci.* **1970**, *34*, 171-184.
100. Dodds, S.; Carvalho, M.; Kumar, S., The dynamics of three-dimensional liquid bridges with pinned and moving contact lines. *J. Fluid Mech., in press*.
101. Tuller, M.; Or, D.; Dudley, L. M., Adsorption and capillary condensation in porous media: Liquid retention and interfacial configurations in angular pores. *Water Resour. Res.* **1999**, *35*, 1949-1964.
102. Rejmer, K.; Dietrich, S.; Napiórkowski, M., Filling transition for a wedge. *Phys. Rev. E* **1999**, *60*, 4027.
103. Jakubczyk, P.; Napiórkowski, M., Adsorption in a nonsymmetric wedge. *Phys. Rev. E* **2002**, *66*, 041107.
104. Pepin, X.; Rossetti, D.; Iveson, S. M.; Simons, S. J. R., Modeling the Evolution and Rupture of Pendular Liquid Bridges in the Presence of Large Wetting Hysteresis. *J. Colloid Interface Sci.* **2000**, *232*, 289-297.
105. Hotta, K.; Takeda, K.; Iinoya, K., The capillary binding force of a liquid bridge. *Powder Technol.* **1974**, *10*, 231-242.
106. Clark, W. C.; Haynes, J. M.; Mason, G., Liquid Bridges Between a Sphere and a Plane. *Chem. Eng. Sci.* **1968**, *23*, 810-&.
107. Megias-Alguacil, D.; Gauckler, L. J., Accuracy of the toroidal approximation for the calculus of concave and convex liquid bridges between particles. *Granul. Matter* **2011**, *13*, 487-492.
108. Willett, C. D.; Adams, M. J.; Johnson, S. A.; Seville, J. P. K., Capillary bridges between two spherical bodies. *Langmuir* **2000**, *16*, 9396-9405.
109. Mehrotra, V. P.; Sastry, K. V. S., Pendular Bond Strength Between Unequal-Sized Spherical-Particles. *Powder Technol.* **1980**, *25*, 203-214.

110. Marmur, A., Tip Surface Capillary Interactions. *Langmuir* **1993**, *9*, 1922-1926.
111. Popescu, M. N.; Oshanin, G.; Dietrich, S.; Cazabat, A. M., Precursor films in wetting phenomena. *J. Phys.: Condens. Matter* **2012**, *24*.
112. Bohringer, K. F.; Srinivasan, U.; Howe, R. T., Modeling of capillary forces and binding sites for fluidic self-assembly. *IEEE Int. Conf. Micro Electro Mech. Syst.* **2001**, 369-374.
113. Xiong, X. R.; Liang, S. H.; Bohinger, K. F., Geometric binding site design for surface-tension driven self-assembly. *IEEE Proc. Int. Conf. Robo. Auto.* **2004**, 1141-1148.
114. Zheng, W.; Jacobs, H. O., Shape-and-solder-directed self-assembly to package semiconductor device segments. *Appl. Phys. Lett.* **2004**, *85*, 3635-3637.
115. Kong, M.; Jeon, S.; Au, H.; Hwang, C.; Lee, Y.-C., Development and Experimental Validation of a 3-D Solder Self-Alignment Model for Alignment Accuracy Prediction of Flip-Chip Assembly. *IEEE T. Compon. Pack* **2011**, *1*, 1523-1532.
116. Shah, A.; Chang, B.; Suihkonen, S.; Zhou, Q.; Lipsanen, H., Surface-Tension-Driven Self-Alignment of Microchips on Black-Silicon-Based Hybrid Template in Ambient Air. *J. Microelectromech. Syst.* **2013**, *22*, 739-746.
117. Mastrangeli, M.; Valsamis, J. B.; Van Hoof, C.; Celis, J. P.; Lambert, P., Lateral capillary forces of cylindrical fluid menisci: a comprehensive quasi-static study. *J. Micromech. Microeng.* **2010**, *20*.
118. Gao, S.; Zhou, Y., Self-alignment of micro-parts using capillary interaction: Unified modeling and misalignment analysis. *Microelectron. Reliab.* **2013**, *53*, 1137-1148.
119. Berthier, J.; Brakke, K.; Mermoz, S.; sanchez, L.; fretigny, C.; Di Cioccio, L., Self-alignment of Silicon Chips on Wafers: a Numerical Investigation of the Effect of Spreading and Wetting. *Sens. Trans.* **2001**, *13*, 44-52.
120. Tsai, C. G.; Hsieh, C. M.; Yeh, J. A., Self-alignment of microchips using surface tension and solid edge. *Sensor Actuat. A-Phys.* **2007**, *139*, 343-349.
121. Berthier, J.; Mermoz, S.; Brakke, K.; Sanchez, L.; Fretigny, C.; Di Cioccio, L., Capillary self-alignment of polygonal chips: a generalization for the shift-restoring force. *Microfluid. Nanofluid.* **2013**, *14*, 845-858.
122. Arutinov, G.; Smits, E. C. P.; Mastrangeli, M.; van Heck, G.; van den Brand, J.; Schoo, H. F. M.; Dietzel, A., Capillary self-alignment of mesoscopic foil components for sensor-systems-in-foil. *J. Micromech. Microeng.* **2012**, *22*.

123. Deering, S. E.; Szekely, J., Mathematical-Modeling of Alternative Pad Designs In Flip-Chip Soldering Processes. *J. Electron. Mater.* **1994**, *23*, 1325-1334.
124. Ahn, D. H.; Lee, J.; Yoo, C. D.; Kim, Y. S., Influence of pad shape on self-alignment in electronic packaging. *J. Electron. Mater.* **2006**, *35*, 411-415.
125. Wang, D.-A.; Liao, B., Shaking assisted self-assembly of rectangular-shaped parts. *J. Mater. Process. Technol.* **2010**, *210*, 343-350.
126. Wang, D.-A.; Ko, H.-H., Magnetic-assisted self-assembly of rectangular-shaped parts. *Sensor Actuat. A-Phys.* **2009**, *151*, 195-202.
127. Lin, C.; Tseng, F.; Kan, H.-C.; Chieng, C.-C., Numerical studies on micropart self-alignment using surface tension forces. *Microfluid. Nanofluid.* **2009**, *6*, 63-75.
128. Ding, Y.; Hong, L.; Nie, B.; Lam, K. S.; Pan, T., Capillary-driven automatic packaging. *Lab Chip* **2011**, *11*, 1464-1469.
129. Kaiji, S.; Ito, K.; Hata, S.; Shimokohbe, A., Self-alignment of microparts using liquid surface tension - behavior of micropart and alignment characteristics (vol 27, pg 42, 2003). *Precis. Eng.* **2003**, *27*, 444-444.
130. Virozub, A.; Haimovich, N.; Brandon, S., Three-Dimensional Simulations of Liquid Bridges between Two Cylinders: Forces, Energies, and Torques. *Langmuir* **2009**, *25*, 12837-12842.
131. Bedarkar, A.; Wu, X.-F., Capillary torque in a liquid bridge between two angled filaments. *J. Appl. Phys.* **2009**, *106*.
132. Lambert, P.; Mastrangeli, M.; Valsamis, J. B.; Degrez, G., Spectral analysis and experimental study of lateral capillary dynamics for flip-chip applications. *Microfluid. Nanofluid.* **2010**, *9*, 797-807.
133. Ferraro, D.; Semprebon, C.; Toth, T.; Locatelli, E.; Pierno, M.; Mistura, G.; Brinkmann, M., Morphological Transitions of Droplets Wetting Rectangular Domains. *Langmuir* **2012**, *28*, 13919-13923.

Fabrication and visualization of capillary bridges in slit pore geometry

[This appendix is reprinted (with minor modifications) with permission from: Broesch, D. J., Frechette, J. Fabrication and Visualization of Capillary Bridges in Slit Pore Geometry. *J. Vis. Exp.* (83), e51143, doi:10.3791/51143 (2014).]

A.1 Introduction

The study of the shape and resulting forces caused by capillary bridges has been the subject of extensive studies^{28-29, 32, 34-36}. Initially most efforts were focused, due to their simplicity, on axisymmetric capillary bridges. Often capillary bridges occurring in natural systems, such as those found in granular and porous media³⁻⁴, and bridges employed in technological applications, such as for capillary self-assembly in flip chip technologies^{45, 86-87, 117, 121, 132} are asymmetric with non-uniform wetting properties on the interacting surfaces. The combination of improved lithography techniques along with the accessibility of simple numerical tools to model fluid interfaces allows for the creation and modeling of capillary bridges with increasing complexity.

Capillary bridges in slit-pore geometry offer an interesting compromise: the directional wetting properties lead to non-axisymmetric bridges that retain some

symmetry planes (which simplifies the analysis). They have been studied theoretically and numerically as a case study for porous media. Systematic experimental studies of capillary bridges in slit-pore geometry have, however, been limited. Here we present a method to create and characterize capillary bridges in slit pore geometry. Briefly, the method consists of 1) the fabrication of pillars to create a chemical and physical heterogeneity, 2) the design of a microstage to align and manipulate the bridges, and 3) the imaging of the capillary bridges either from the front or the sides to characterize their morphology. The characterization of the bridge morphology, along with comparisons to Surface Evolver simulations are provided in a separate publication⁵². The protocol text is broken up into three main sections: 1) the fabrication of the PDMS (polydimethylsiloxane) pillars, 2) the functionalization of the tops of the pillars, and 3) the formation and characterization of the capillary bridges.

A.2 Protocol

A.2.1. Fabrication of the PDMS pillars

This section details the fabrication of the PDMS pillars using die casting with a silicon/SU-8 mold.

1.1. Fabrication of silicon/SU-8 mold

1.1.1. Place a clean 4 inch silicon wafer in a Pyrex Petri dish.

1.1.2. Prepare a 4:1 (by volume) sulfuric acid to hydrogen peroxide (piranha) solution in a separate beaker.

Note: Extreme caution is needed in the preparation and use of the piranha solution. The reaction is highly exothermic and insulated gloves will be required to handle beakers. Piranha reacts violently with organics. Let piranha solution cool to room temperature before disposing. Only prepare enough solution required to submerge the wafer in the dish.

1.1.3. Pour piranha solution slowly onto the silicon wafer until it is completely submerged. Let sit for 15 min.

1.1.4. Remove the wafer from the Petri dish and rinse under a stream of: deionized (DI) water for 2 min, ethanol for 30 seconds, acetone for 30 seconds, then blow dry with nitrogen.

Note: If residues from acetone are a problem, an additional rinse with IPA is recommended

1.1.5. Dry the wafer on a hot plate at 150° C for 15 min.

1.1.6. Remove from hot plate and let cool to room temperature.

1.1.7. Spin coat SU-8 2002 onto the surface of the wafer for 40 seconds at 500 RPM.

1.1.8. Spin coat SU-8 2050 onto the wafer with a two-step spin coater program. Step 1: 40 seconds at 500 RPM. Step 2: 1 min at 1500 RPM.

1.1.9. Remove the wafer from the spin coater and place on a preheated hotplate (65° C) for 10 min.

1.1.10. Let cool to room temperature, then place mask over wafer.

1.1.11. Place under ultraviolet lamp and expose for 30 seconds at 200 watts.

1.1.12. Remove mask and place the wafer on a preheated hotplate (95° C) for 10 min.

1.1.13. Place in SU-8 Developer solution and lightly agitate until all unexposed SU-8 has been removed. Then rinse in a stream of isopropyl alcohol for 30 seconds, blow dry with nitrogen.

1.1.14. Place on a preheated hotplate (95° C) for 30 min for a final hardbake.

1.2. Die casting of PDMS pillars

1.2.1. Mix vigorously a 10:1 mass ratio of PDMS sylgard-184 base to curing agent in beaker.

1.2.2. Degas PDMS in a vacuum chamber until all bubbles are gone.

1.2.3. Place the mold fabricated in section 1.1 in a large 4 inch plastic weighing dish and pour the PDMS.

1.2.4. Place dish with PDMS and mold back into vacuum chamber. Degas again until all bubbles are gone.

1.2.5. Place entire dish in an oven (preheated to 75 °C) for at least 2 hours. Then let cool to room temperature.

1.2.6. Cut away the dish from the PDMS, and the PDMS from the silicon wafer with a straight razor blade.

1.2.7. Cut out PDMS region with the pillars from the bulk and store in a clean Petri dish.

A.2.2. Functionalization of the tops of the pillars

This three-step process involves first the evaporation of a gold film on a silicon wafer, followed by imprint transfer lithography⁹⁷ of the gold film onto the PDMS pillars

(fabricated in section 1), and lastly the functionalization of the gold film with a self-assembled monolayer to render it hydrophilic.

2.1. Fabrication of gold on silicon wafers for imprint transfer lithography

2.1.1. Use a glass cutter to dice a 4 inch circular silicon wafer into 4 equally sized pieces.

Note: Wafers can be cleaned using steps 1.1.2-1.1.4 and reused.

2.1.2. Evaporate 20 nm of gold directly onto the silicon wafer.

2.1.3. Leave the wafer in evaporation chamber (or in a desiccator) until section 3 below is complete. This will keep the wafer as clean as possible.

2.1.4. Prepare an 8 μ L:20mL, (3-Mercaptopropyl)-trimethoxysilane (MPTS) : toluene solution in a clean glass vial.

2.1.5. Prepare 200 ml of 16 mM hydrochloric acid (HCl) in a clean beaker.

2.1.6. Put the wafer with gold film into the plasma reactor.

2.1.7. Clean the wafer using oxygen plasma at a pressure of 300 mTorr, power of 50 watts for 10 min.

Note: For this procedure a home-built plasma reactor was used.

2.1.8. Put the wafer in a Pyrex Petri dish full of 200 proof ethanol for at least 10 min.

Note: This step is done to remove any unstable oxides that form on the gold due to the oxygen plasma.

2.1.9. Rinse the wafer with ethanol, then blow dry with nitrogen.

2.1.10. Spin coat the MPTS solution onto the wafer at 500 RPM for 30 seconds followed by 2750 RPM for 1 min.

Note: MPTS is used as an adhesion layer between the PDMS and Au layer⁹⁷.

2.1.11. Take the wafer off of the spin coater and rinse under a stream of ethanol. Then, rinse with DI water and blow dry with nitrogen.

Note: Rinse gently to avoid peeling of the gold layer from the silicon wafer.

2.1.12. Place the wafer into a Pyrex Petri dish that contains enough 16 mM HCl solution to fully submerge the wafer. Leave in HCl for at least 5 min.

Note: Place into the solution gently to prevent the gold from peeling off.

Note: This is done to improve the adhesion between the PDMS and Au layer⁹⁷.

2.1.13. Remove the wafer from the HCl solution and blow dry with nitrogen.

Note: Wafers should be used no more than 15-20 min after this step is complete.

2.2. Imprint transfer lithography of the gold from wafer to PDMS pillars

2.2.1. Prepare one 25 x 75 mm glass slide for each PDMS sample by rinsing it with ethanol, DI water, and blow dry with nitrogen.

2.2.2. Place PDMS pillars into plasma chamber and perform oxygen plasma at a pressure of 300 mTorr and power of 50 watts for 30 seconds.

Note: Overexposure of the PDMS to the oxygen plasma will cause cracking. Adjust the plasma conditions accordingly.

2.2.3. Bind the back of the PDMS substrates to the clean glass slides by applying light pressure to them. The glass slide facilitates the manipulations of the PDMS pillars and mounting on the device described in Step 3.

2.2.4. Flip the glass-backed PDMS substrates and press the pillars down onto the MPTS-functionalized gold films (Step 2.1). Apply moderate pressure initially, and then put a weight (approximately 100 grams) on the glass slide to ensure conformal contact.

2.2.5. Leave the substrate in contact with the silicon wafer for at least 12 hours.

2.2.6. Separate the PDMS substrate from the wafer. If the PDMS substrate is stuck, use a straight razor blade to carefully pry an edge of the PDMS off of the wafer.

2.2.7. At this point a uniform gold film should be present on the top of the PDMS pillars. Use an optical microscope to verify that the gold film is not cracked or that there are no parts missing along the pillar.

2.3. Functionalization of the gold on the top of the PDMS pillars

2.3.1. Prepare enough 1mM mercaptohexadecanoic acid (MHA) in dimethyl sulfoxide (DMSO) to submerge fully the gold on top of the PDMS pillars.

Note: DMSO is used for its low PDMS swelling factor⁹⁸.

2.3.2. Place the PDMS substrates in the MHA solution and keep them there for at least 24 hours.

2.3.3. Remove the substrate from the MHA solution and rinse with DI water, then blow dry with nitrogen.

2.3.4. Place in vacuum chamber (pressure < 100 mTorr at 25 °C) for at least 12 hours.

Note: To verify that the functionalization process was successful, step 2 can be performed on a bulk piece of PDMS (without pillars) and the wetting angle can be tested in a goniometer. The MHA gold films should have advancing and receding water contact angles of <15° and ~0°, respectively.⁵⁸

A.2.3. Formation and characterization of the capillary bridges

This section details how a liquid bridge can be introduced between two substrates followed by its characterization via imaging at different heights and fluid volumes.

3.1. Using two pillar substrates (made in Steps 1-2), place one in the top and one in the bottom holders. Secure the substrates using side tension screws.

Note: See Figure 1 and representative results for device details.

3.2. Assemble the device by attaching the top substrate stage to the bread board such that the top substrate is roughly above the bottom substrate. Decrease the height between the two facing pillars to about 1mm.

3.3. Rough alignment: using the x, y, and rotation knobs on the bottom substrate stage align (by eye) the gold strips for the two substrates so that they are parallel (looking top down through the top substrate).

3.4. Fine alignment: position the camera to look down the length of the PDMS pillar. Using the live camera feed on the computer screen, further adjust the position of the bottom substrate so the pillars are parallel.

3.5. Move the camera to the opposite side of the device and repeat step 3.4.

3.6. Decrease the separation between the two pillars until the top pillar makes contact with the bottom pillar (using live camera feed). Zero the digital micro stage. This will be defined as a pore height of zero.

3.7. Increase the pore height to approximately 200 μm .

3.8. Prepare a syringe with 1-5 μ L of an 80% glycerol 20% water solution. Attach a 30 gauge needle to the end of the syringe, making sure no air bubbles get trapped inside the needle.

Note: The water/glycerol mixture is used to reduce evaporation during the experiment. Water can also be employed.

3.9. Mount the syringe to the syringe xyz translation stage with a mechanical clamp.

3.10. Adjust the micrometers on the syringe positioning stage so that the needle fits into the slit pore (parallel to the length of the pillars).

3.11. Decrease the slit pore height so that the top and bottom surfaces gently contact the needle. This will make sure that the liquid will touch both surfaces and spontaneously form a capillary bridge.

3.12. Dispense the liquid from the syringe into the slit pore slowly.

3.13. Use the micrometers on the syringe positioning stage to remove the needle from the slit pore.

Note: At this point, the height of the slit pore can be varied and the liquid bridge imaged.

Note: The pictures can be analyzed with the open source software package ImageJ.

A.3 Representative Results:

A.3.1. Description of the experimental device

The experimental device can be broken up into four main parts: 1) the top substrate stage, 2) the bottom substrate stage, 3) the syringe/ syringe xyz-translation stage and 4) the camera/optics and camera holder. The details of each follow:

- 1) **Top substrate stage.** A digital translation stage is attached to a P-series mounting clamp via a custom machined connector piece. The mounting clamp is connected to a variable height P-post which is anchored to a bread board via a P-series clamping fork. A custom connection piece attaches to a custom machined glass slide holder to the translation stage, providing 1 μm displacement resolution in the z-direction.
- 2) **Bottom substrate stage.** A xy linear translation with z-axis rotation stage is attached to the bread board via 8 post extension pieces. A custom machined substrate holder is attached to the top of the xy linear translation with z-axis rotation stage, allowing the bottom substrate to be positioned with 10 μm translational resolution and rotated with 1 degree resolution.
- 3) **Syringe/syringe xyz translation stage.** For xyz positioning of the syringe used to fill the gap between the pillars, a 5 μL syringe with a 30 gauge needle is attached to a xy translation stage. The xy stage is then attached to a z translation stage via a 90° connector piece.

4) **Camera/ optics and camera holder.** For imaging of the liquid bridges, a CCD camera is attached to a variable zoom optics piece. At maximum zoom, this gives a resolution of 3.3 μm / pixel. The camera is attached to a laboratory scissor jack, which can be positioned to image the liquid bridge from different angles.

A.3.2. Transfer of Au foil to PDMS pillars

In the transfer of the gold to the PDMS substrate, it is important to separate the PDMS device from the silicon wafer smoothly and carefully (see Step 2.2.6). Figure 3a shows a microscope image of a PDMS pillar with gold after a successful transfer. Figure 3b shows excess gold foil from the wafer that was transferred to the pillar due to poor transfer. To facilitate the transfer of the gold film a sharp safety razor can be used to gently pry one edge of the PDMS pillar from the silicon wafer. Additionally, the PDMS substrate should be pulled in a direction normal to the wafer's surface (avoid lateral motion) to prevent additional gold foil from sticking to the edge of the substrate. Figure 3c shows how cracks can form in the gold layer after transfer if the PDMS substrate undergoes significant shear or bending.

A.3.3. Characterization of the MHA monolayer

Once the fabrication process (Step 2) is finished, it is important to verify the quality of the MHA monolayer by testing its water contact angle. Figure 2 shows a liquid water drop on an Au/PDMS substrate after being functionalized with MHA. The low contact angle on the PDMS indicates that the process was successful. The inset of figure 2 shows a liquid water drop placed on one of the raised pillars after the completed

procedure. The 140° contact angle demonstrates that the combination of physical and chemical heterogeneities allow the drop to be pinned on the sides of the pillars.

A.3.4. Visualization of capillary bridges

Once the substrates have been fabricated and installed into the microstage holders, the channels can be filled using the syringe/syringe xyz translation stage. Figure 4a shows a filled slit pore with a perspective perpendicular to the width of the pillar (looking “down the barrel” of the channel). Figure 4b shows a perspective orthogonal to 4a, that is, perpendicular to the length of the slit pore. 4c shows the process of filling the channel from the same perspective as 4b. It is critical during the filling stage to dispense the liquid from the syringe slowly. The force from sudden large flow rates can depin the liquid from the top of the pillar, causing it to spread onto the hydrophobic PDMS regions. If this happens, the substrates must be cleaned and dried and the filling process repeated.

A.4 Figures

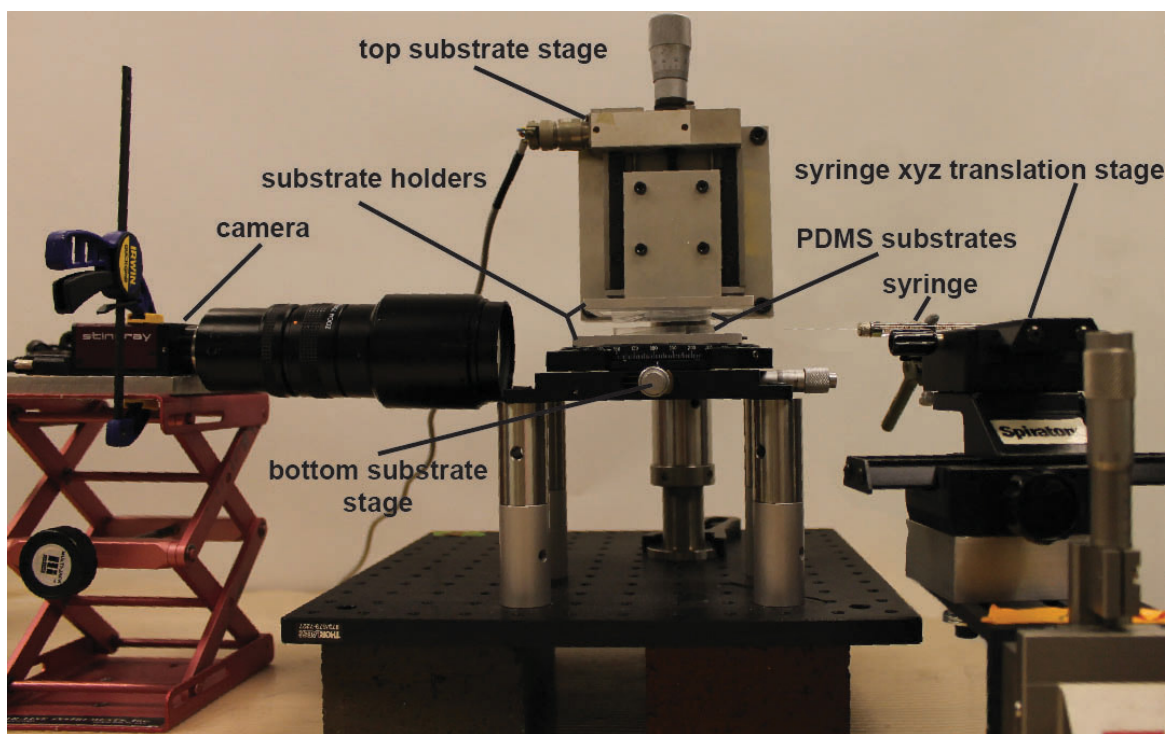


Figure A.1: Picture of complete experimental set up. The PDMS substrates are held at a variable distance apart through a combination of x,y,z and rotation stages. A separate set of microstages (far right) holds the syringe to introduce the liquid into a narrow gap to create the capillary bridge in a slit-pore geometry. A CCD camera (pictured left) is used to image the resulting capillary bridges as the pore separation is changed. The resulting images can then be analyzed in the open source image analysis software ImageJ.

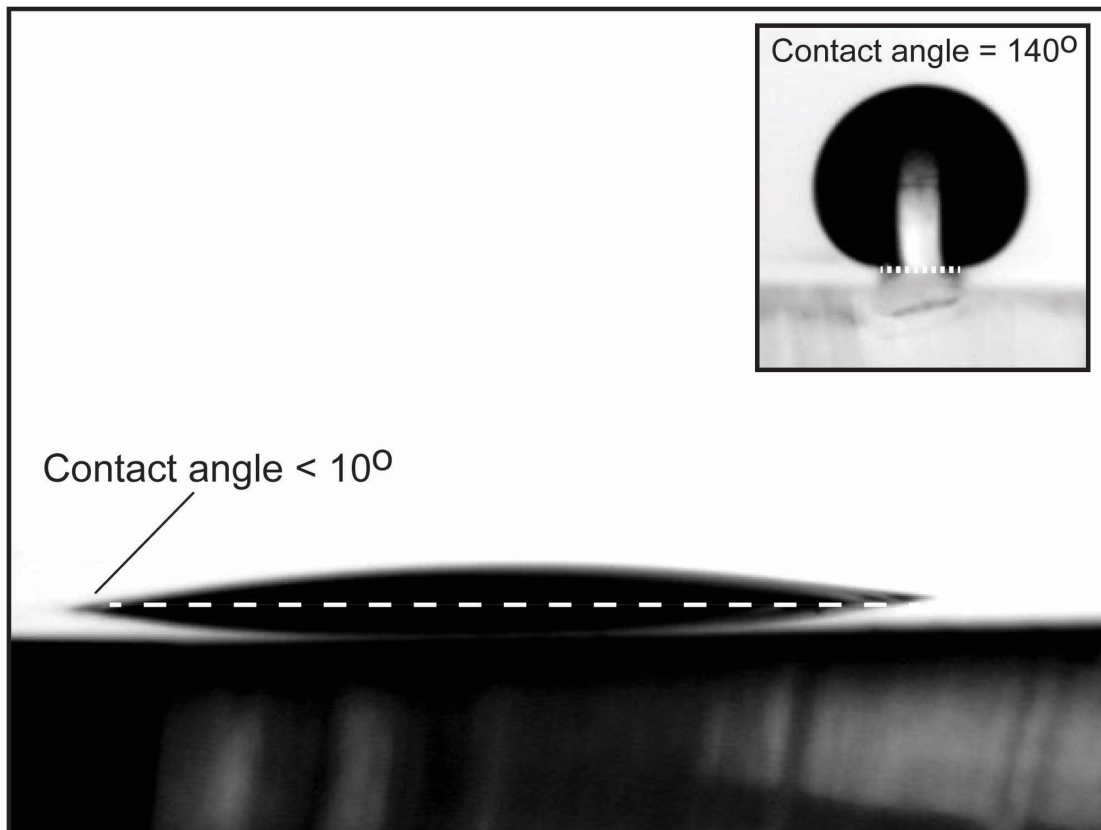


Figure A.2: PDMS substrate with 20nm Au layer functionalized by a MHA self-assembled monolayer. The low water contact angle shows that the procedure was successful. The inset shows a drop on a raised functionalized PDMS/Au pillar.

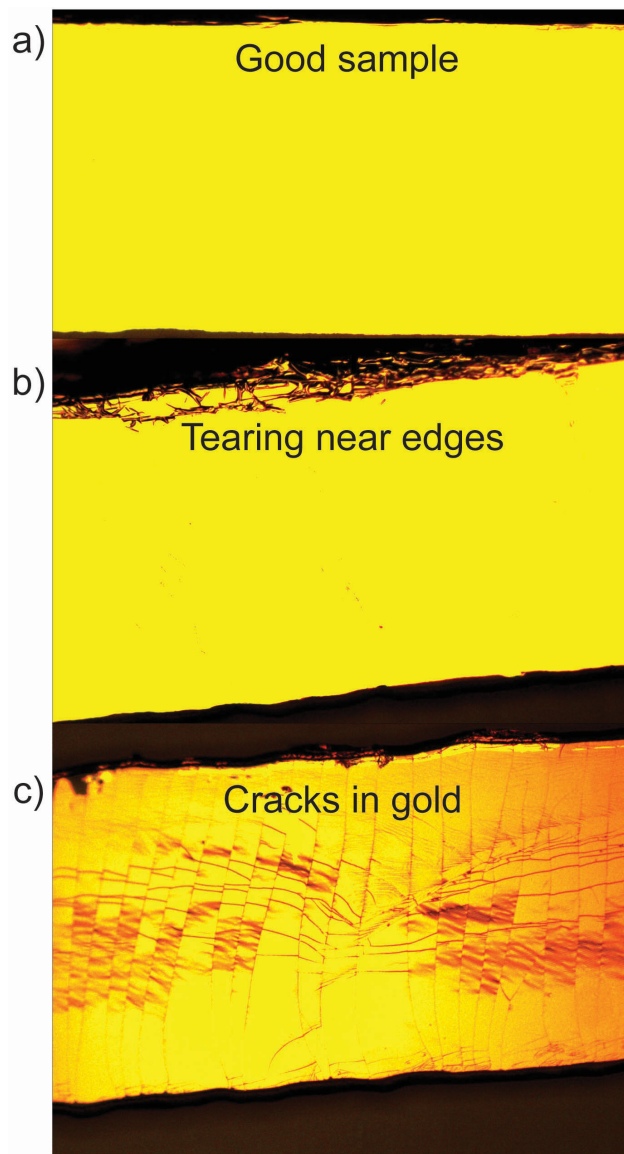


Figure A.3: Raised PDMS pillar after transfer of 20nm Au layer. a) Successful transfer. b) Tearing due to lateral motion of the PDMS substrate during the transfer process. c) Cracking caused by the bending of the PDMS substrate during the transfer process.

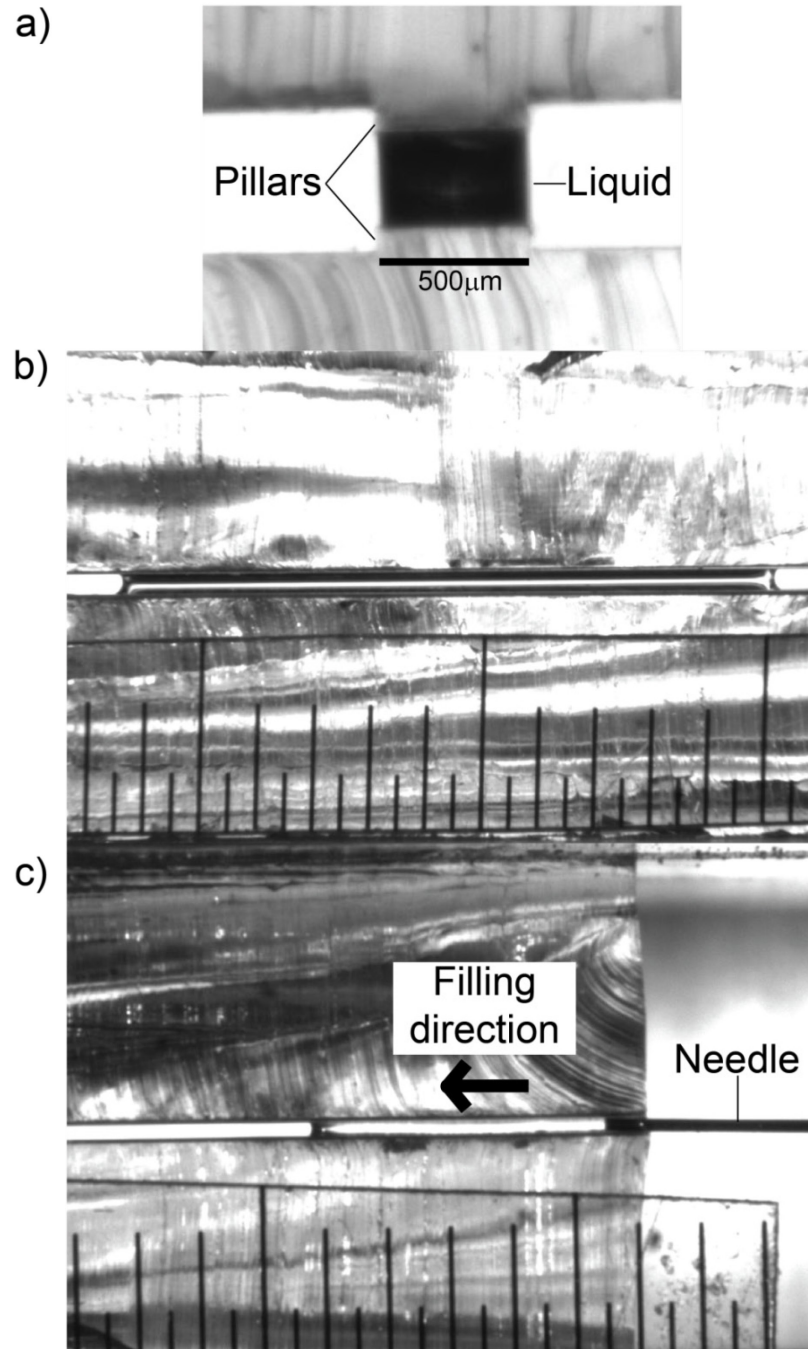


Figure A.4: Images of capillary bridges on pillars in the experimental device. a) Field of view parallel to the length of the pillar. b) Field of view perpendicular to the length of the pillar. c) Shows the filling process of the slit pore (same perspective as b). The minor graduation of the ruler in b) and c) is 500 μm .

A.5 Discussion:

The method presented here provides a way to create capillary bridges in slit pore geometry, and also a method for imaging these bridges so that their morphology can be analyzed and compared to simulation and theory.

This method incorporates physical relief as well as selective chemical patterning to create asymmetric wetting properties. If only a chemical heterogeneity is present, a liquid drop will stay pinned on the heterogeneity until the contact angle exceeds that of the less wettable (lower surface energy) region. When PDMS is the region of lower surface energy, the maximum achievable contact angles at the hydrophilic/hydrophobic boundary is around 100° . Adding a physical heterogeneity in the form of a pillar allows for significantly larger water contact angles at the edge of the pillars ($> 140^\circ$), as seen in figure 2 (An alternate method for creating similar substrates is presented by Ferraro et al.¹³³). Higher contact angles imply that liquid drops or bridges can be confined to specific areas and sustain higher pressures than would be possible for a purely chemical heterogeneity.

Since the gold on top of the PDMS pillars is functionalized with a self-assembled monolayer, different functionalizations are possible using different thiol precursors. Also, in addition to being able to adjust the height of the slit pore, the combination of microstages allows for real time adjustment of both lateral and rotational offsets. This functionality would make such a device ideal for imaging dynamic capillary bridges systems, such as those relevant to ink jet or gravure printing.

A.5.1. Critical steps within the protocol

To obtain reproducible capillary bridge morphologies precautions must be taken in the preparation of the chemical and physical heterogeneities. For example, pillars with a thickness gradient lead to bridges located at the end of the pore where the PDMS is thicker. Thickness gradients can arise if the plastic weighing dish holding the liquid PDMS during the molding step is not lying perfectly flat. The change in height along the length of the pore can also lead to a change in the curvature of the liquid, skewing image data. The extent of this thickness variation can be evaluated when the zero point is set in Step 3.6. The tilt of the top substrate holder can be reduced by placing a soft spacer between the top substrate holder and the substrate holder-z stage connector piece (a few layers of masking or foam tape works well for this.) By varying the tension on the screws that attach the connector piece to the substrate holder, the tilt can be eliminated from the system.

It is also important to ensure that no excess DMSO is left on the substrates after the 24 hours DMSO/MHA soak. It is possible that a small amount of residual DMSO can be present on the substrate even after rigorous rinsing with DI water. If the substrates are used at this point, the excess DMSO can leach into the capillary bridge. Excess DMSO can be evaporated from the sample by placing it in a vacuum chamber (pressure < 100mTorr, 25° C) for at least 12 hours.

A.5.2. Limitations of the technique

A chief limitation of using raised pillars to form high aspect ratio capillary bridges becomes apparent during imaging. When the height of the pore is changed at constant volume, the liquid recedes away from the ends towards the center of the pore⁵². As a consequence, the bridge can become out of focus when imaging normal to the width of the strip. This loss in focus happens when the distance between the end of the slit pore and the liquid bridge exceeds the depth of field of the camera. It is therefore important to use the shortest possible slit pore lengths required for a given experiment. The depth of field can be extended by changing optics, or by decreasing the magnification, but these come at a cost to resolution.

The tops of the PDMS pillars are functionalized to have a high surface energy (low water contact angle). As a consequence they are susceptible to contamination, coming either from the ambient environment or the fluid. Our experiments were performed in a cleanroom (class 1000) which allowed us to test the samples 5 to 10 times before any degradation of the surface was noticeable. Contamination leads to pinning of the wetting angle for the contact line parallel to the width of the pillars.

A.6 Table of specific reagents and equipment:

Name of the reagent	Company	Catalogue number
99.999% gold wire	Kurt J. Lesker	EVMAU40040
Acetone	Pharmco-AAPER	C1107283
Dimethyl sulfoxide	Fisher	D128-500
Ethanol (200 proof)	Pharmco-AAPER	111000200
Hydrochloric acid	EMD	HX0603-4
Hydrogen peroxide (30%)	EMD	HX0635-3
Isopropyl alcohol	Fisher	L-13597
Mercapto hexadecanoic acid (90%)	Sigma-Aldrich	448303-1G
Mercapto-propyl-trimethoxy-silane (MPTS)	Gelest	Sim6476-O-100GM
Mili Q DI water	Millipore	Mili-Q
Nitrogen (gas)	Airgas	UN1066
Oxygen (gas)	Airgas	UN1072
Silicon wafers (4 in)	WRS Materials	CC8506
SU-8 2002 (negative photo resist)	MicroChem	SU82002
SU-8 2050 (negative photoresist)	MicroChem	SU82050
SU-8 developer solution	MicroChem	Y020100 4000L1PE
Sulfuric acid	J.T. Baker	9681-03
Poly dimethyl sulfoxide (PDMS)	Dow corning	Sylgard -184
Toluene	Omnisolv	TX0737-1

Table A1: Specific chemicals and reagents used for the fabrication of MHA functionalized raised PDMS pillars.

Name of equipment	Company	Catalogue number
Bread board	Thorlabs	MB3030/M
CCD camera	Allied Vision Technologies	Stingray F125B
connector piece	Newport	360-90
Digital translation stage	Klinger	MR 80-25
Goniometer	First Ten Angstroms	FTA 125
Needle (30 guage)	Hamilton	91030
Optics piece	Navitar	Zoom 7000
plasma reactor	Home built	Home built
Post extension piece (x8)	Thorlabs	P100/M
P-series clamping fork	Thorlabs	PF175
P-series mounting clamp	Thorlabs	C1525/M
Spin coater	Laurell	WS-400B-6NPP/lite
syringe (5mL)	Hamilton	87930
Thermal evaporator	Kurt J. Lesker	Nano 38
Ultra violet lamp	Thermo Oriel	66142
Variable height P-post	Thorlabs	P100/M
xy linear translation with z-axis rotation stage	Thorlabs	XYR1/M
xy translation stage	Spiratone	xy-stage
z translation stage	Newport	M-462

Table A2: Specific parts used to create experimental 4-axis micro stage and imaging device.

Curriculum Vitæ

David Broesch was born on August 23, 1986 in San Diego California, where he remained until finishing his secondary schooling in 2004. He then attended the University of California Santa Barbara, receiving a bachelors degree in physics with highest honors in 2008. During his time at university, he was awarded a National Science Foundation research in science and engineering (RISE) fellowship to conduct undergraduate research on the formation of vesicles in AC electric fields. In 2008 he became a graduate research assistant at the Johns Hopkins University in the Department of Chemical and Biomolecular Engineering under the advisement of Dr. Joelle Frechette. His research interests include experimental and numerical simulation investigations of pinned and partially pinned capillary bridges between solid substrates.